DIPARTIMENTO DI SCIENZE CHIMICHE

CORSO DI LAUREA MAGISTRALE IN CHIMICA

Coupling dry reforming of methane with nitric oxide reduction on nickel-based nano-catalysts: the role of C

Relatore: Prof.ssa Antonella Glisenti

Laureanda: Beatrice Senoner

matricola 2040611

Anno Accademico 2021/2022

INDEX

1. INTRODUCTION

One of the problems of today's society is to secure the supply of energy and fuels through environmentally sustainable processes. The massive employment of fossil fuels in power plants and transportation, that has characterized our society until today, has led to issues such as the emission of molecules harmful for human health or dangerous to the ecosystem. Increasing concentrations of pollutants such as NO_x, CO or greenhouses gasses like CO_2 during the last century have led to environmental and health concerns. In this scenario, different solutions have been implemented to reduce the impact of those substances. For example, renewable sources of energy are an interesting source to supply for energy demand, and various ways to convert or store emissions - such as CO_2 storage devices- have been implemented. In order to efficiently convert harmful substances into chemicals, it is important to search for processes that transform pollutants and waste products into inert substances or useful compounds. Among these processes, methane conversion to valuable chemicals has taken a lot of consideration in the recent years. Methane can be converted to syngas, a gas mixture of high energy content, composed by CO and H_2. Syngas can be then used as fuel or as reagent in industrial processes, also depending on the H_2:CO ratio, such Fischer-Tropsch synthesis, methanol process, carbonylation or hydrogenation.[1]This conversion of methane to syngas can be achieved by different routes, such as reforming or partial oxidation. [1], [2]

Among different kinds of reforming, dry reforming of methane is one of the most interesting options, as it allows the conversion of two major greenhouse gasses, CO_2 and CH_4, to syngas, with a H_2:CO ratio around 1:1. To catalyze this reaction, noble metals have been widely used for dry reforming of methane, thanks to their high catalytic activity and their resistivity to carbon deposition. However, noble metals are not industrially applicable due to their high cost and low availability. [3] That’s why one of the most commonly used metals is Nickel, which provides comparable activity to noble metals, without the heavy cost of the latter. [4] However, Nickel catalysts are sensible to deactivation by coking and by sintering, while noble metal catalysts are more resistive against carbon deposition. [1], [5]. So, in order to develop catalysts with an industrial applicability, extending their lifetime is one of the key issues. [5]

Although numerous strategies have been developed to solve the issue related to coke deposition, such as partial oxidation of methane (POM), this phenomenon cannot be avoided in the long run, making it crucial the development of alternative solutions to extend the lifetime of catalysts.

In this project, catalysts will be studied for a process in which dry reforming of methane and nitric oxide reduction reactions are involved. Coupling those two reactions allows to eliminate the carbon that deposits onto the catalysts during DRM by exploiting the oxidizing power of one of the biggest pollutants in the atmosphere, which has reached tens of millions of tons/year of emissions: nitric oxide. This pollutant is responsible for acid rain, photochemical smog and ozone build-up, so that its conversion into unharmful

substances is needed to avoid ecological consequences. Nitric oxide is currently emitted mainly from power plants and post-production capture systems applied to natural gas turbines are currently available.[6], [7]

The process is adaptable to different sources and concentration of CH_4, CO_2, NO - i.e. flux gases from different industrial plants - possibly adjusting the reaction temperature to obtain the best syngas yields.

1.1 Dry Reforming of methane (DRM) process

Dry reforming of methane is a process that converts CO_2 and CH_4 into syngas.

$$CH_{4(g)} + CO_{2(g)} \longrightarrow 2CO_{(g)} + 2H_{2(g)} \qquad (1)$$

The reaction is endothermic, with a ΔH^0=260 kJ/mol$_{CH_4}$ at 750°C. So, major conversions will be achieved at high reaction temperatures. However, temperature doesn't only influence DRM reaction. As a matter of fact, both products and reagents are involved in other reactions in the process:

$$CO_{2(g)} + H_{2(g)} \longrightarrow CO_{(g)} + H_2O_{(g)} \qquad (2)$$

$$CH_{4(g)} \longrightarrow C + 2H_{2(g)} \qquad (3)$$

$$2CO_{(g)} \longrightarrow C_{(s)} + CO_{2(g)} \qquad (4)$$

CO_2 that flows into the reactor and H_2 produced by DRM react via reverse water-gas shift reaction (2), an endothermic reaction with a ΔH^0=34 kJ/mol$_{CO_2}$ at 750°C. This reaction causes a decrease in H_2:CO desired ratio of 1:1, making the syngas produced less economically valuable. Other side reactions involve coke formation. The formation of coke results from CH_4 decomposition (3) and from CO disproportionation (4), also known as Boudouard reaction, and leads to the deactivation of the catalyst. CO disproportionation is an exothermic reaction, so its thermodynamic constant decreases as temperature rises, while CH_4 decomposition is an endothermic reaction. Reitmer's calculations show that coke deposition decreases overall with increasing temperatures, so the greatest contribution to coke deposition is due to CO disproportionation. [1], [2]

Moreover, another cause of deactivation is the oxidation of the catalyst due to CO_2 oxidative power. [8] However, DRM's environment is both oxidative (CO_2, H_2O) and reductive (H_2, CH_4, CO), leading to a partial reduction of the oxidized metal to its elemental form. [9]

Dry reforming of methane is a reaction that can be conducted over a wide range of temperature. Among the advantages of working at higher temperatures there is the fact that, being an endothermic reaction, it is thermodynamically favored at higher temperatures; moreover, the H_2/CO ratio is higher- meaning an higher economic value of the product. However, working at high temperatures have also a negative side: the high energy consumption. [1] Depending on the reaction at which DRM is conducted, a change in concentration of reagents and products occurs. In order to have an idea of this change of composition over temperature, the equilibrium compositions of reactants and products have been plotted against temperature in the following Fig. 1:

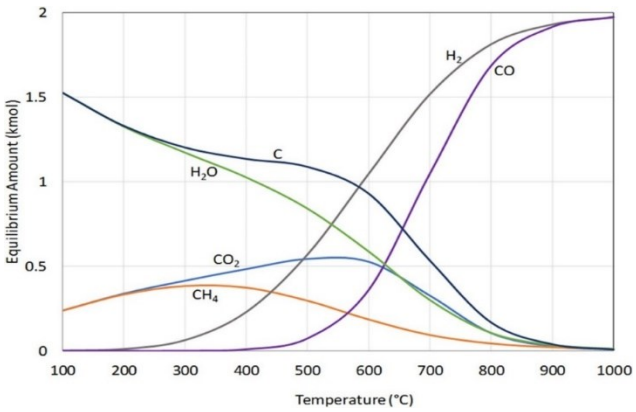

Figure 1- equilibrium composition vs temperature obtained from HSC Chemistry assuming 1kmol of initial CH_4 and CO_2 and at 1atm pressure.[2]

1.1.1. Dry Reforming of Methane (DRM) mechanism

Dry reforming mechanism has been an object of many discussions, as the mechanism of the reaction depends as well on the support. However, it's widely accepted that CH_4 and CO_2 don't react directly but are firstly activated following a Langmuir-Hinshelwood mechanism. While inert materials are characterized by mono-functional pathway, so to say that CH_4 and CO_2 are both activated on the active metal, basic and acid supports lead to bi-functional mechanisms where CO_2 is activated on the catalyst's support and CH_4 on the active metal. Different specific mechanisms were proposed for various supports.[2] It's widely accepted that methane activation has different steps involving CH_x species (x=0-3). Either the steps that lead to CH_x formation or the reaction between CH_x and the oxidant are considered the slow steps of the reaction, with the oxidant being CO_2 or oxygen adatoms originating from CO_2 dissociation. For γ-Al_2O_3, Zhang and Verykios

have proposed as rate determining step, the reaction between surface carbon species and the oxidant. [10] In case of perovskites, a specific mechanism is proposed, which involves the formation of oxycarbonates. In this case CO_2, which has a lower activation energy than CH_4, is chemisorbed by the support to form oxycarbonates species, while methane is activated on the active metal, with possible influence of the oxycarbonates.[2] Overall, the results present in literature are not conclusive as they depend on reaction conditions.

1.1.2. Coking

Coking, term used to describe carbon's deposition, is one of the main causes of catalysts' deactivation. [11]

The coke that deposits on the catalyst is due both to Boudouard reaction, which takes place below 800°C, and methane decomposition, over 550°C. Even if the terms carbon and coke were originally used to differ these species, with the first being product of CO disproportionation, and the latter product of CH_4 decomposition, those definition were somewhat arbitrary, and have been consequently used interchangeably in the last decades. [12] In this work, the terms coke and carbon are used interchangeably to describe the carbonaceous deposits that form due to both reactions. [13]

Coke deposits onto the catalysts following various pathways: carbon can cover the nickel particles encapsulating them, it can block the pores of the catalyst reducing the accessibility of reactants to active sites or develop in form of filaments that cause the catalyst to break and be destroyed. [13], [14]

Depending on the supports and the reaction conditions, different kind of coke is formed. 5 different kind of coke can be deposited over the catalyst, classified in order of decreasing reactivity from α to γ: amorphous carbon C_α, filament carbon C_β (polymeric films and filaments), graphite carbon C_γ (vermicular whiskers/fibers/filaments), bulk carbon C_γ and crystalline carbon C_c (graphitic platelets and films). [2] It is important to understand how to obtain highly reactive carbons in order to easily gasify the coke that deposits on the catalysts. Not only it has been proven that the type of support deeply influence the coking in both quantity and type [15], but the type of coke is also deeply influenced depending on the reaction that causes its deposit. As a matter of fact, coke produced by Boudouard reaction is less reactive than the one produced via methane decomposition: methane dissociates on nickel surface and generates C_α, which is highly reactive and can react with H_2O, CO_2 or H_2 to be gasified, or it can evolve to C_β. [16]

At the reaction conditions considered for this process, coke gasification will occur thanks to H_2O and CO_2, as H_2 helps with coke gasification at temperatures below 650°C. While CO_2 is a reactant, H_2O is present thanks

to the reverse water-gas shift reaction. Gasses react with coke giving respectively as products CO and CO and H_2. [17]

1.2. Nitric Oxide Reduction

Nitric oxide reduction is the step chosen as a solution to coking deposition. Here, coke is employed for its reducing abilities. Flowing nitric oxide into the reactor, the coke that is deposited during DRM can react with NO via the following reactions (5):

$$C_{(s)} + xNO_{(g)} \longrightarrow CO_{x(g)} + x/2\ N_2 \qquad (5)$$

$(x = 1,2)$

The reaction is exothermic, with a ΔH^0 of -203 and -576 kJ/mol_C for x=1 and x=2 at 750°C.[18]

However, nitric oxide can react with other species apart from coke. NO reduction can occur both reacting with Ni particles (300-500°C), giving N_2 and N_2O as products, and with the coke deposited on the particles, producing N_2, CO_2 and CO (mechanism significantly present above 677°C). As CO formation is competitive with that of CO_2, given the higher economic value and interest in application of CO compared to CO_2, the temperature range chosen is the one in which CO production is favored, i.e. 650-850°C.

The mechanism proposed in Hu et al. involves the formation of an N_2O intermediate from two NO molecules; subsequently N_2O decomposes to N_2 and the remaining O atom oxidizes Ni to NiO (XRD).

High temperatures play a role in facilitating the Ni-catalyzed evolution from N_2O to N_2. [18] These mechanisms have been represented in Fig. 2.

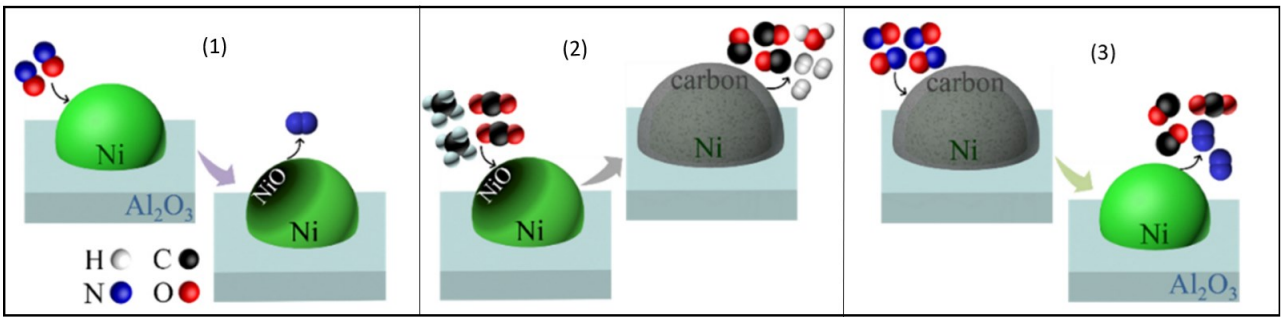

Figure 2-Schematic representation of NO oxidation by nickel (1) and by coke deposited on nickel (deposition of nickel (2)- coke removal (3)) [2]

Finally, we must consider that methane could be reduced also by methane and hydrogen that are present in the reactor, as the studies around NO removal technologies have shown in the last decades. [19], [20]

1.3. Catalysts

To increase the catalytic activity and avoid undesired side reactions, catalysts' design is the key. The catalysts proposed are constituted by an active part and a support. The active part consists in nickel nanoparticles, while the support has the role of dispersing the metal nanoparticles, affecting both the interaction with nickel and the size of particles; the support can have various properties that modify the affinity and/or the adsorbtion of gasses involved in the process. To evaluate the role of different supports in the catalytic activity, both the nickel percentage on the catalyst and the technique to deposit it were maintained the same over the different catalysts in this thesis work.

To deposit nickel, an economic, reproducible and simple way has been chosen: wet impregnation.

To choose the quantity of Ni loading to impregnate on the supports, previous works have been considered to optimize the nickel quantity employed. Higher nickel content leads to a higher number of catalytic sites, leading to an increase of the catalytic activity, but it also decreases the specific area of catalysts and the metal dispersion. This is due, respectively, to the blockage of the support's pores and to the increase of nickel particle size. Moreover, nickel content is related to the quantity of coke that is deposited on the catalyst during the process. Nickel content has been commonly used for DRM reaction in a content between 10% and 15% , so these percentages can be considered as standard. [1], [15], [21]–[24]

Moreover, commercial catalysts with a nickel percentage around 13% have been developed for DRM processes, showing a good stability. [15] So, in order to obtain good catalytic activities and to study coke's deposit and its removal thanks to NO, nickel loading was chosen as 13%, the quantity also chosen in J. Hu et al. work. [18]

1.3.1 Properties of the supports

Among various aspects that need to be evaluated for the supports' choice, the main ones are cited below:

- mechanical strength: it's important to provide catalysts with good mechanical strength in order to have an industrial application

- thermal stability: catalysts must be resistant to high temperatures, as dry reforming of methane is an endothermic process conducted between 500-1000°C.

- surface area: this must be as large as possible to promote the catalytic activity, without compromising the mechanical stability of the catalyst.

- sintering resistance: sintering can be decreased through homogeneous nanoparticles dispersion methods, that allow controlling the size of the latter [9], and through supports favoring strong metal support interaction.

- metal support interaction (MSI): A strong MSI is essential to ensure good dispersion of Ni particles, on which catalysts' performance depends. Ni particles are thus dispersed on a support in the form of nanoparticles, and the higher the MSI, the lower the risk of sintering. In addition, a strong MSI leads to more amorphous carbon being formed during DRM, which discourages the formation of nanofibre-like carbon. Carbon nanofibers are a problem as they tend to settle at the Ni/support interface, leading to the detachment of nickel from the substrate. Amorphous carbon can be oxidized to CO_2 if enough vacancies are present and oxygen diffusion on the substrate surface is possible. A strong MSI interaction also facilitates the transfer of 3d electrons of Ni to the support, helping with the activation of adsorbed CO_2 (6). [25]

$$CO_2 + V_O + 2e^- \rightarrow CO + O_O^x \qquad (6)$$

-acidity/basicity: the presence of basic sites helps with the gasification of carbon deposits, while acid sites promote coke deposition. Basic sites help as a matter of fact with CO_2 adsorption, given the higher affinity of this acidic molecule with the support; by increasing chemisorbed CO_2 on the surface of the catalyst, carbon dioxide will be able to gasify coke ($C + CO_2 \rightarrow 2CO$). As acidic supports have less CO_2 chemisorbed onto the catalyst, the carbon that deposits onto the catalyst will be less easily gasified. So, carbon deposition and

ageing of the catalyst will be partially prevented on basic supports. [26] Therefore, supports with strong Lewis base character will be investigated. [27]

-oxygen mobility: The presence of mobile lattice oxygen helps with the activation of methane's C-H bond, and with coke deposits as well, as it leads to carbon oxidation to CO (see after). [26]

- presence of vacancies: oxygen vacancies interact with both CO_2 adsorbtion, coke deposition mechanism and NO reduction. Oxygen vacancies promote CO_2 adsorbtion, increasing coke gasification. In NO removal, the redox capacity of the substrate plays an important role, as oxygen vacancies allow NO adsorption. This can influence also NO decomposition mechanism, as at high temperatures in perovskites two NO molecules adsorbed at adjacent sites can decompose. Perovskites oxides catalysts have a general formula ABO_3 (see after in chapter 1.3.2.), with A cation surrounded by 12 oxygen anions and cation B surrounded by 6 oxygen anions. If the cation B can be oxidized, a simultaneous oxidation of the B atom occurs together with NO adsorbtion, and electrons lost in B atom oxidation go into NO antibonding orbital, forming NO^- species. This species can interact with an adjacent NO^-, giving N_2(g). [28]

1.3.2. Supports for catalysts

In order to investigate support's role in both catalytic activity and on the type of coke that is deposited on the catalyst, different supports have been chosen.

The first support investigated is Al_2O_3, an inert support, which is the most common support used for dry reforming of methane, and also the support chosen for the chemical looping work of J. Hu et al. [15], [18]. Al_2O_3 is a cheap and readily available substrate. Alumina morphology also plays an important role in catalytic activity and catalyst stabilization. Alumina catalysts benefit of a high surface area, good thermal stability and the ability to disperse nickel well. Possible polymorphs interesting for catalysis are γ, α and θ phases. The γ-phase is the one with the largest surface area, however it shows problems regarding the formation of the $NiAl_2O_4$ spinel at high temperatures, which increases sintering and decreases its reductive capacity. However, in Wang et Lu. work[29], γ-Al_2O_3 was found to be the catalyst with the highest catalytic activity, being compared with α- Al_2O_3, MgO and SiO_2. In this paper, γ-Al_2O_3 highest activity is explained thanks to the presence of strong MSI interaction of Ni nanoparticles reduced from the spinel. [30] This strong MSI provides great resistance to sintering and coking, so γ-Al_2O_3 is the first support chosen.

As Al_2O_3 is a mildly acidic support, it does not facilitate the adsorption of CO_2, which is itself an acidic molecule. [31] So, to facilitate CO_2 activation, systems with basic cations or oxygen vacancies will be taken into consideration to allow a better CO_2 coordination.

To choose the next support for the process, supports with high metals support interaction are taken into consideration. Among those, spinels oxide have been studied for DRM reaction due to their stability at high temperatures. [32] Spinels are a class of compounds with general formula AB_2X_4, with the anion X being oxygen, sulfur, tellurium, selenium or nitrogen (Fig. 3). [33] Their structure is based on a cubic close packing of anions, while cations are inside tetrahedral and octahedral sites. Among this wide class, oxygen spinels have been studied thanks to their high stability and effective dispersion of active metal particles. [34]. Spinels oxides can be classified in "2-3 spinels" ($A^{2+}B_2^{3+}O_4$, such as $MgAl_2O_4$ spinel – Fig. 4) and in "4-2 spinels" ($A^{4+}B_2^{2+}O_4$). [35]

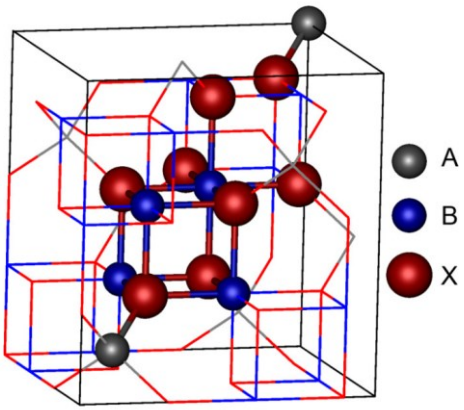

Figure 3- Schematic representation of spinel's unit cell, with cation A in a tetrahedral site and cation B in octahedral site[29]

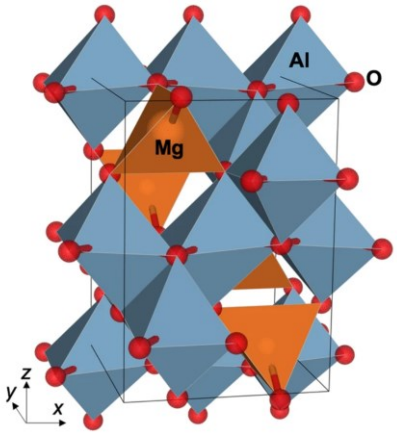

Figure 4- Schematic representation of $MgAl_2O_4$ [30]

Among spinels, magnesium aluminate spinel ($MgAl_2O_4$) has been investigated for dry reforming thanks to its good chemical stability, thermal stability (melting temperature above 2000°C) and mechanical strength. Those characteristics, together with its basicity and its resistance to sintering, makes it a valid support for DRM process. [15] This spinel provides a strong metal-spinel interaction which causes partial insertion of Ni into the spinel and subsequent deformation of the lattice and formation of oxygen vacancies. This could be a promising scenario to discourage the oxidation of Ni, and to encourage at the same time the adsorption and dissociation of CO_2 due to the presence of vacancies. [32]

To investigate further supports, perovskites represent a valid alternative. The term Perovskite was originally used to indicate the $CaTiO_3$ mineral, which was discovered by Lev Sinovsky in 1839; subsequently a wide class of materials with the same crystal structure has been identified, and so the term "perovskite" became interchangeable with "perovskite structure". Those compounds have a general formula ABX_3, where A and B are cations, with cation A bigger in size than B, and the anion X either O, N, S, Te, Se, or a halide.

Thanks to their peculiar structure, stable oxide perovskites can be obtained with 90% of metallic natural elements of the period table; this feature allows them to be used in a large variety of reactions, as supports or as catalysts.[36] Their peculiar crystal structure determines the coordination number of the cations, respectively 12 for cation A and 6 for B (Figs. 5 and 6). [37], [38]

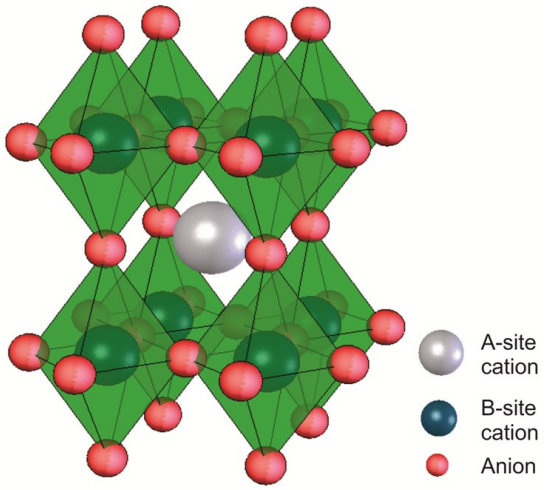

Figure 5- schematic representation of ABX3 perovskites [39]

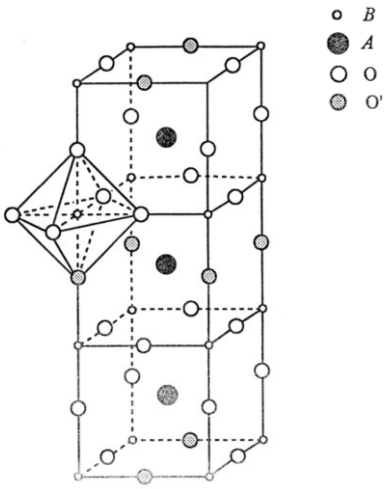

Figure 6- Schematic representation of oxide perovskite structure [31]

Ideally, perovskites have a cubic structure, where cation A is surrounded by 12 anions X and cation B surrounded by 6 X. The cubic unit of the structure has a B cation in the corner, coordinated with 6 oxygen atoms in an octahedra, and the center of the cube is occupied by an A cation. This structure can alternatively be viewed with A in the corner and B in the center of the cube.

The ideal cubic structure can be distorted, depending on the radius of cations, giving most commonly orthorhombic or rhombohedral distortions; therefore a tolerance factor (t) was defined by Goldschmidt to measure this deviation, reported in equation (6) . [2]

$$t = r_A + r_O/\sqrt{2}(r_B + r_O) \quad (6)$$

This formula is applicable at room temperature, and r is the empirical ionic radius of the ion. The ideal cubic structure has a *t* factor of 1, but stable structures can be obtained with a *t* factor between 0.75 and 1. [36]

Those compounds, in addition to having excellent thermal and redox stability, are materials with a flexible nature, both chemically, electronically and in terms of their crystal structure. This characteristic allows to tune the desired properties- such as photocatalytic activity, optical properties, ferroelectric properties, superconductivity, magnetic properties, mechanical and electrochemical properties. As for their disadvantages, they usually demand high calcination temperatures, resulting in low surface area values, usually around 10 m^2/g. [2] Overall, the versatility of perovskites makes them interesting materials for catalyst design of various reactions- among them CO oxidation or NO reduction.

Perovskites can extend their properties by doping, i.e. A and B cations can be partially substituted with other ions. [40], [41] The possibility to substitute the original ions with ions of different oxidation numbers (aliovalent doping) affects both catalytic activity and structure of the catalyst. Structural defects develop in the perovskite structure indeed, having an impact in both catalytic activity and oxygen mobility, caused by the non-stoichiometry of the doping. [36] In fact, substitution with a cation whose oxidation number is smaller than the original one leads to an excess of charge of oxygen that, not being anymore compensated, is partially released, forming oxygen vacancies. Those vacancies are very important in our process as they allow to coordinate molecules with oxygen terminal atoms and they increase the oxygen mobility of the catalyst, helping with coking gasification. [38]

Among the perovskites studied as support for DRM there is $CaZrO_3$. It was chosen due to its thermal stability and redox and acid-base properties. Having alkali metals as A cation increases the stability of the material as it decreases coke accumulation thanks to the increased CO_2 chemisorption capacity, due to the metal's Lewis basicity. In addition, alkali metals promote catalyst reducibility, generating new active sites. [2] $CaZrO_3$ has been investigated for steam reforming of methane, given its ability to improve coke gasification and enhance H_2 yield when used as promoter. This is due to favorable water adsorption that leads to water dissociation. As a matter of fact, $CaZrO_3$ can create a great number of vacancies in H_2 containing atmospheres, due to the reaction of the perovskite with H_2 to create oxygen deficient perovskite. Then, water can adsorb on those vacancies and therefore react with the reduced oxygen deficient perovskite to give H_2 and oxidized perovskite. [42], [43] As Dry Reforming of methane benefits as well from H_2 reductive atmosphere and water production from reverse water gas shift reaction, this interesting properties of $CaZrO_3$ can be applied also to our process, to have a stable catalyst with enhanced H_2 production.

Finally, another perovskite substrate was studied: $LaFeO_3$. $LaFeO_3$ is among the large common oxide perovskites that has an orthorhombic structure. It involves an FeO_6 octahedral unit, where La cations are implanted among the octahedral units. Here, Fe^{3+} ions are positioned at the centers of slightly distorted O^{2-}

octahedrals. [37] This support has, as the previous one, basic sites that favor CO_2 adsorbtion. In addition to that, the support has great affinity towards NO, being as a matter of fact one of the perovskite catalysts for NO reduction. Among other lanthanum perovskites oxides that catalyze NO reduction, $LaFeO_3$ was chosen for his stability at high temperatures in a reductive atmosphere: indeed, Fe^{3+} can be reduced only at very high temperatures. This allows the support to be stable in DRM conditions. [2], [44]

1.4. Real application scenarios

For industrial applications of this project, it is necessary to ensure a post-combustion CO_2 source and a NO source. Usually, NO_x coming out of combustion is around 150-1500 ppm, but nitric oxide is also produced in chemical processes (plastics, explosives...) using nitric acid or nitrates or nitrites, glass industry, metal surface treatment operations and nitric acid production (2-3% NO_x). Largest NO emissions are found in flue gases of power plants (0.1% NO, 1-5% O_2, 10-15% CO_2) and in tail gases of nitric acid production plants (0.2-1% NO, 2-3% O2). To ensure the flow of CO_2 and NO, it is necessary to have two industrial plants in proximity, which can be problematic for the territory and the quality of life of the inhabitants close to the plants. Therefore, an alternative can be to fuel a DRM plant with a gas turbine. This represents an interesting way to provide energy, as they can be built in a few months and employ relatively little capital, as well as being adaptable in size. [6] In gas turbines, NO emissions are due to high flame temperatures that involve oxygen reaction with nitrogen present in air (thermal NO), hydrocarbons and N_2 reaction (prompt NO) or organic nitrogen compounds that oxidize to NO when burnt (fuel bound to nitrogen (FBN) NO). [45]

Aside from the ecological side of the process, it is important to remember that this process would allow a double gain, given both the conversion of waste gasses, and the production of fuel with no CO_2 net emission, as CO_2 emissions are currently taxed due to their environmental impact. Taking a look at the efficiency of the process, gas turbines have net efficiencies of 30-40%, rising to 60% if heat recycling systems are used, compared with 46% and 60% for gas engines, which have much larger emissions. Furthermore, CO_2 produced by nitric oxide reduction can be re-fluxed into the reactor to react via DRM, ensuring a complete conversion of CO_2, and avoiding CO emission into the atmosphere.[46]

Finally, we must remember that this process allows NO conversion via waste and greenhouse gasses, avoiding the employment of substances with a higher economic value, representing an alternative to current NO emission treatment with NH_3.

1.5. Aim of this thesis

In this thesis the aim is to investigate the coking problem of nickel based catalysts for dry reforming of methane, and to offer a solution employing coke's oxidizing ability. To obtain stable and economic catalysts, different supports will be taken into consideration in order to determine which properties of the supports give stability and high catalytic activity to the process. Moreover, the type of coke produced during DRM will be related with the support, and to the easiness with which coke is removed by nitric oxide.

2. EXPERIMENTAL

2.1. Catalyst preparation

Catalysts were prepared via wet-chemical environmental-friendly synthesis, using water as solvent. In the first step the support was obtained, then nickel oxide nanoparticles were deposited in the second step. To obtain the active form of the catalyst, a reduction is needed, in order to reduce nickel oxide and obtain metallic nickel; this was carried out via a 5% H_2 treatment.

2.1.1. Supports

Four different supports have been taken into consideration.

Commercial γ-Al_2O_3 was used as first support (Merck, ≥ 99.95%) while the other three have been obtained via wet chemistry routes.

The second support is a $MgAl_2O_4$ spinel-coated γ-Al_2O_3. The spinel has been obtained via a coprecipitation synthesis, using precursors of the metals in stoichiometric amounts to obtain around 4 g of support. Precursors used were $Mg(OH)_2$ (Sigma-Aldrich, 95%) and γ-Al_2O_3 (Merck, ≥ 99.95%). $Mg(OH)_2$ precursor was dissolved in around 50 mL of H_2O with stoichiometric quantity of HNO_3 (65%, Sigma-Aldrich) to obtain the corresponding nitrate salt. Then, γ-Al_2O_3 was suspended in around 150 mL of H_2O and added to the previous solution. The solution was heated at 80 °C overnight under stirring until complete evaporation, then the product was grinded, and a powder was obtained. The powder was then calcined at 900°C for 6 h to obtain the spinel-alumina phase.

Finally, two perovskites have been synthetized via a citrate self-combustion route. [47] Stoichiometric quantities of precursors of the metal cations were dissolved in around 50 mL of water H_2O for each cation, and HNO_3 was used to dissolve cations if needed. Then citric acid monohydrate (Sigma-Aldrich, ≥ 99.0 %) was dissolved in H_2O and added to the solution of the cations in order to coordinate the cations as a complexing agent. The solution was then heated at 200°C under stirring conditions and basified with NH_4OH (Sigma-Aldrich, 28-30%) drop by drop until pH 7-8. This pH allows citric acid to be completely deprotonated, so to better disperse homogeneously the metal cations. The solvent was evaporated until reaching a solution volume of around 100 mL of solution, then the solution was transferred in a metal becker for the gel formation and self-combustion. The gel was formed under 100 mL of total solution volume, and it is composed by a network of metal cations/metal nitrates linked with citrate ligands. The gel was dried

overnight at around 100°C and then heated at 300°C to obtain the self-combustion (due to the exothermic decomposition of NH_4NO_3, formed from the reaction between nitric acid and ammonia), which then causes the decomposition of all the gel organic content, with a development of gaseous products (CO_2, H_2O and NO_x). A porous solid was formed after combustion, then this solid was grinded in order to obtain a powder which is finally calcined at the appropriate temperature to obtain the perovskite phase. $CaZrO_3$ has been obtained starting from precursors $ZrO(NO_3)_2$ and $Ca(CO_3)_2$ (Sigma-Aldrich, ≥ 99%); minimum quantities of HNO_3 were used to dissolve $Ca(CO_3)_2$. Citric acid was used in a molar ratio citric acid/total number of cations of 1.9, ratio optimized by the research group. Then the product was calcined in a muffle for 6 h at 1400°C (heating rate: 5 °C/min) to obtain minimum impurities.

$LaFeO_3$ was synthetized using La_2O_3 (Sigma-Aldrich, ≥ 99.9%), dissolved in H_2O with the aid of HNO_3, and $Fe(NO_3)_3 \cdot 9H_2O$ (Sigma-Aldrich, ≥ 98%). Citric acid was used in a molar ratio citric acid/total number of cations of 1.1, ratio optimized by the research group for ferrites. The product was finally calcined in a muffle for 6 h at 800°C (heating rate: 5 °C/min) to obtain the final product.

After calcination treatment, all solid samples obtained were grinded to obtain solid powders. The supports have been obtained with a yield of around 80-90%.

2.1.2. Nickel oxide nanoparticles deposition

Nickel oxide deposition has been obtained by a simple wet impregnation. $Ni(NO_3)_2 \cdot 6H_2O$ has been used as precursor; stoichiometric amount of precursor was dissolved in around 20 mL of H_2O and then added to the suspension of the specific support in water (around 50 mL), to obtain catalysts with a $13\%_{w/w}$ loading of metallic Nickel after H_2-reductive treatment. All samples were dried at 80°C overnight under stirring conditions, then kept for 2 hours at 120°C and the solid obtained was grinded to powder. Finally, samples were calcined in a muffle furnace at 650°C for 6 hours (heating rate: 5°C/min).

2.1.2. Reductive treatment

To obtain the active form of the catalysts, a reductive treatment in 5% H_2 flow in Ar or He was used to reduce NiO nanoparticles to Ni. The temperature for the reduction was chosen after H_2-TPR experiments. The reduction treatment was carried out in situ before each DRM coupled with NO reduction catalytic test took place.

2.2. Characterization of samples

X-ray powder diffraction (XRD) measurements were performed to identify the crystalline phases present in the samples, thanks to JCPDS database references for diffraction lines positions and intensity. A Bruker D8 Advance diffractometer was employed, equipped with a Cu K source (λ=0.154 nm) and operating in Bragg-Brentano geometry. XRD patterns were acquired in a 2θ=20-80° range, with steps of 0.02° and well time of 0.35 s.

H_2-temperature programmed reduction (TPR) was performed to determine the samples reducibility on a Micromeritics AutoChem II 2920 equipped with a TCD detector for H_2 concentration monitoring. 50 mg of sample were heated up until 900 °C for all samples and 600°C for perovskites samples under a 50 mL/min flow of 5 vol% H_2 in Ar, with a ramp of 10 °C/min.

H_2 pulsed-chemisorption was performed on all catalysts to determine Ni dispersion and average particles size after an in situ reductive treatment. The same instrument as for TPR was used. The following procedure was employed: first, about 50 mg of sample were reduced under 5 vol% H_2 in Ar at 900 °C for NiO/Al_2O_3 and $NiO/MgAl_2O_4$-Al_2O_3 samples and at 600°C for the perovskite catalysts. Then catalysts were cooled down to 40 °C in the same environment, and, finally, H_2 was repeatedly pulsed at the same temperature for 20 times; the total amount of chemisorbed H_2 was quantified through the TCD detector.

N_2 physisorption was carried out on a Micromeritics ASAP2020 analyser, to calculate the specific surface area (SSA) by means of the Brunauer-Emmett-Teller (BET) model. Samples were degassed at 300°C for 6 h under reduced pressure (around 0.013 mbar) before adsorption took place. Then, analysis was conducted at -196 °C, collecting 80 points between at p/p^0 = 0.002 and p/p^0 = 1 (linear range of the adsorption isotherm).

Scanning electron microscopy (SEM) images were acquired with a Zeiss SUPRA 40 V P microscope, setting the electron acceleration voltage at 5 or 10 kV. Energy-dispersive X-ray analysis (EDX) was coupled to SEM for elemental quantification, at 20 kV electron acceleration voltage, probing a large area of sample (rectangle of hundreds of µm each side).

X-ray photoelectron spectroscopy (XPS) was performed with a Thermo Scientific ES-CALAB QXi spectrometer, employing a monochromatized Al Kα source (hv = 1486.68 eV) and a charge compensation gun. Survey spectra were acquired at pass energy 100 eV, resolution 0.5 eV/step and dwell time 25 ms/step. Elemental quantification was carried by integration photopeaks after Shirley-type background subtraction.

2.3. Catalytic Tests

2.3.1. Dry Reforming and Nitric Oxide reduction

Dry reforming of methane coupled with nitric oxide reduction was performed on the four samples in a quartz tube fix bed reactor (ID 6 mm), loaded with about 50 mg of catalyst sandwiched between two quartz wools, with a thermocouple mounted upstream of the bed. The reaction mixture was composed of 5 vol% CH_4, 5 vol% CO_2, 1 vol% NO and Ar, for a total flow rate of 100 mL/min and a GHSV of about 12000 h^{-1}, depending on the catalyst. Further experiments were conducted using a reaction mixture of 25 vol% CH_4, 25 vol% CO_2, 1 vol% NO and Ar, for a total flow rate of 100 mL/min. Before the catalytic experiments, a reductive treatment was performed to obtain the active form of the catalysts, using a 5% H_2 flow in Ar and increasing the temperature until 900°C for Al_2O_3 based samples and 600°C for perovskites samples, as suggested by TPR measurements, with a ramp of 10 °C/min. Then catalytic measurements were conducted at 750 °C. The reaction mixture was analyzed by an on-line Agilent Technologies 7890A gas-chromatograph, equipped with a TCD detector; a condenser to trap the generated water was employed between the reactor and the GC.

2.3.2. O_2-TPO

Temperature-programmed oxidation was conducted in order to examine the quantity and type of coke that deposits onto the catalyst during the catalytic tests. Around 25 mg of post-reaction catalysts was loaded between two quartz wools into a quartz tube reactor coupled with a thermocouple, as done in the catalytic tests before. A flow of 5% O_2 in He, for a total flow rate of 100mL/min, was used to carry out TPO measurements, and the temperature was increased in a ramp from room temperature to 900°C (ramp of 10 °C/min) and then decreased at 10°C/min. The reaction mixture was analyzed by an on-line Agilent Technologies 7890A gas-chromatograph, equipped with a TCD detector; a condenser to trap the generated water was employed between the reactor and the GC.

2.3.3. NO-TPO

Temperature-programmed oxidation was carried out in order to understand how NO can remove the carbon formed that deposits onto the catalyst during the catalytic tests. Around 20 mg of post-reaction catalysts was loaded between two quartz wools into a quartz tube reactor coupled with a thermocouple, as done in the catalytic tests before. A flow of 5% NO in Ar, for a total flow rate of 100mL/min, was used to carry out TPO

measurements, while the temperature was increased in a ramp from room temperature to 750°C (ramp of 10 °C/min) and then kept at 750°C for 2 hours. The reaction mixture was analyzed by an on-line Agilent Technologies 7890A gas-chromatograph, equipped with a TCD detector; a condenser to trap the generated water was employed between the reactor and the GC.

3. PHYSICOCHEMICAL CHARACTERIZATION

3.1. Characterization of calcined catalysts

3.1.1. XRD results

XRD is a helpful technique that allows do identify crystalline phases of the bulk. XRD patterns of the four calcined catalysts are here reported; for each catalyst both the support and the post impregnation sample have been characterized. All graphs, showing comparison among different samples, report normalized intensities of XRD patterns.

1 - NiO/Al_2O_3

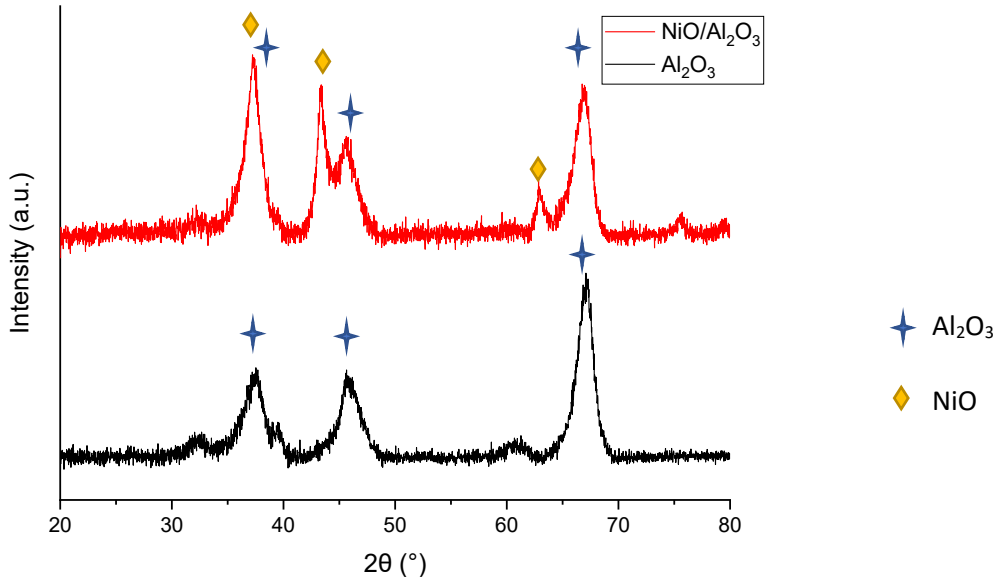

Figure 7-XRD pattern of the γ-Al_2O support (black) and of the post-impregnation (red) catalyst

XRD patterns of the first support and impregnated catalyst are reported in figure 7. The support γ-Al_2O_3 is present in the catalyst after impregnation; however, there is a slight anticipation of its reflexes, which is clear in the reflex at 2θ= 67,1° of Al_2O_3 that shifts to 2θ= 66,9° after impregnation and calcination. This might be due to the presence of $NiAl_2O_4$ spinel, that can easily be formed during calcination [30]. However, from XRD pattern its presence is not clear as its reflexes are hindered by Al_2O_3 broad reflexes. So, further analysis will be performed in order to understand if the spinel is present (see chapter 3.1.6.).

2 - $NiO/MgAl_2O_4$-Al_2O_3

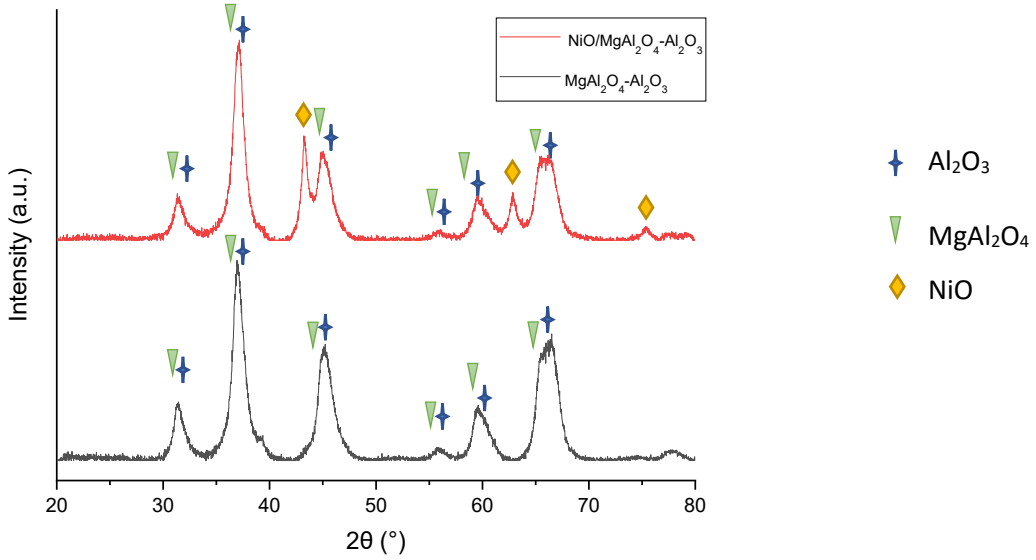

Figure 8- XRD pattern of the $MgAl_2O_4$-Al_2O_3 support (black) and of the post-impregnation catalyst (red)

In figure 8 XRD patterns of our second support $MgAl_2O_4$ and $NiO/MgAl_2O_4$-Al_2O_3 catalysts are shown. The support has broad peaks due to the overlap of different crystalline phases, in particular $MgAl_2O_4$ and Al_2O_3. The presence of both phases can be seen by looking at the very broad peak at 2θ= 65,3°-67,8°, where the reflexes of the two compounds are more separate; moreover, the presence of both also accounts for the asymmetry of the reflexes at 2θ=45° and 2θ=60°. We can clearly see the presence of NiO in the impregnated catalyst thanks to its characteristic peaks, while $NiAl_2O_4$ that could be formed during calcination have peaks that would overlap with both $MgAl_2O_4$ and Al_2O_3, so further experiments are needed (see chapter 3.1.4.).

3 - $NiO/CaZrO_3$

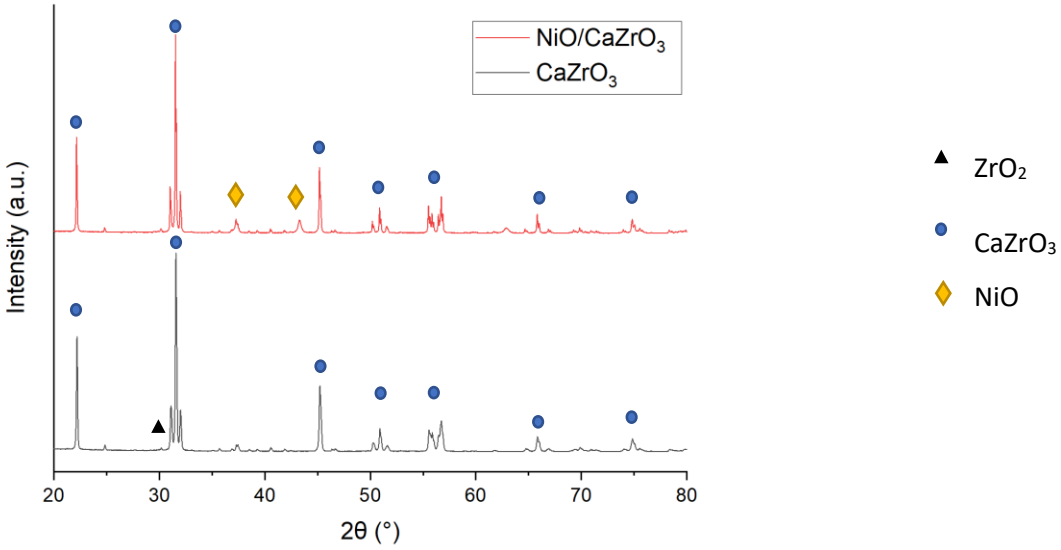

Figure 9- XRD pattern of the $CaZrO_3$ support (black) and of the post-impregnation catalyst (red)

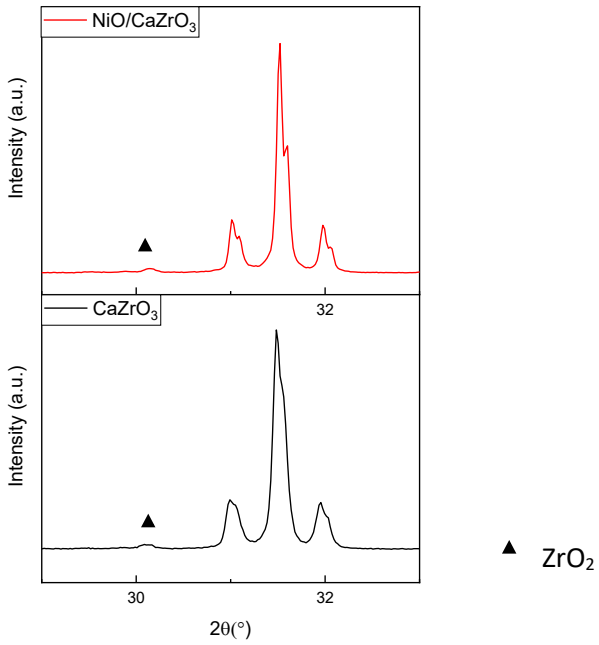

Figure 10- Zoom of the XRD pattern in the range 2ϑ =28-34° of the $MgAl_2O_4$-Al_2O_3 support (black) and of the post-impregnation catalyst (red)

XRD pattern of the third support (Figure 9) shows the perovskite $CaZrO_3$. The perovskite phase was present, with little traces of ZrO_2 impurities that can be seen zooming at around 2θ=30°, as showed in figure 10. The perovskite has an orthorhombic structure, as seen by XRD peaks; this structure is the stable perovskite structure for the calcination temperature chosen (1400°C), while after 1900°C cubic structure is formed.[48] After impregnation, NiO was clearly seen at 2θ=37,3° and 2θ=47,3°.

4 - $NiO/LaFeO_3$

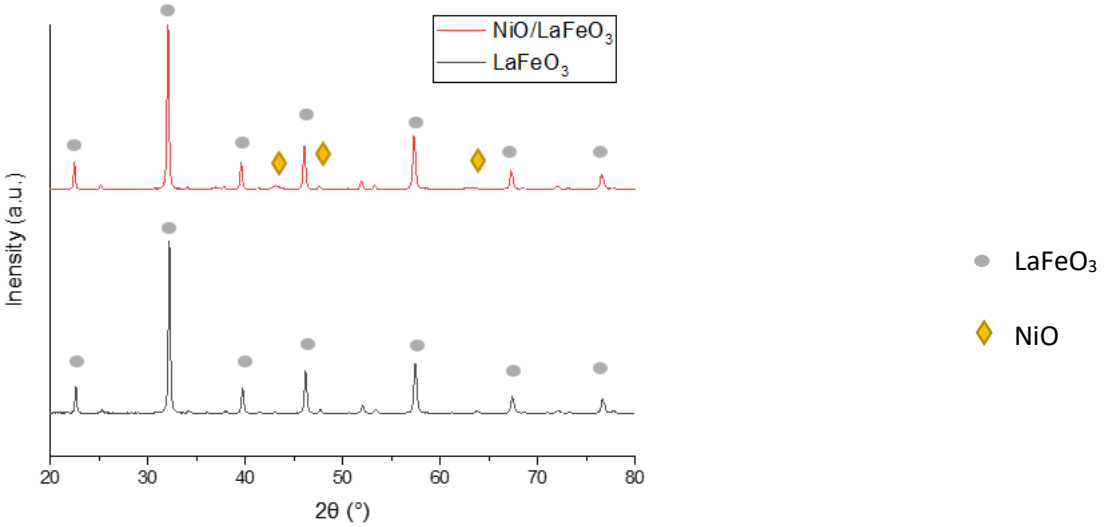

Figure 11- XRD pattern of the $LaFeO_3$ support (black) and of the post-impregnation catalyst (red)

In figure 11, our last support $LaFeO_3$ and the catalyst $NiO/LaFeO_3$ after calcination, are compared. The perovskite $LaFeO_3$ is the only crystalline phase present in the support and it has an orthorhombic structure, as expected. [49] NiO broad peaks appear clearly after impregnation and calcination, and no modification of the perovskite support was observed.

3.1.2. N_2 PHYSISORPTION

N_2 physisorption allows to measure porosity; it is an important parameter as pores increase the surface area of the catalyst, which can improve the catalytic performance as reactants can adsorb both on the outer-surface of the sample and on its pores. [38] Physisorption isotherms were measured by degassing the samples to remove volatiles (300°C, 6h), then nitrogen was fluxed to ensure absorption at liquid nitrogen temperature (77K). The quantity of gas adsorbed (mmol/g) was plotted against the equilibrium relative pressure p/p^0, where p^0 is the saturation pressure of the pure adsorptive at the operational temperature.[50] The so obtained isotherms are showed below:

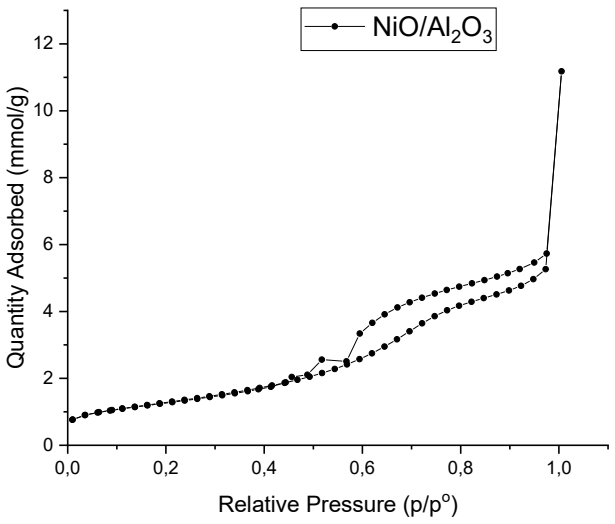

Figure 12- N_2 adsorbtion-desorption isotherm of NiO/Al_2O_3

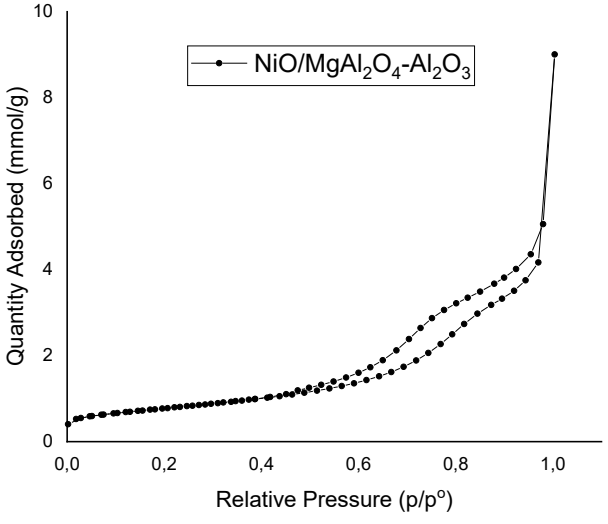

Figure 13- N_2 adsorbtion-desorption isotherm of $NiO/MgAl_2O_4$-Al_2O_3

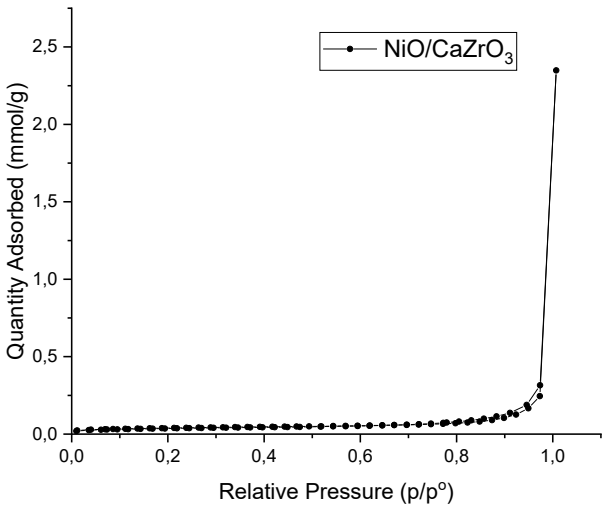

Figure 14- N_2 adsorbtion-desorption isotherm of $NiO/CaZrO_3$

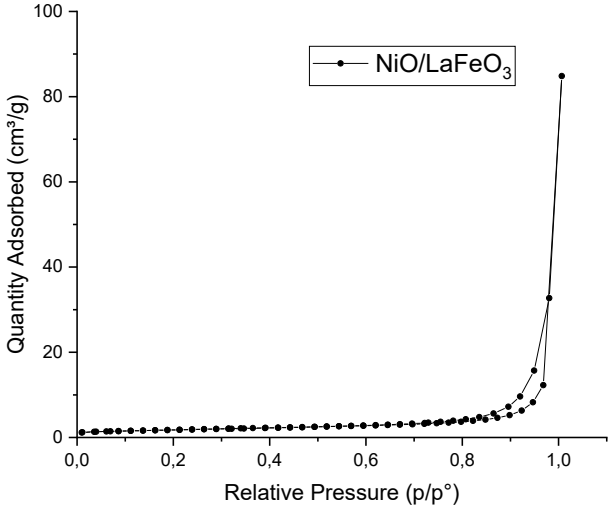

Figure 15- N_2 adsorbtion-desorption isotherm of $NiO/LaFeO_3$

The linear plot of the physisorption isotherm was interpreted through the 1985 IUPAC classification. [50] Al_2O_3 based samples showed isotherms with a shape between isotherm type II and IVa (figures 12 and 13). The catalyst is thus characterized by the behavior of mesoporous material and a macroporous or nonporous porosity, which causes the amount of adsorbate to change to infinity at $p=p^0$. The hysteresis loop is a mix of type H1, i.e. associated with materials with uniform mesopores within a narrow range. On the other hand, perovskites samples (figures 14 and 15) showed type III isotherm, that accounts for macroporous/ nonporous porosity, and a hysteresis loop H1 type due to the mesoporosity of the materials.

Thanks to Brunauer-Emmett Teller method (BET), an estimation of the values of the surface area of the different samples can be made, and is reported below in table 1 below:

Table 1-Post-impregnation catalysts have been analyzed by calculating BET surface areas via N_2-physisorption measurements

Sample	**BET surface area** (m^2/g)
NiO/Al_2O_3	104.6794
$NiO/MgAl_2O_4$	61.5471
$NiO/CaZrO_3$	3.0267
$NiO/LaFeO_3$	6.3601

Samples show different values of surface area based on the properties of the material and synthesis conditions. As NiO deposition was done with the same synthesis conditions (13%$_{w/w}$, 650°C, 6h), it is the differences among the supports of the catalysts that cause the difference of values in surface area. Commercial Al_2O_3 support showed the higher surface area, that diminished at around half its value when coated with $MgAl_2O_4$, which needed and additional calcination treatment at 900°C, with consequent sintering. Perovskites samples showed the lower values of surface area, as expected [2]. $CaZrO_3$ perovskite needed high temperature of calcination (1400°C) to obtain low amounts of ZrO_2 impurities, so surface area is the lowest due to sintering of the support. $LaFeO_3$ perovskite, on the other hand, was obtained as pure crystalline phase using a calcination temperature of 900°C, that allowed to obtain higher surface areas (double with respect to $CaZrO_3$).

Moreover, N_2 physisorption gives information about the pore size distribution of the different materials via the Barrett, Joyner, and Halenda method (BJH), based on the physisorption equilibrium isotherms. [51] BJH method utilize the Kelvin equation under the assumption of having an equilibrium between the gas phase and the adsorbed phase during desorption, determined by two mechanisms: physical adsorption of N_2 molecules on the pore walls and capillary condensation in the inner capillary volumes. Kelvin equation (7) relates vapor pressure depression to capillary radius, allowing to have a relationship between the volume of the capillary condensate and the relative pressure: [52]

$$\log P/Po = -2\sigma V/(8.316 * 10^7 * 2.303 Trk) \quad (7)$$

With σ the surface tension of liquid nitrogen, V the liquid molar volume of nitrogen, rk the radius of capillary in cm and T the absolute temperature in K.

In the following figures (16-19) desorption isotherms were used for BJH analysis.

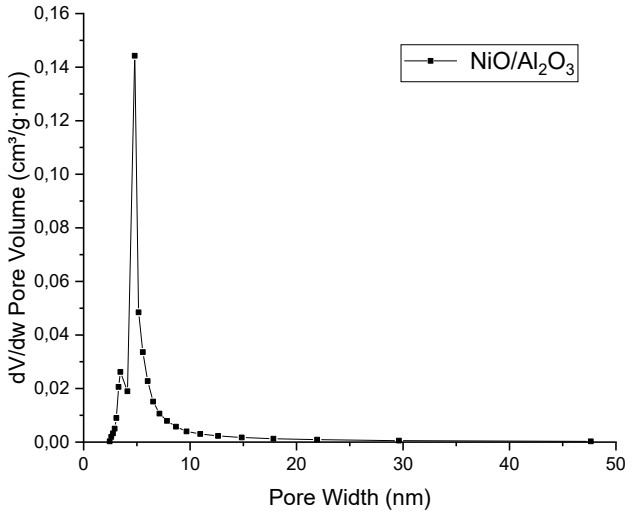

Figure 16- Pore distribution on NiO/Al_2O_3

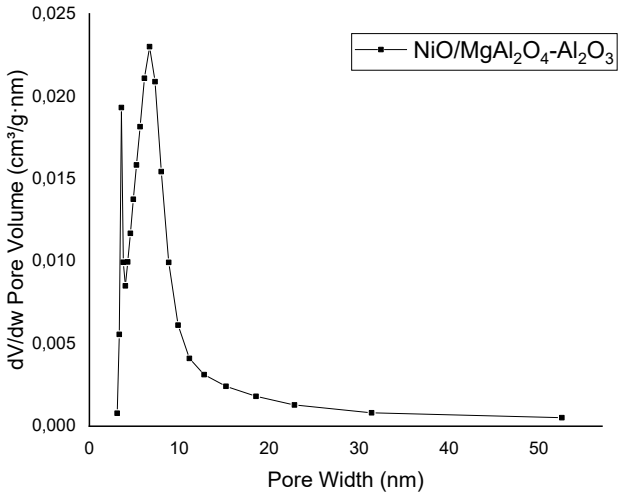

Figure 17- Pore distribution on $NiO/MgAl_2O_4$ -Al_2O_3

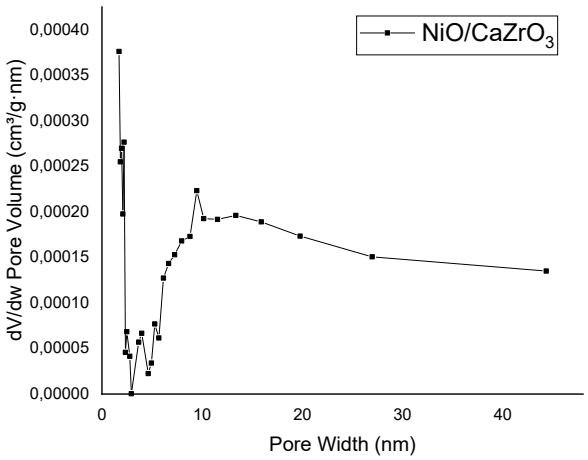

Figure 18- Pore distribution on $NiO/CaZrO_3$

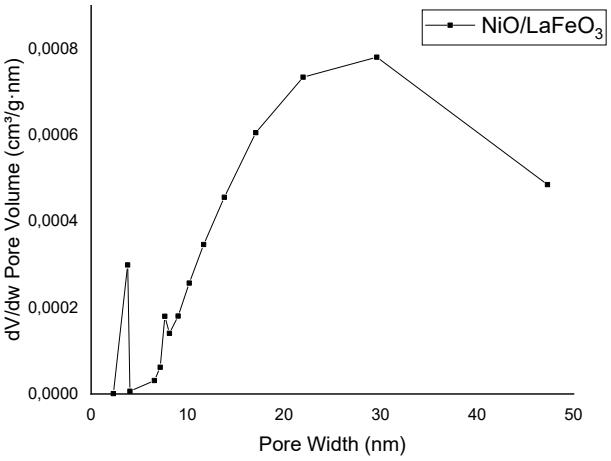

Figure 19- Pore distribution on $NiO/LaFeO_3$

The pores are mainly distributed for $NiO/MgAl_2O_4$-Al_2O_3 in peaks between 3 and 4 nm and between 4 and 6 nm pore width and for NiO/Al_2O_3 around 3.5 nm and between 4 and 9 nm. Being the pore width distribution between 2 and 50 nm, those catalysts are mesoporous materials. [53]

Perovskites samples have bigger and fewer pores than the alumina-based samples, and overall, less porosity. Pore volume is two order of magnitude $NiO/CaZrO_3$ have a more varied pore size distribution, mainly before 2 and after 6 nm; this variety in its morphology is also appreciable in SEM images of the catalyst. $NiO/LaFeO_3$ catalyst have its pore size distribution mainly after 10 nm of pore width, and pore volume double than $NiO/CaZrO_3$, in accordance with their surface area values.

3.1.3. SEM/EDX

SEM coupled with EDX was performed on the 4 supports and on the respective post-nickel impregnation catalysts: Al_2O_3, NiO/Al_2O_3, $MgAl_2O_4$-Al_2O_3, $NiO/ MgAl_2O_4$-Al_2O_3, $CaZrO_3$, $NiO/CaZrO_3$, $LaFeO_3$, $NiO/LaFeO_3$. Here, in figures 20-35, SEM images are reported to investigate the morphology of the samples, while EDX results can provide the compositions of the post-impregnation catalysts with a depth of hundreds of nm.

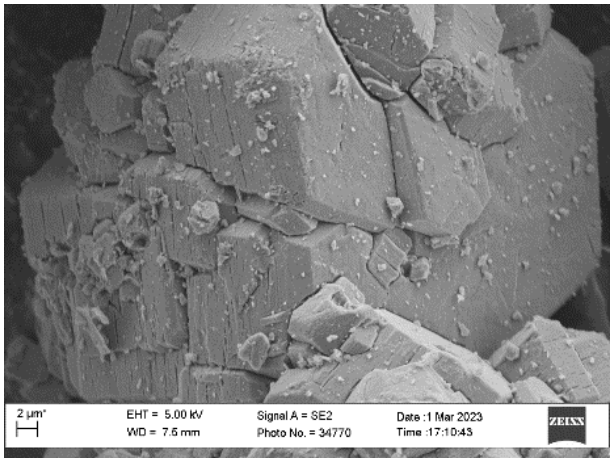

Figure 20- SEM image of Al_2O_3 at 5000x magnification

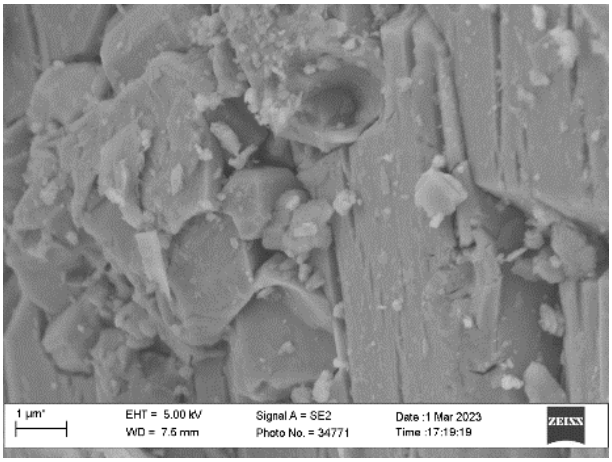

Figure 21- SEM image of Al_2O_3 at 25000x magnification

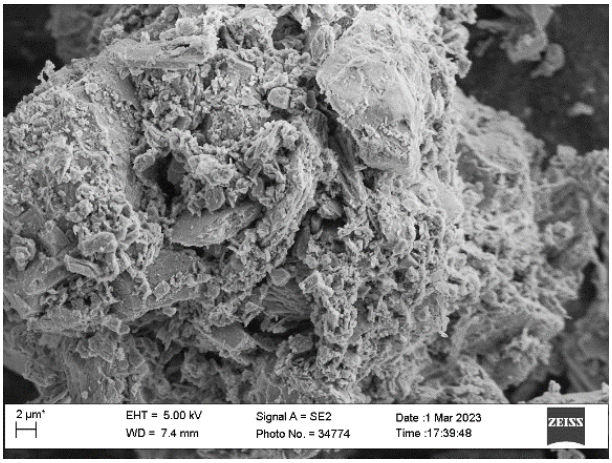

Figure 22- SEM image of NiO/Al_2O_3 at 5000x magnification

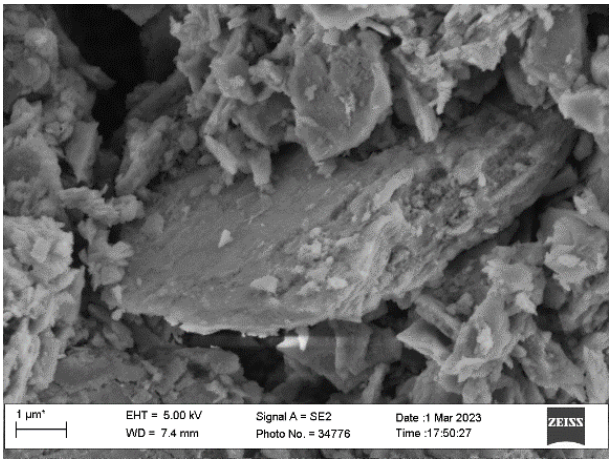

Figure 23- SEM image of NiO/Al_2O_3 at 25000x magnification

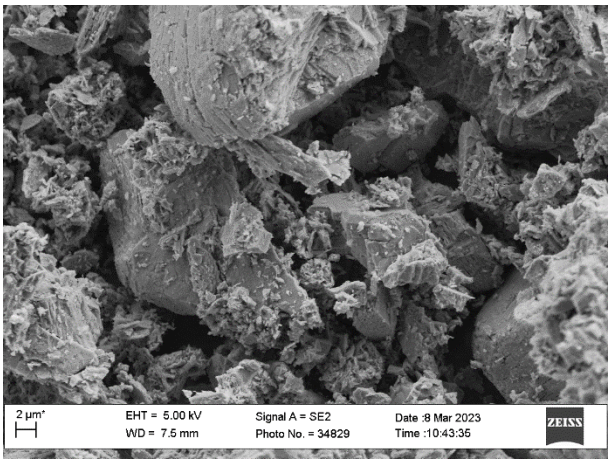

Figure 24- SEM image of $MgAl_2O_4$-Al_2O_3 at 5000x magnification

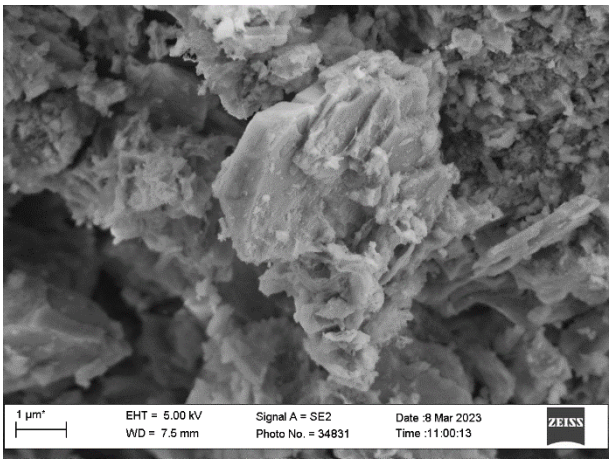

Figure 25- SEM image of $MgAl_2O_4$-Al_2O_3 at 25000x magnification

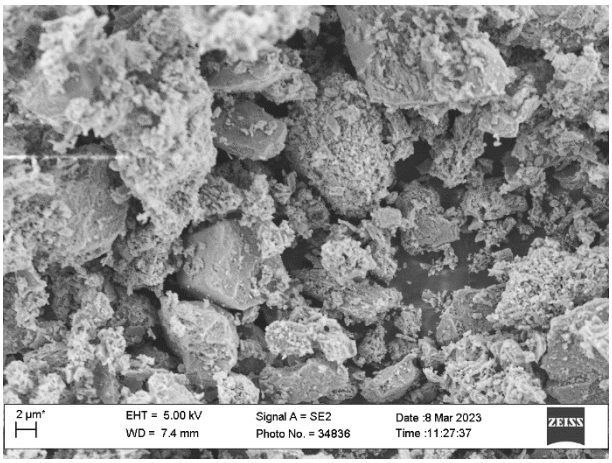

Figure 26- SEM image of NiO/$MgAl_2O_4$-Al_2O_3 at 5000x magnification

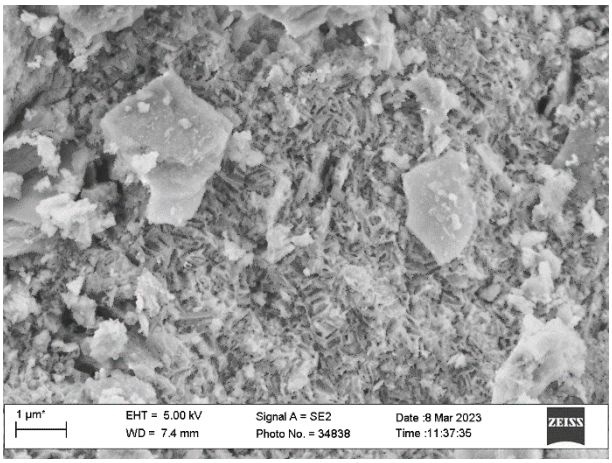

Figure 27- SEM image of NiO/$MgAl_2O_4$-Al_2O_3 at 25000x magnification

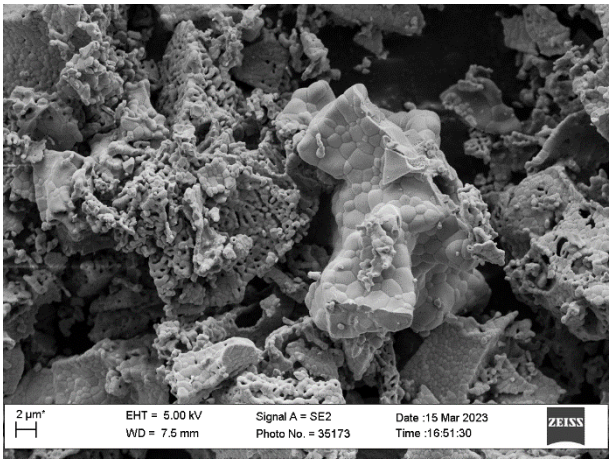

Figure 28 - SEM image of $CaZrO_3$ at 5000x magnification

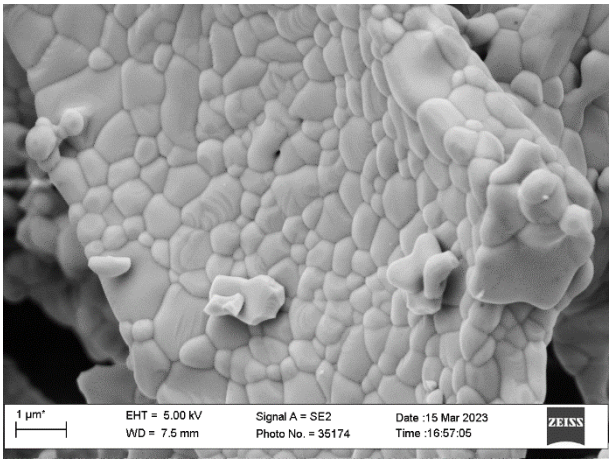

Figure 29 - SEM image of $CaZrO_3$ at 25000x magnification

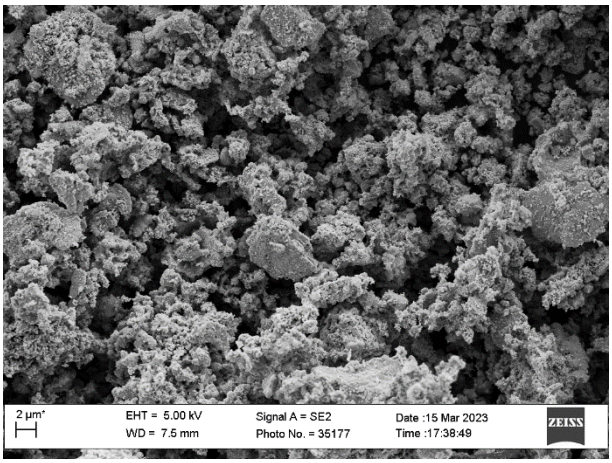

Figure 30 - SEM image of $NiO/CaZrO_3$ at 5000x magnification

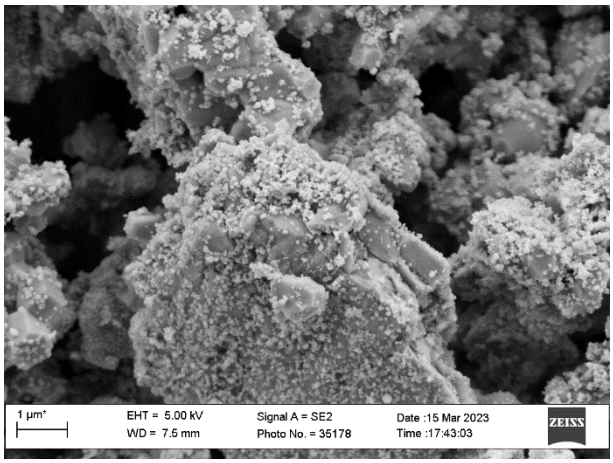

Figure 31 - SEM image of $NiO/CaZrO_3$ at 25000x magnification

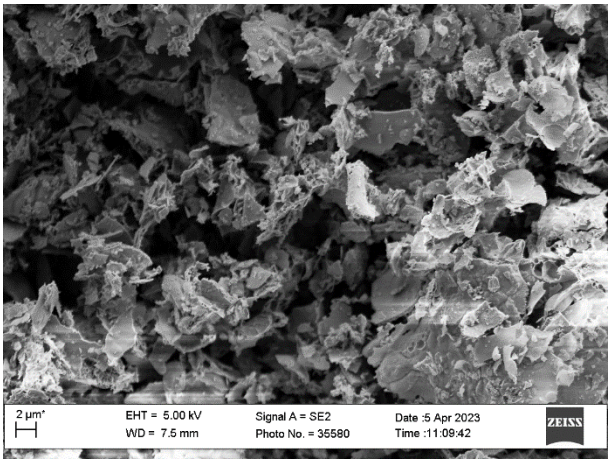

Figure 32 - SEM image of $LaFeO_3$ at 5000x magnification

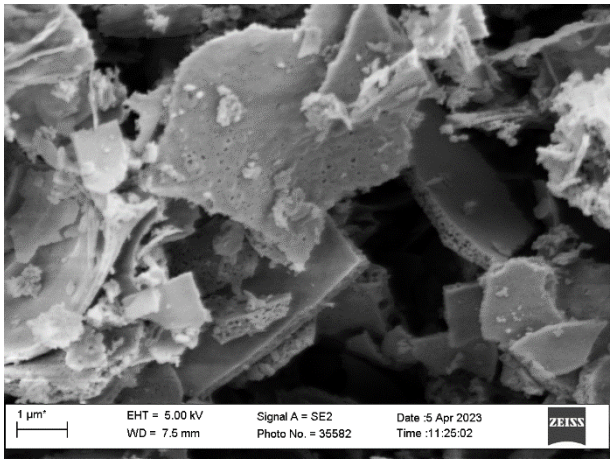

Figure 33 - SEM image of $LaFeO_3$ at 25000x magnification

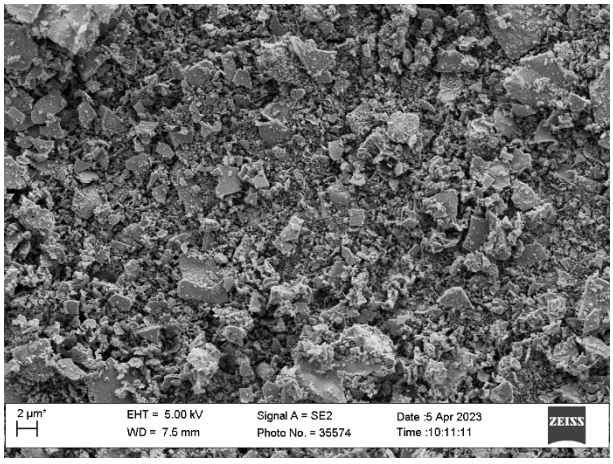

Figure 34 - SEM image of $NiO/LaFeO_3$ at 5000x magnification

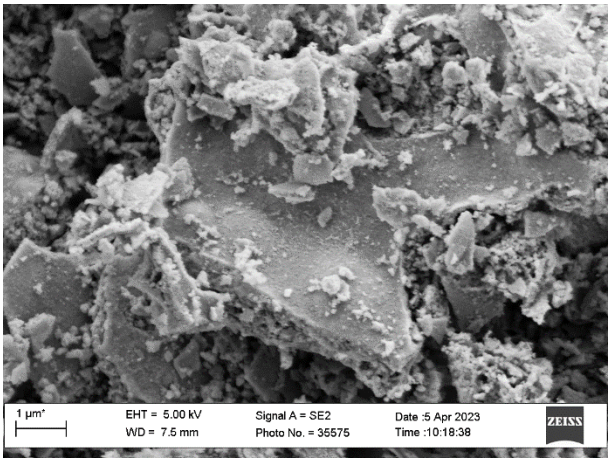

Figure 35 - SEM image of $NiO/LaFeO_3$ at 5000x magnification

From SEM images analysis no particular information was retrieved about the morphologies of the samples, while EDX measurements allowed to analyze the compositions of the materials with a depth of around

hundreds of nm. At this depth, the element quantification is representative of an almost "bulk" composition- so to say that the compositions obtained are not strictly bulk compositions, but are representative of a much higher depth than XPS compositions.

EDX measurement were made on post-impregnation catalysts to study their composition and compare EDX results with nominal results expected, calculated using the stoichiometry employed during the synthesis. Results are shown in table 2 below:

Table 2- EDX elemental quantifications are here reported, calculated without considering the oxygen content, by analyzing square areas of around 400-500 µm of samples. Post-impregnation catalysts are taken into consideration, and EDX results are compared with nominal compositions based on the employed stoichiometry.

Atomic Composition (at. %)

Sample	***Analysis***	***Ni***	***Al***	***Mg***	***Ca***	***Zr***	***La***	***Fe***
NiO/Al_2O_3	Nominal	16.9	83.1					
	EDX	22.9	77.1					
$NiO/MgAl_2O_4$-Al_2O_3	Nominal	11.1	73.5	15.4				
	EDX	12.3	76.4	11.3				
$NiO/CaZrO_3$	Nominal	15.8			42.1	42.1		
	EDX	23.8			37.9	38.3		
$NiO/LaFeO_3$	Nominal	20.8					39.6	39.6
	EDX	24.4					36.7	38.9

The table shows a good accordance between expected compositions and EDX results for almost all samples. However, Ni atomic compositions are in general higher than the theoretical ones. This might be due to the impregnation synthesis used to deposit nickel onto the supports; however more information will be gained by comparing EDX results and XPS compositions in chapter 3.1.6, in order to understand how the elements are distributed in the bulk and surface of the catalysts.

EDX atomic ratios obtained on both supports and post-impregnation catalysts are compared in table 3, in order to understand if the support composition changed with impregnation.

Table 3- EDX elemental quantifications are here reported as ratio of cations of the support, calculated without considering the oxygen content, by analyzing square areas of around 400-500 µm. Both supports, post-impregnation and post-reduction catalysts have been taken into consideration. γ-Al_2O_3 wasn't considered as the support has only one cation.

Atomic Composition (at. %)

Sample	***Al/Mg***	***Ca/Zr***	***La/Fe***
$MgAl_2O_4$-Al_2O_3	8.3		
NiO/$MgAl_2O_4$-Al_2O_3	6.8		
Ni/$MgAl_2O_4$-Al_2O_3	7.0		
$CaZrO_3$		0.9	
NiO/$CaZrO_3$		1.0	
Ni/$CaZrO_3$		1.0	
$LaFeO_3$			1.0
NiO/$LaFeO_3$			0.9
Ni/$LaFeO_3$			1.1

The ratio among the cations is kept almost constant after impregnation of Ni. Only Al/Mg ratio in *NiO/$MgAl_2O_4$-Al_2O_3* catalyst slightly differs from the ratio measured for *$MgAl_2O_4$-Al_2O_3* support; this might be due to the migration of ions that happens during calcination, when the support is modified to form $NiAl_2O_4$ spinel (see chapter 3.1.1. and 3.1.4.)

3.1.4. H_2-temperature programmed reduction (H_2-TPR) and XRD patterns of the reduced catalysts

H_2-TPR experiments were conducted on all post-impregnation catalysts in order to study the reducibility of nickel oxide particles; a gas mixture of 5% H_2/Ar and a temperature ramp from 25°C to 900°C at 10°C/min were employed. Hydrogen consumption was measured by TCD detector, and the data achieved allowed to measure the quantity of H_2 consumed by the catalysts to be in their active phase. Moreover, XRD patterns of

the post-reduction catalysts will be gained to obtain information about the catalysts in their active phase; their XRD pattern will be showed together with the calcined catalysts, i.e. the catalysts before the reductive treatment.

1 - NiO/Al_2O_3

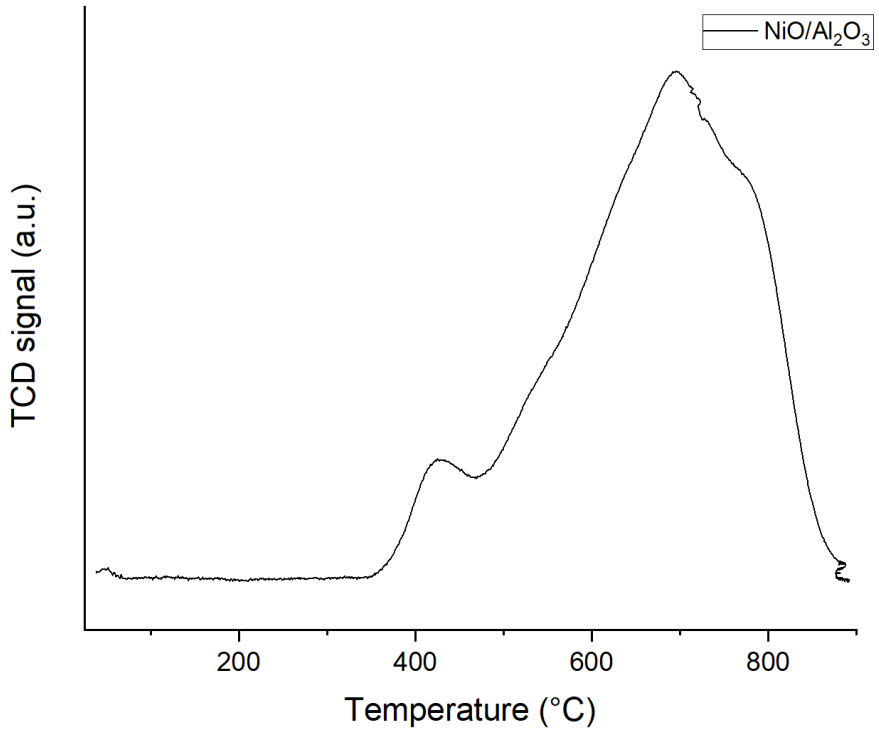

Figure 36- H_2-TPR experiment on NiO/Al_2O_3

NiO/ γ-Al_2O_3 exhibited 2 reduction peaks at 400 °C and 700 °C (figure 36). The first reduction peak is to be attributed to NiO weakly interacting with γ-Al_2O_3. The second peak has the maximum at 700°C and a shoulder at 780°C. This peak at high temperatures is due to a strong interaction of Nickel and alumina, while the shoulder at reduction temperatures above 700°C is probably due to the formation of $NiAl_2O_4$ spinel, as reported in literature. [54]–[56] As a matter of fact, γ-Al_2O_3 is prone to the formation of the nickel spinel, as at high calcination temperatures nickel ions gain sufficient energy to integrate in the alumina lattice to produce the spinel. [30]

After H_2-TPR, XRD analysis was made to see the crystalline phases present in the post reduction sample. The XRD pattern of the post reduction catalysts is shown in the graph below, together with the pre-reduction catalyst (post-calcination NiO/Al_2O_3) (figure 37):

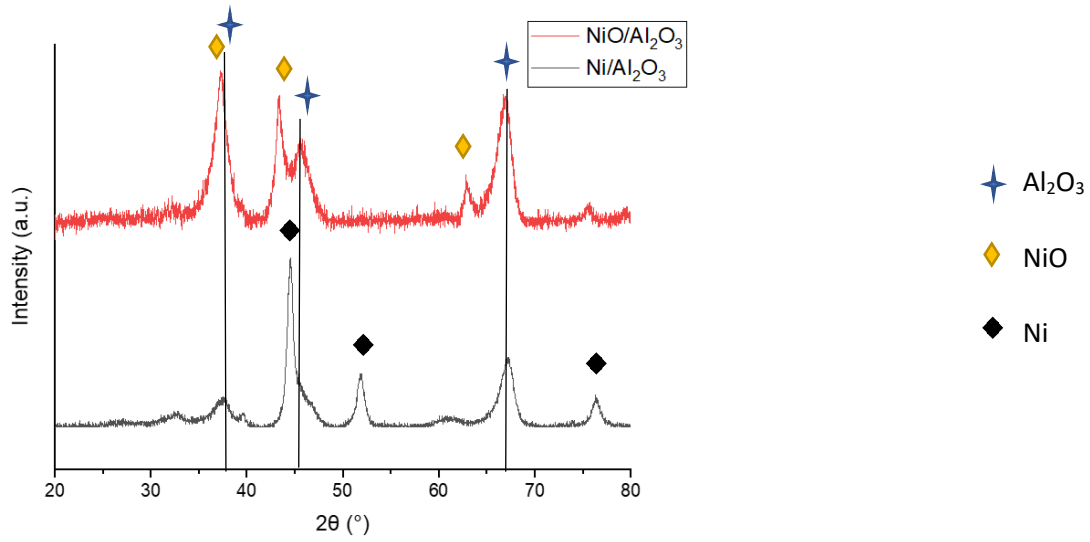

Figure 37- XRD pattern of NiO/Al_2O_3 catalyst post-calcination (red) and post-reduction (black)

XRD pattern show that all NiO phase is completely transformed into metallic Ni due to H_2 reduction. No information could be retrieved about the presence or the reduction of $NiAl_2O_4$ spinel due to its peak positions that overlap with Ni, NiO and Al_2O_3 peaks; so further analysis will be needed (see XPS analysis, chapter 3.1.6.)

2 - $NiO/MgAl_2O_4$-Al_2O_3

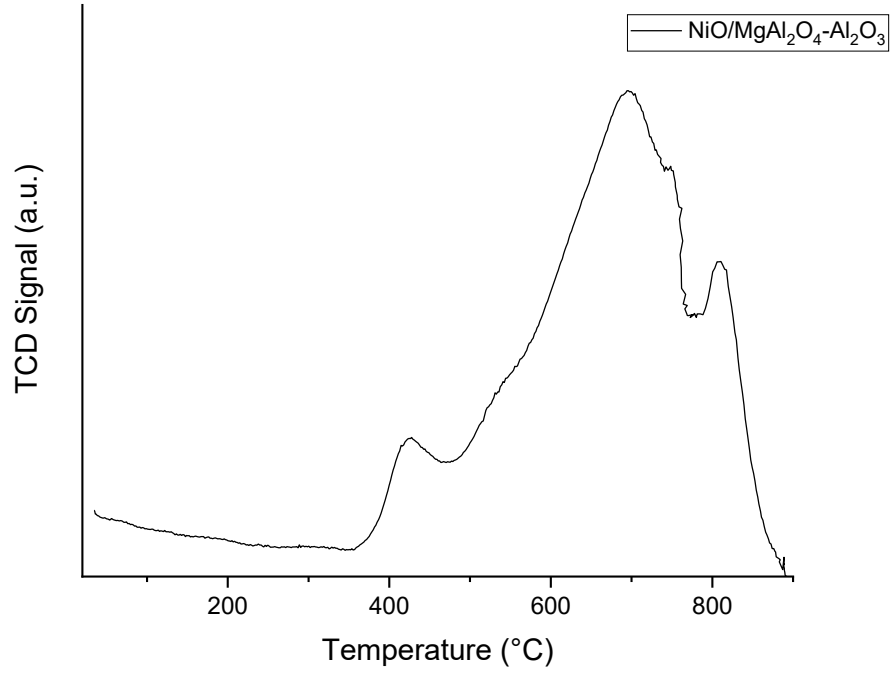

Figure 38- H_2-TPR experiment on $NiO/MgAl_2O_4$-Al_2O_3

For $NiO/MgAl_2O_4$-Al_2O_3 (figure 38), a first peak at around 400°C was detected, due to surface NiO weakly interacting with $MgAl_2O_4$, as for the previous catalyst. A second and a third peak were detected respectively at 700°C and 800°C. High reduction temperatures are due to spinels strongly interacting with Nickel particles. The second peak is very broad and has a left shoulder before 600°C, and a right shoulder at around 746°C, suggesting different strength of interaction. Among the peaks between 600°C and 800°C, nickel could enter into the magnesium aluminum spinel to form nickel aluminum spinel. To investigate this possibility, XRD of the reduced sample was analyzed in the graph below (figure 39):

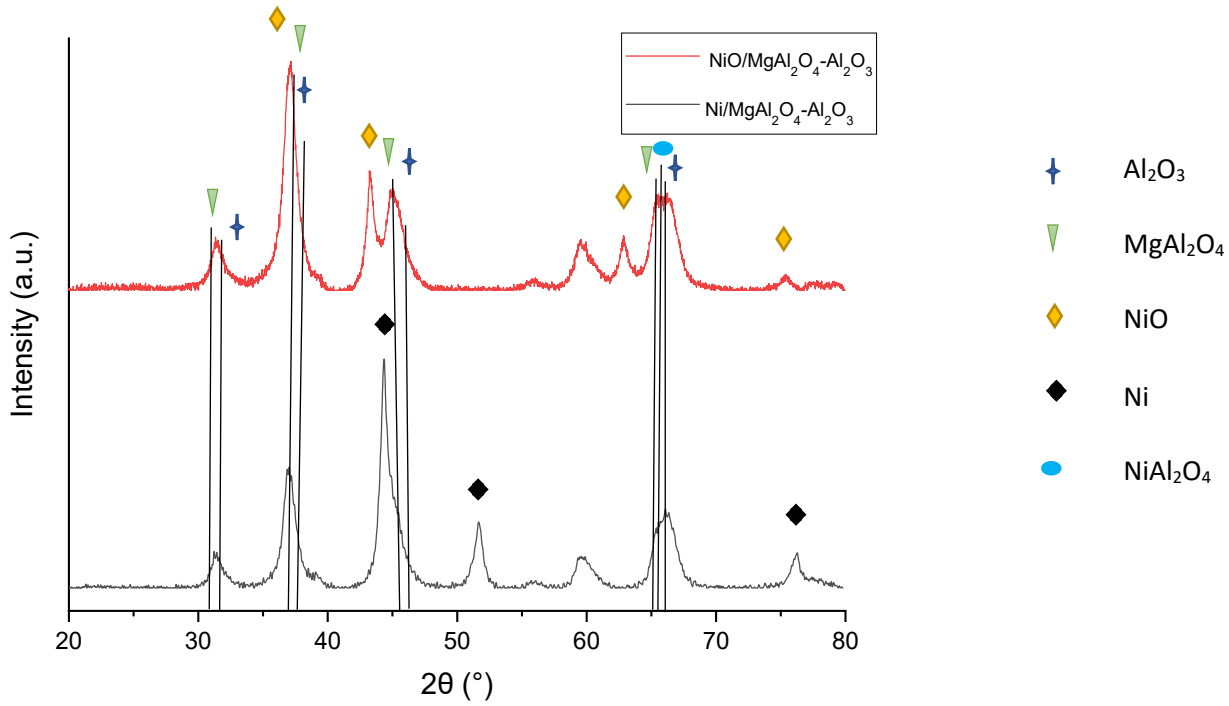

Figure 39 - XRD pattern of $NiO/MgAl_2O_4$-Al_2O_3 catalyst post-calcination (red) and post-reduction (black)

XRD pattern of the post-calcination and post-reduction catalyst showed differences in the peak at around $2\theta = 66°$. The broad peak is symmetric in $NiO/MgAl_2O_4$-Al_2O_3, and has the contribution of $MgAl_2O_4$-Al_2O_3, Al_2O_3 and possibly $NiAl_2O_4$ reflexes. When the catalyst is reduced, we can see a significant change in shape of the peak, that accounts for the loss of a contribution in its left shoulder. At this 2θ, the latter contribution is most probably due to the presence of the spinel, that can be reduced (totally or partially) during the reductive treatment to gain the active phase of the catalyst. Spinel's peaks are always between $MgAl_2O_4$-Al_2O_3 and Al_2O_3 peaks, that's why it's difficult to see its presence I the other peaks of the pattern. Apart from this, XRD analysis shows complete reduction of crystalline NiO to Ni.

3 - $NiO/CaZrO_3$

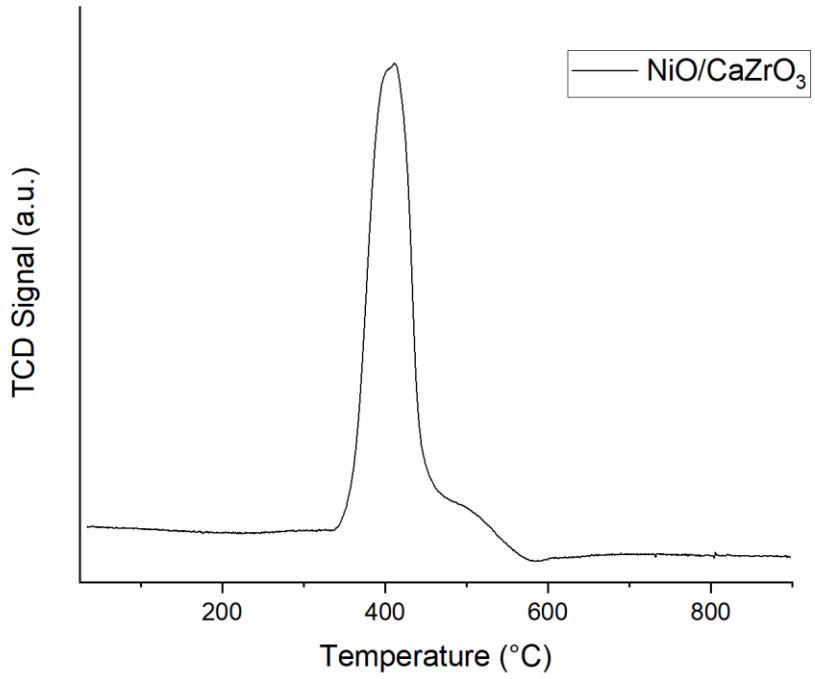

Figure 40- H_2-TPR experiment on $NiO/CaZrO_3$ (until 900°C)

For $NiO/CaZrO_3$ (figure 40), a peak around 400°C was detected, that is NiO weakly interacting with the surface. The shoulder at 500°C is due to more strongly interacting nickel with the perovskite. [57]

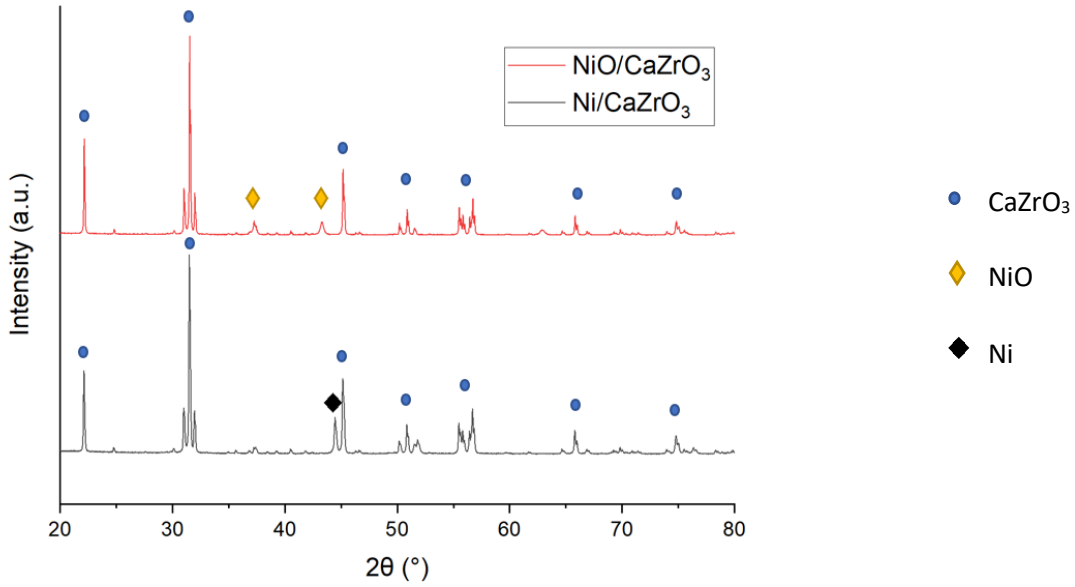

Figure 41 - XRD pattern of $NiO/CaZrO_3$ catalyst post-calcination (red) and post-reduction treatment (black) (until 900°C)

After reduction treatment (figure 41), the XRD pattern indicates that all NiO was converted to metallic Ni. As NiO reduction is completed before 600°C, another H_2-TPR experiment was made heating the sample from room temperature to 600°C with a heating rate of 10°/min. Obtaining the reduced form of the catalyst at lower temperature is beneficial both to avoid sintering of the sample and to lower the energetic cost of the catalyst's preparation. After this milder reduction treatment, XRD was made to verify the complete conversion of NiO to Ni; complete reduction of NiO was confirmed by XRD pattern (see Appendix 6.1.).

4 - $NiO/LaFeO_3$

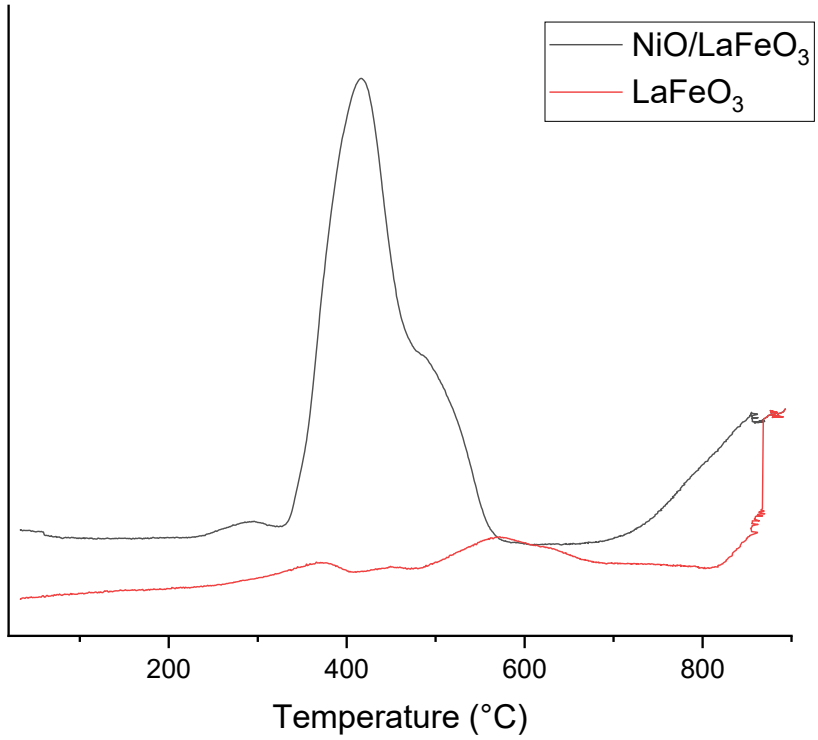

Figure 42- H_2-TPR experiment on $NiO/LaFeO_3$ (black) compared to $LaFeO_3$ (red)

Finally, $NiO/LaFeO_3$ reducibility was studied and is compared with that of the support in figure 42. A broad peak with maximum at 400°C and a shoulder at 500°C was seen, due respectively to NiO weakly interacting and more strongly interacting with the perovskite. Then, from 750°C, perovskite reduction took place. The partial reduction of the perovskite explains the formation of La_2O_3 seen from XRD pattern of the reduced catalyst (figure 43). [58]

It is possible to see a slight shift of perovskite's reduction temperatures between $NiO/LaFeO_3$ and $LaFeO_3$: $LaFeO_3$ shows later reduction temperatures, as can be seen by the starting temperature of the peak at 600°C and 800°C respect to $NiO/LaFeO_3$. Higher reduction temperatures may be attributed to a bigger dimension of the particles. [59]

Finally, XRD measurements were made to evaluate the crystalline phases of the reduced catalyst, and to compare them with the post-impregnation one (figure 43).

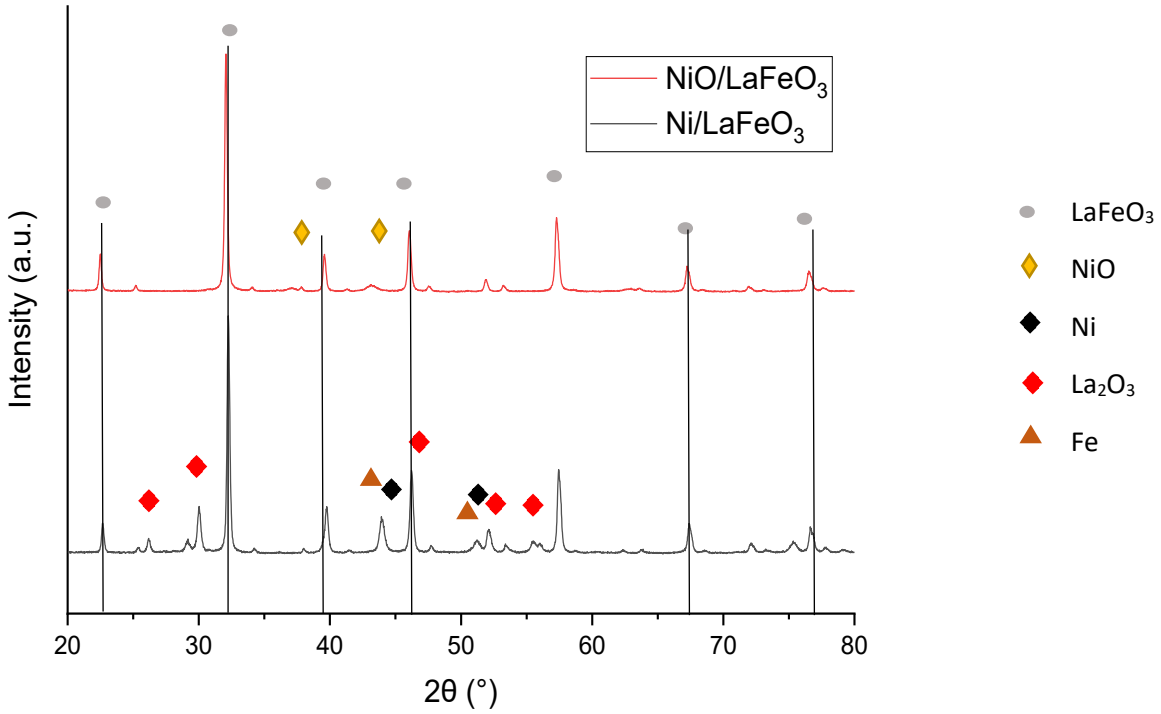

Figure 43- XRD pattern of $NiO/LaFeO_3$ catalyst post-calcination (red) and post-reduction treatment (black) (until 900°C)

Metallic nickel can be seen in the reduced catalyst, while no nickel oxide was detected, confirming total Ni reduction after the treatments. Apart from the perovskite support, La_2O_3 is present in the XRD pattern, accounting for perovskite instability in the reductive atmosphere at high temperatures. When the perovskite is reduced, La_2O_3 and Fe are obtained. However, Fe is more difficult to see, as its reflexes overlap with those of nickel. Therefore, to detect the presence of Fe, a zoom in the XRD pattern of the reduced catalyst is needed, as shown below (figure 44):

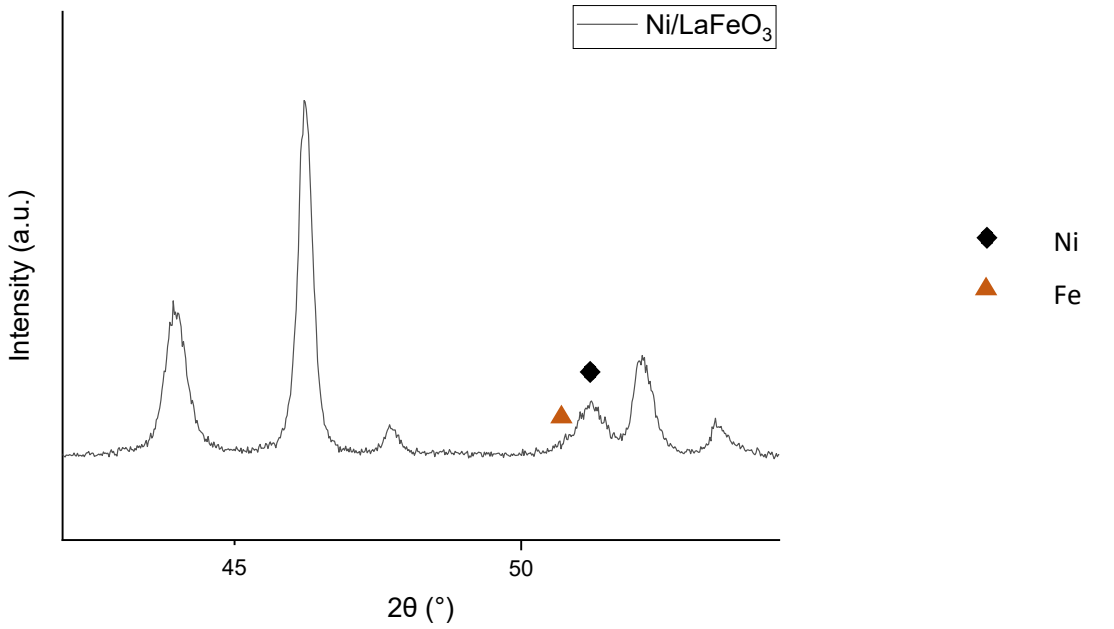

Figure 44 -Zoom of XRD pattern of $Ni/LaFeO_3$ (reduction treatment up to 900°C)

Fe presence can be seen in particular at 2θ=51°, thanks to the shoulder present at the left of nickel's peak.

To evaluate whether nickel oxide is completely reduced after the peak at 600°C, a TPR treatment was carried out reaching a maximum temperature of 600°C. The reduced catalyst was then studied via XRD measurements (figure 45):

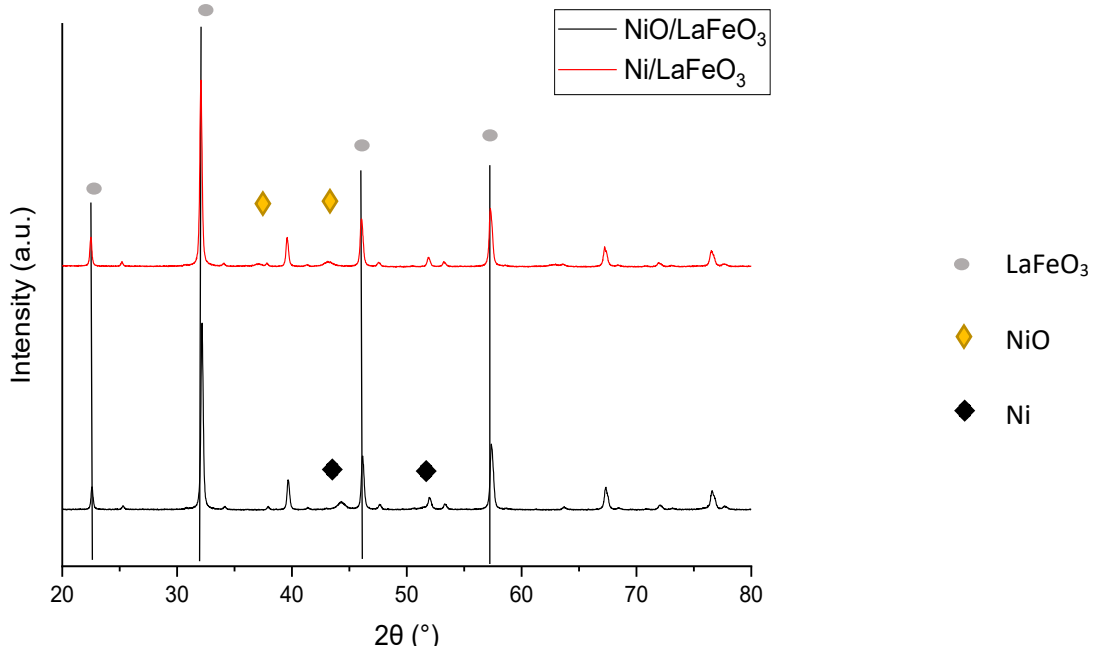

Figure 45- XRD pattern of $NiO/LaFeO_3$ catalyst post-calcination (black) and post-reduction treatment (red) (until 600°C)

XRD pattern of the reduced and post-impregnation catalyst show the complete reduction of NiO with a reductive treatment at 600°C (figure 45). No La_2O_3 was detected by XRD, due to the milder conditions of reduction that allow to keep the perovskite structure intact. However, as seen in H_2-TPR measurements (figure 42), $LaFeO_3$ is slightly reduced under 600°C. Under H_2 flow, Fe cations can exit from the perovskite structure, forming perovskites sub-stoichiometric in iron, with the latter that can either form iron oxides or be reduced to its metallic phase, as reported in literature. [60] Thanks to an analysis of nickel reflexes in $Ni/LaFeO_3$ pattern, metallic Fe can be detected, as seen in figure 46 below:

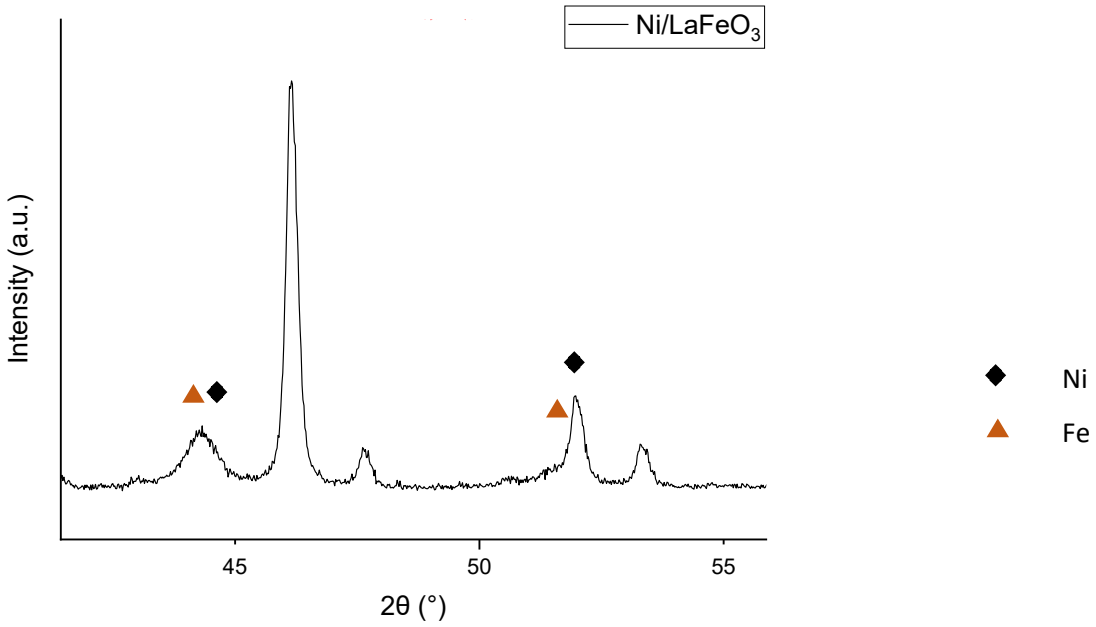

Figure 46-Zoom of XRD pattern of $Ni/LaFeO_3$ (reduction treatment up to 600°C)

Metallic Fe is particularly visible thanks to the asymmetry of the peak at 2θ=52° and to the contribution on the left of Ni's peak at 2θ=44.3°.

In conclusion, complete reduction of crystalline NiO to Ni was observed in all samples.

In order to evaluate whether Ni^{II} was completely reduced in TPR measurements, the quantity of H_2 used in the experiments was used to calculate the amount of Ni^{II} reduced, and compared to the theoretical quantity of nickel deposited onto the catalysts during the synthesis. In order to obtain this information, the following reaction (8) was considered:

$$NiO + H_2 \rightarrow Ni + H_2O \qquad (8)$$

The acquired data are summarized in table 4 below:

Table 4- H_2 quantity (cm^3/g) employed in TPR measurements and evaluation of the experimental quantity of NiO reduced, the theoretical quantity of NiO present in each sample and the percentage of NiO reduced in each sample

Sample	**Quantity H_2** (cm^3/g)	**m_{NiO}/ g**	**$m_{NiO\ calculated}$/g**	**$\%_{NiO\ reduced}$**
NiO/Al_2O_3	39.08	0.13	0.16	79.83
$NiO/MgAl_2O_4$-Al_2O_3	45.41	0.15	0.17	91.39
$NiO/CaZrO_3$	54.76	0.18	0.17	110.34
$NiO/LaFeO_3$	55.72	0.19	0.17	109.33

The table shows that in alumina-based samples NiO was partially reduced, around 80% and 90% for respectively Al_2O_3 and $MgAl_2O_4$-Al_2O_3 support. This might be due to the presence of the spinel $NiAl_2O_4$, which needs high temperatures to be reduced. However, this difference could be also due to Ni strongly interacting with the support, that doesn't necessarily enter in the support's structure to form the spinel. [61], [62] Perovskites samples showed instead over 100% nickel oxide reduction; this might be due to the presence of other reducible species present in the samples. H_2-TPR results suggested that the supports were either stable in reductive atmosphere, as for $CaZrO_3$, or the quantity of H_2 consumed by the perovskite support had already been subtracted for the H_2 consumed by the sample, as for $LaFeO_3$. So, it most probably Ni that consumes all the detected H_2. This might be explained with Ni being present after impregnation in a higher oxidation state than Ni^{2+}. Nickel could be in its Ni^{3+} oxidation state at the interface with perovskites, as has been hypothesized before in literature for nickel at the interface with oxygen rich environments, such as perovskites. [63]

Finally, reduced catalysts were studied to gain information about the average Ni crystallite size, calculated using Scherrer's equation from their XRD pattern; Ni average crystallite size was then compared to NiO crystallite size, evaluated thanks to the post-impregnation XRD patterns of the samples.

For each sample, the average crystallite size was calculated via Scherrer equation (9):

$$L = \frac{K \cdot \lambda}{\beta \cdot cos\theta} \qquad (9)$$

Where L is the crystallite size (nm), K a constant related to the crystallite shape (a value of 0.89 assuming a spherical shape was used), λ the radiation wavelength (0.154 nm for Cu Kα), β the full width at half maximum (FWHM) of the most intense reflection. β was calculated using the reflection at 2θ=43.2° for NiO calculations, and 2θ= 44.3° for Ni. The obtained results are reported in Table 5.

Table 5- NiO and Ni dimension for each sample, evaluated via Scherrer's equation

Support	L_{NiO} (nm)	L_{Ni} (nm)
Al_2O_3	10.7	12.9
$MgAl_2O_4$-Al_2O_3	10.6	16.1
$CaZrO_3$	23.9	37.6
$LaFeO_3$	10.5	19.8

Crystallite size shows bigger crystallites dimension for Ni than NiO, due to the reducing treatment at high temperature that causes the sintering of the particles. Moreover, while NiO crystallite size are almost the same for all catalysts except NiO/$CaZrO_3$, Ni crystallite size shows an increase in crystallite size in perovskite-based samples, that are characterized with a weaker interaction with NiO particles, as seen in H_2-TPR experiments in this chapter.

3.1.5. H_2-Pulsed Chemisorption

Nickel dispersion and nickel particle size was calculated by H_2-Pulsed Chemisorption. The amount of H_2 chemisorbed was evaluated from the area under the experimental curves. A model for spherical particles was used in order to evaluate the dispersion and size of nickel nanoparticles, under the assumption of having spherical nanoparticles and of the nature of the crystal planes exposed on the metal surface and of having 1 hydrogen atom adsorbed by each metallic surface atom. [64] The following equation (10) was used to evaluate nickel dispersion:

$$D(\%) = \frac{1}{\alpha} \cdot \frac{H}{M} \cdot 100 = \frac{M_S}{M} \cdot 100 \qquad (10)$$

Where H is the total amount of chemisorbed hydrogen atoms (experimentally quantified from chemisorption peaks integration), M the total amount of metal atoms (known from the synthesis), α the

number of surface metallic atoms and $\alpha = \frac{H}{M_S}$ the chemisorption stoichiometric factor, i.e. the number of adsorbed hydrogen atoms per surface metallic atom. α is here assumed to be 1, as reported by Bartholomew et al in their H_2 chemisorption studies on Al_2O_3 and SiO_2. [65]

Nickel average particle size was then evaluated via the following equation (11):

$$d\ (nm) = \frac{6 \cdot MW}{D \cdot \rho \cdot \sigma \cdot N_{AV}} \qquad (11)$$

Where 6 is a factor derived from the ratio volume/area of the nanoparticles ($\frac{\pi d^3}{\pi d^2}$), MW is the molecular weight (58.71 for nickel), D is the distribution in %, σ is the atomic cross- sectional area (0.0649 nm² for nickel), ρ is the (8.9 g/cm^3 for nickel) and N_{AV} is the Avogadro number.

Ni Dispersion and its average particle size are reported for each sample below in table 6 below:

Table 6- Nickel Dispersion and Nickel average particle size for all samples

Sample	**Metal Dispersion** (%)	**Active particle size** (nm)
Ni/Al_2O_3	0.31%	327
$Ni/MgAl_2O_4$-Al_2O_3	0.36%	279
$Ni/CaZrO_3$	1.66%	61
$Ni/LaFeO_3$	0.26%	390

Nickel particles are estimated to have dimensions in the range of 200-300 hundred of nanometers for all samples except $Ni/CaZrO_3$. In those samples, nickel has smaller dimension for alumina-based catalysts, due to the strong interaction between the metal and the support. Smaller nickel particles have been found for $Ni/MgAl_2O_4$-Al_2O_3 (279 nm), followed by Ni/Al_2O_3 (327 nm), as suggested in H_2-TPR experiments by the reduction temperatures, that accounted for the strength of the metal-support interaction in the samples (see chapter 3.1.4.). $Ni/LaFeO_3$ shows bigger particle dimension (390 nm), which is due to the low interaction of NiO with the support (see chapter 3.1.4.). However, this trend is not followed by $NiO/CaZrO_3$, which has the smallest particle dimension, despite being the support with the weaker interaction with NiO particles (see H_2-TPR results). The latter result could not be rationalize comparing it with the results obtained by the other experiments, not being in accordance with H_2-TPR, XRD and XPS data acquired to characterize nickel species in the samples. This might be due to the model employed to obtain the dispersion and particle size dimension,

that was used under different assumptions such as of having spherical particles, having 1 hydrogen atom adsorbed by each nickel atom and of having only hydrogen chemisorption due to the nickel present in the samples. [64]

3.1.6 XPS

XPS was employed at first for semi-quantitative surface compositions analysis of the reduced catalysts: Ni/Al_2O_3, $Ni/MgAl_2O_4$-Al_2O_3, $Ni/CaZrO_3$, $Ni/LaFeO_3$. This analysis allows to investigate the composition of the first 5-10 nm in depth of the catalysts; XPS compositions can be compared to the nominal values and to EDX results, that account for an almost "bulk" compositions- i.e. EDX is able to investigate around 1 µm depth. A graphical visualization of this comparison is given by figures 47–50 below.

XPS analysis was performed by integrating main elements' photopeaks and using the sensitivity factor implemented in the XPS software-which accounts for the ionization cross-section, i.e. the probability, that depends on a series of parameters such as the specific orbital. Prior to that, a Shirley type background was made. Obtained atomic compositions are shown in the table below:

Table 7-XPS (5-10 nm depth) and EDX (≈ 1 µm depth) elemental quantifications for each metal, calculated without considering the oxygen content are here reported together with the nominal values, based on sample stoichiometry. Note: for EDX, the analyzed areas are squares of 400-500 µm side.

		Atomic Composition (at. %)						
Sample	***Analysis***	***Ni***	***Al***	***Mg***	***Ca***	***Zr***	***La***	***Fe***
	Nominal	16.9	83.1					
Ni/Al_2O_3	EDX	16.1	83.9					
	XPS	6.3	93.7					
	Nominal	11.1	73.5	15. 4				
$Ni/MgAl_2O_4$-Al_2O_3	EDX	21.7	68.5	9.8				
	XPS	7.0	83.9	9.1				
	Nominal	15.8			42.1	42.1		
$Ni/CaZrO_3$	EDX	23.8			37.6	38.6		
	XPS	42.2			39.5	18.2		
	Nominal	20.8					39.6	39.6
$Ni/LaFeO_3$	EDX	25.1					38.9	36.0
	XPS	52.9					27.4	19.7

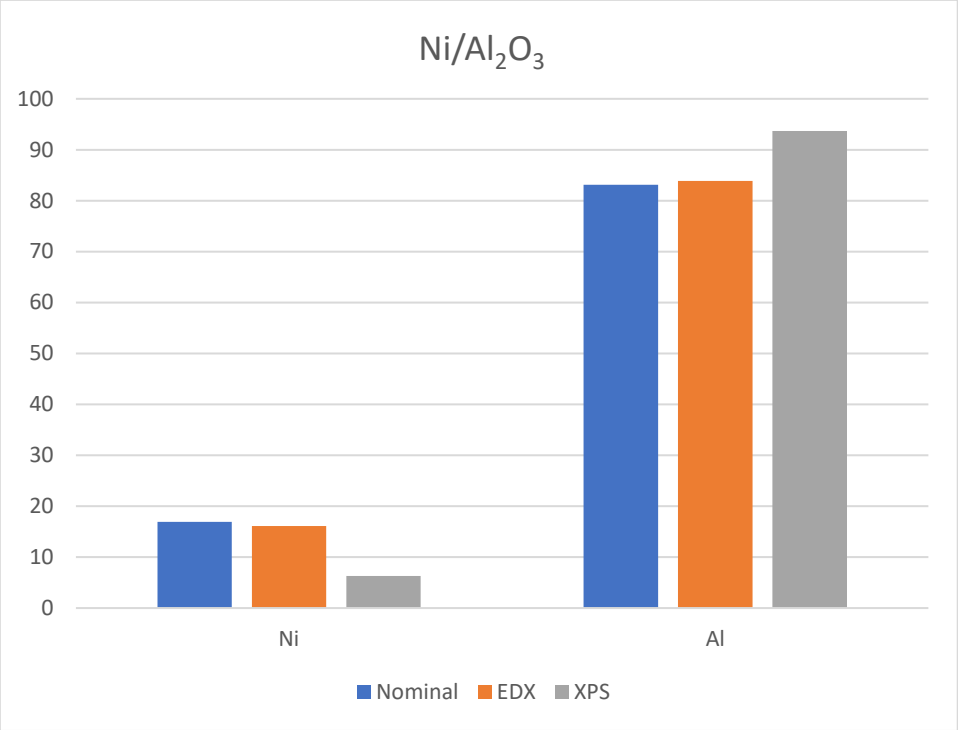

Figure 47- Comparison between XPS, EDX and nominal compositions in atomic percentage for each metal for Ni/Al_2O_3 sample

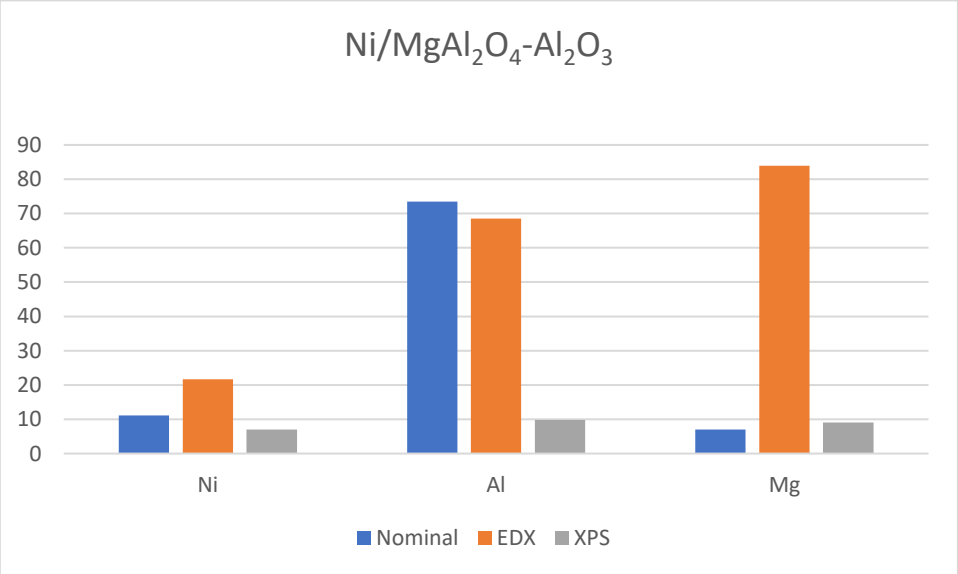

Figure 48- Comparison between XPS, EDX and nominal compositions in atomic percentage for each metal for $Ni/MgAl_2O_4$-Al_2O_3 sample

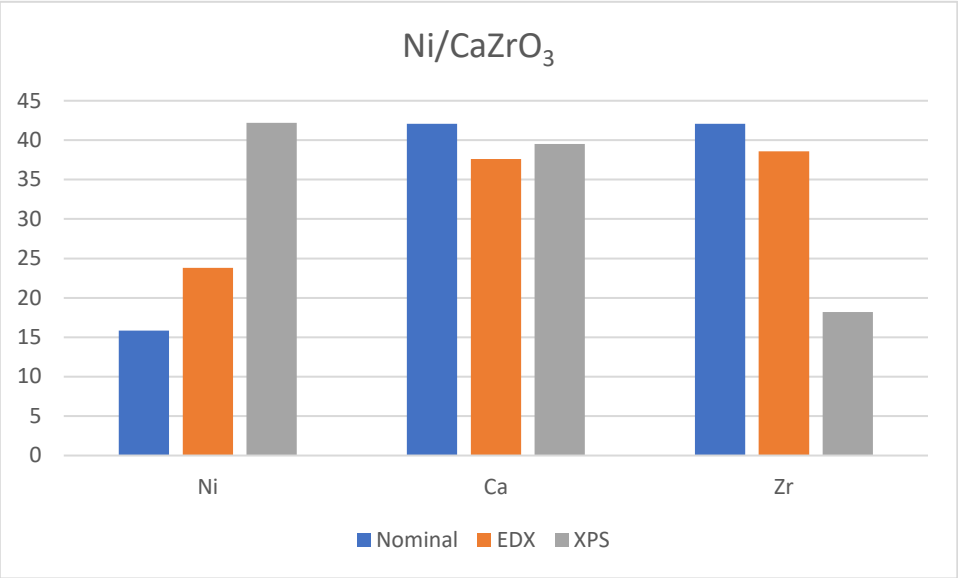

Figure 49- Comparison between XPS, EDX and nominal compositions in atomic percentage for each metal for $Ni/CaZrO_3$ sample

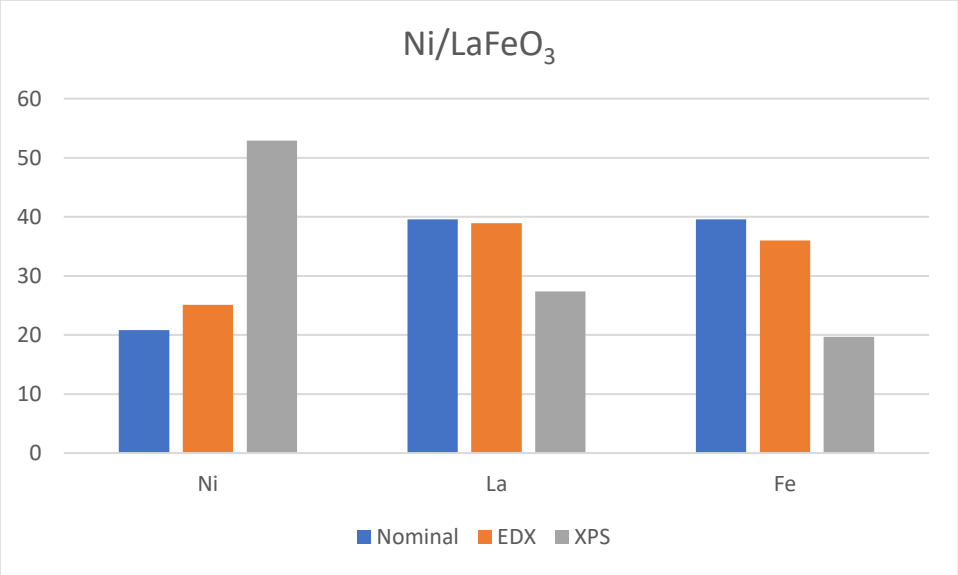

Figure 50- Comparison between XPS, EDX and nominal compositions in atomic percentage for each metal for $Ni/LaFeO_3$ sample

The results above allow several considerations about the catalysts. First of all, it shows that nickel distribution in the surface and bulk of the catalysts is different in alumina-based catalysts and in perovskites catalysts. Perovskites catalysts show that nickel is more present at the surface than in the bulk, as nickel atomic composition is double in XPS results compared to EDX data. Nominal compositions are lower than EDX compositions (as EDX - with its 1µm analysis depth - accounts for compositions that are mediated between bulk compositions and surface compositions); these results support the hypothesis that Ni is prevalent on

surface as is expected because the synthesis chosen is an impregnation method, which deposits nickel onto the surface of the supports. However, this changes with alumina-based catalysts, where Ni XPS derived compositions are less than half of Ni EDX compositions. This presence of nickel in deeper levels of the catalysts can be explained with the diffusion of nickel atoms into the structure of the support, to give nickel-based spinel $NiAl_2O_4$, that is in agreement with XRD and XPS analysis (see below).

In both perovskites catalysts, XPS results show a difference in A and B cations concentrations: in $Ni/CaZrO_3$, Zr is present in lower concentrations then Ca ($Ca_{\%} > 2\ Zr_{\%}$), while in $Ni/LaFeO_3$, La XPS concentration was around 2/3 of Fe concentration. EDX atomic compositions show, on the other hand, a good accordance between the two cations compositions, as expected by the nominal values. This might be explained with a surface migration of the ions Ca and La respectively, that most probably form oxygen-rich species such as oxides, hydroxides or carbonates species.

XPS detailed spectra of the main regions have been acquired to improve information about the oxidation state of the elements distributed on the surface of the samples.

At first, XPS detailed spectra of Ni2p was acquired for all reduced catalysts, to investigate the surface species present in the catalysts.

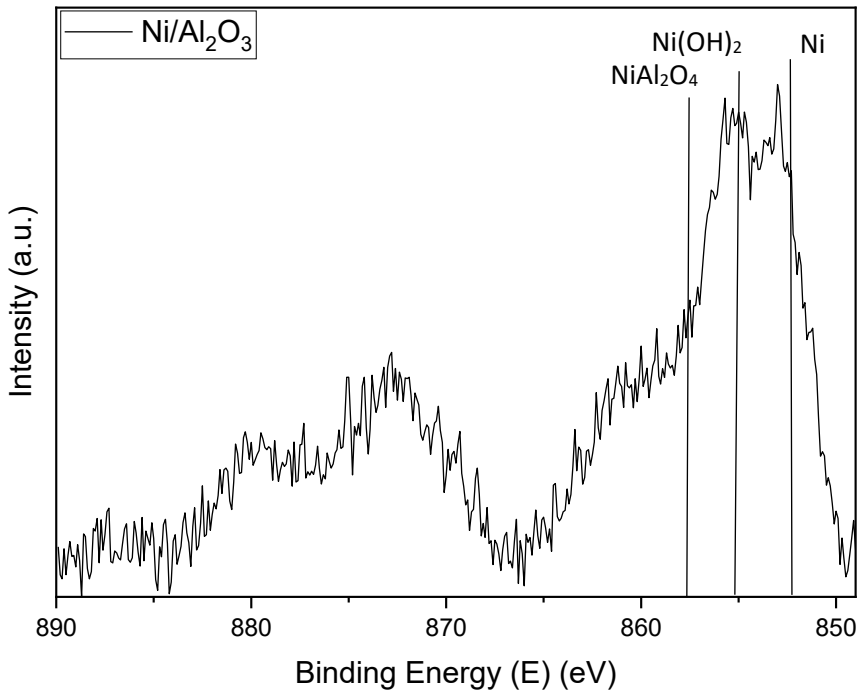

Figure 51- Detailed XPS spectra of Ni 2p photopeak for Ni/Al_2O_3 sample

From Ni 2p photopeak it is possible to see the presence of two contributions: metallic nickel at 852.9 eV, as expected, and a Ni^{II} specie contribution at 855.3 eV. The latter specie was attributed as nickel hydroxide for

both its binding energy position and peak shape (see figure 52), as expected for impregnated nickel nanoparticles after reduction. [66] The presence of this specie is probably due to metallic nickel that is oxidized back when put in contact with the air. This explains why $Ni(OH)_2$ is visible in the XPS spectra and not by XRD measurements, as only the most superficial layers of metallic Ni are oxidized back. However, this phenomenon won't concern the catalytic activity of the samples, as catalysts will be reduced and then directly tested for catalytic activity using the same apparatus, in order to avoid the oxygen-containing atmosphere of the air.

Moreover, it is possible to gain additional information about nickel species by comparing Ni photopeak with reference Ni and $Ni(OH)_2$ photopeaks, showed in figures 52 and 53 below:

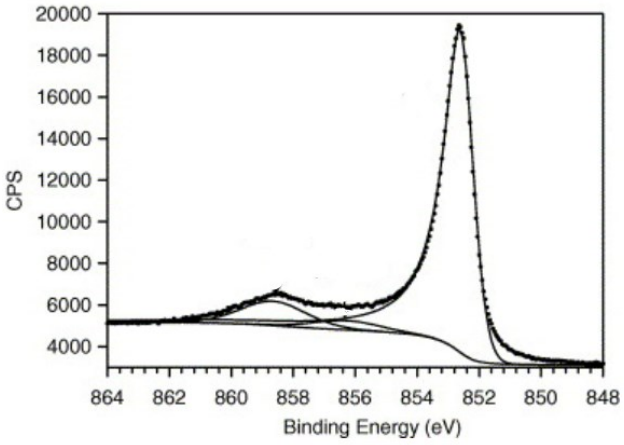

Figure 52- Detailed reference XPS spectra of Ni 2p photopeaks for $Ni(OH)_2$ [67]

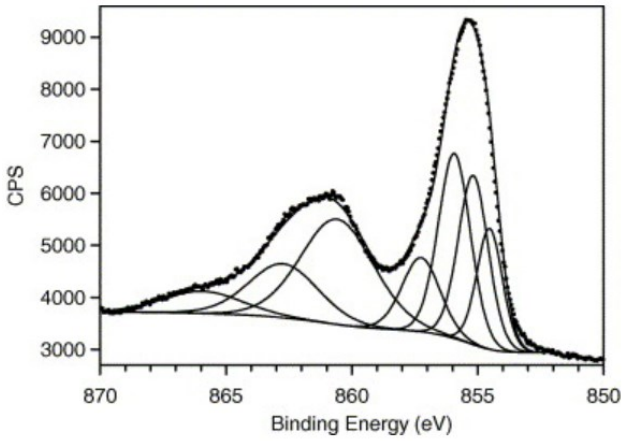

Figure 53- Detailed reference XPS spectra of Ni 2p photopeaks for Ni^0 [67]

By comparing Ni photopeak with the reference peaks (figure 52-53), it is evident that an added contribution around 858.1 eV is present in the spectra. This contribution can be centered at around 858.1 eV, and it accounts for the presence of a Ni^{II} specie besides $Ni(OH)_2$, that is in agreement with how expected for this element in $NiAl_2O_4$ spinel. To verify this hypothesis, Al 2p photopeaks were acquired (see after), and revealed the spinel's presence. This contribution can be attributed to $NiAl_2O_4$ spinel, thanks to comparison with literature and in agreement with what suggested by TPR results. [68]

$Ni/MgAl_2O_4$-Al_2O_3 was analyzed as well with a Ni 2p scan to study the nickel species present in the surface of the reduced catalyst (figure 54):

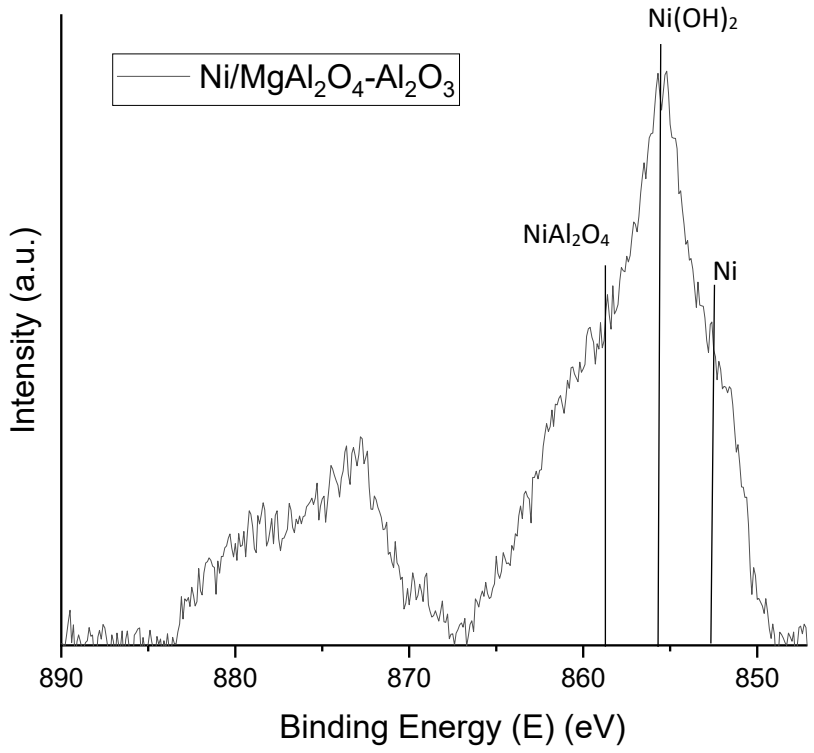

Figure 54- Detailed XPS spectra of Ni 2p photopeak for $Ni/MgAl_2O_4$-Al_2O_3 sample

The reduced sample showed the presence of Ni^0 and Ni^{II} species at respectively 852.8 eV and 855.7 eV. Ni^{II} specie has been attributed as before to $Ni(OH)_2$, present after reduction treatment because of the re-oxidation of the nickel particles when the sample is air exposed. By comparing Ni 2p photopeak with reference Ni^0 and $Ni(OH)_2$ photopeaks (figures 52-53), it appears that an additional Ni^{II} contribution is present in the sample, as for the sample before. This contribution at around 858.1 eV can be attributed to the spinel, as expected from literature and TPR results.

Ni in perovskites samples was studied as well, and Ni 2p and Ni 3p scans were obtained and analyzed. Ni was analyzed in $Ni/CaZrO_3$ sample via a Ni 2p scan, while $NiO/LaFeO_3$ was analyzed with Ni 3p detailed spectra due to the interferences of La 3d in Ni 2p region. $Ni/CaZrO_3$ Ni 2p scan is reported in figure 55 below:

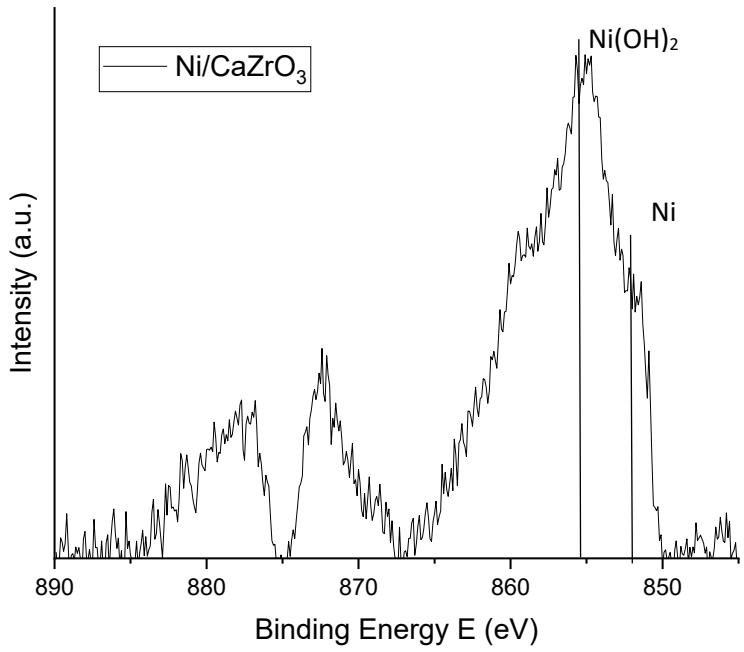

Figure 55 - Detailed XPS spectra of Ni 2p photopeak for $Ni/CaZrO_3$ sample

$Ni/CaZrO_3$ showed the presence of both metallic Ni (852.6 eV) and $Ni(OH)_2$ (855.3 eV). As for the other samples, while Ni is expected after the reductive treatment in 5% H_2/Ar, $Ni(OH)_2$ detected by XPS analysis is due to partial re-oxidation of Ni particles due to air exposure after the treatment. However, re-oxidation is expected to affect only the most superficial layers of nickel particles, as being the layers in contact with air; no crystalline bulk $Ni(OH)_2$ was detected by XRD results (see chapter 3.1.4.).

Finally, Ni 3p scan was obtained for $Ni/LaFeO_3$ catalyst (figure 56):

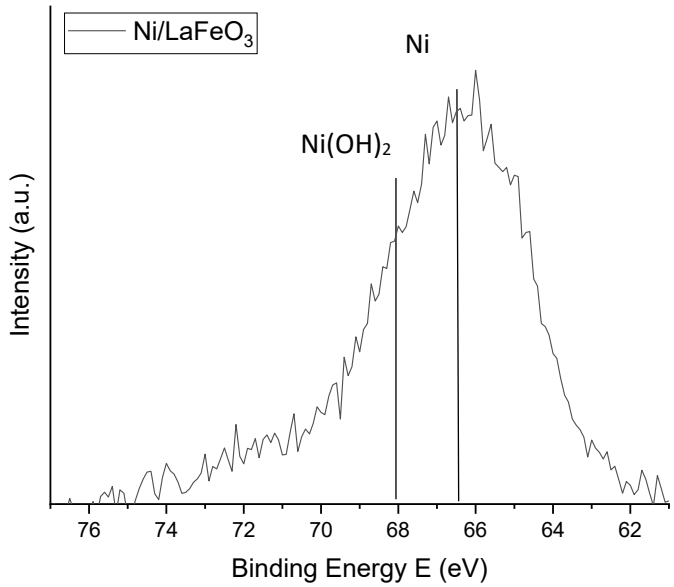

Figure 56 - Detailed XPS spectra of Ni 3p photopeak for $Ni/LaFeO_3$ sample

Ni peak was detected in the scan, as well as a contribution at around 68 eV, that was attributed to $Ni(OH)_2$ as for the samples above.

In conclusion, all reduced samples showed Ni presence in their surface, and a $Ni(OH)_2$ contribution that is due to air exposure after the reductive treatment. However, re-oxidation of the catalyst is supposed to affect only the outer layers of nickel particles, as suggested by the absence of $Ni(OH)_2$ in XRD patterns of the reduced catalysts in chapter 3.1.4.. Moreover, catalysts will be reduced and then directly tested for catalytic activity, therefore avoiding air exposure that could compromise their activity.

Also the other spectral regions of the have been acquired to obtain information about the surface species present in the samples.

Detailed Al 2p, Mg 1s, Ca 2p, Zr 3d, La 3d and Fe 2p scans have been obtained for the respective reduced catalysts, and are shown below in figures 57-63:

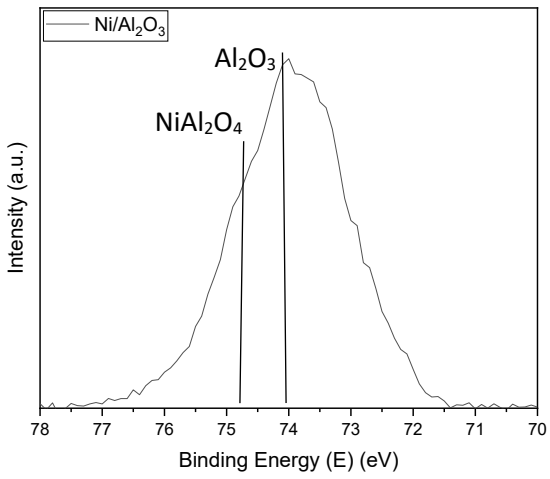

Figure 57 - Detailed XPS spectra of Al 2p photopeak for Ni/Al_2O_3 sample

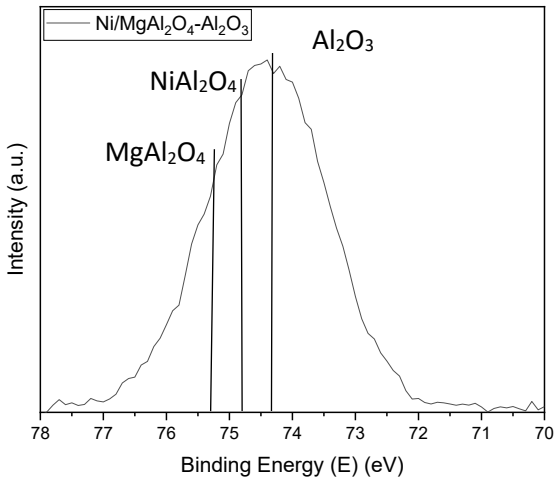

Figure 58- Detailed XPS spectra of Al 2p photopeak for $Ni/MgAl_2O_4$-Al_2O_3 sample

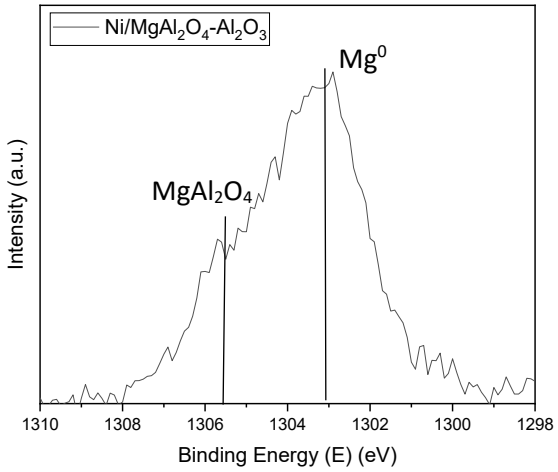

Figure 59- Detailed XPS spectra of Mg 1s photopeak for Ni/$MgAl_2O_4$-Al_2O_3 sample

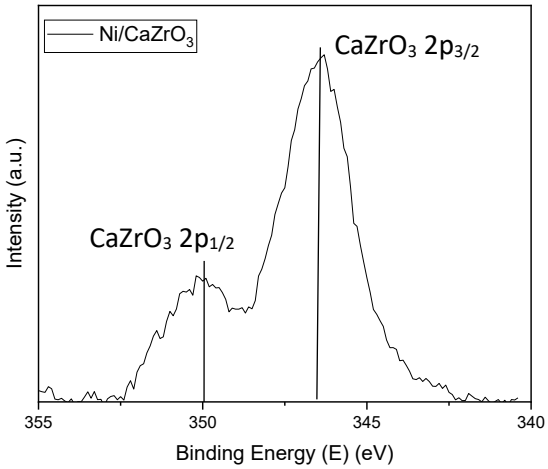

Figure 60- Detailed XPS spectra of Ca 2p photopeak for Ni/$CaZrO_3$ sample

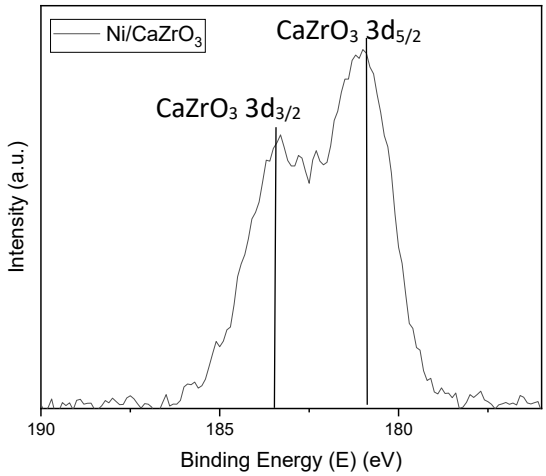

Figure 61- Detailed XPS spectra of Zr 3d photopeak for Ni/$CaZrO_3$ sample

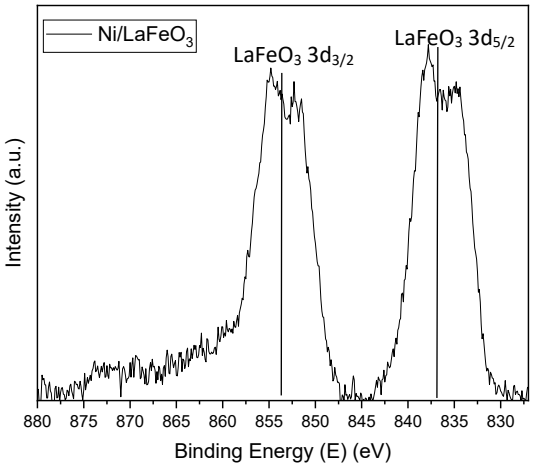

Figure 62 - Detailed XPS spectra of La 3d photopeak for Ni/$LaFeO_3$ sample

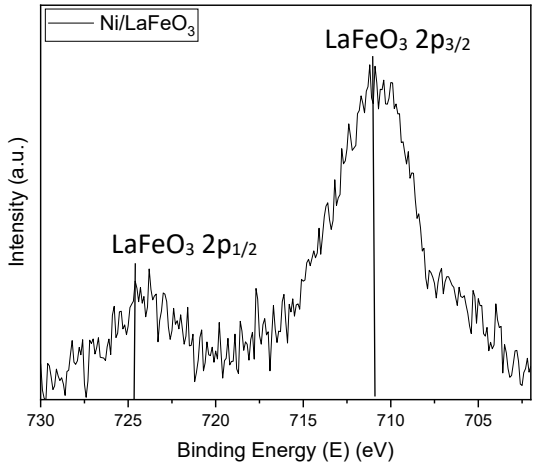

Figure 63- Detailed XPS spectra of Fe 2p photopeak for Ni/$LaFeO_3$ sample

The detailed spectra acquired above have showed the expected photopeaks characteristic for the elements of the supports in their typical oxidation states. Al 2p scan shows in Ni/Al_2O_3 sample a clear contribution to Al_2O_3 peak (74.1 eV) of $NiAl_2O_4$ spinel in the shoulder at 74.7 eV. In $Ni/MgAl_2O_4$-Al_2O_3 catalyst, Al peak broadens due to $MgAl_2O_4$ spinel contribution at the left of $NiAl_2O_4$ spinel (around 75.4 eV), as shown in literature. [69] A part from the confirmation of the expected oxidation states for the atoms of the support, Mg 1s scan has showed the presence of a peak at 1303 eV which is attributed to Mg^0; this is due to the exchange of Mg^{2+} ions of the spinel phase by Ni^{2+}, as previously seen in literature for catalysts with high nickel loadings. [70] For perovskite catalysts, the expected oxidations states of the metal cations in the perovskite phases were observe(Ca^{2+}, Zr^{4+}, La^{3+}, Fe^{3+}), as well as a contribution of Fe^0 to Fe^{2+} peak visible at 707 eV, in accordance with post-reduction XRD results. [57], [71]

4. CATALYTIC ACTIVITY

4.1. Dry Reforming of Methane and Nitric Oxide Reduction: First tests (5% CH_4, 5% CO_2, 1% NO)

Dry Reforming of Methane and Nitric Oxide Reduction catalytic tests were made over all samples. Catalytic activity was tested after a pre-reductive treatment in 5% H_2/Ar flow in temperature ramp (10°C/min, from room temperature to 900°C for alumina-based catalysts and to 600°C for perovskites-based catalysts, as suggested by H_2 -TPR experiments in chapter 3.1.5.) After this step, temperature was decreased until 300-100°C and then gas flow was changed with a gas mixture of 5% CH_4, 5% CO_2, 1% NO and Ar, and temperature risen until 750°C. Catalytic activity was measured thanks to conversion percentages of reactants and yields obtained from percentages of the gas detected after the reactor. Moreover, XRD and XPS data of the spent catalysts were collected to evaluate how the catalysts changed during the catalytic process.

1 - NiO/Al_2O_3

The first catalyst tested was NiO/Al_2O_3 the temperature was increased from 300°C at a heating rate of 10°C/min and then kept constant at 750°C. Conversions and yield data are reported in the graphs below (figures 64 and 65, respectively):

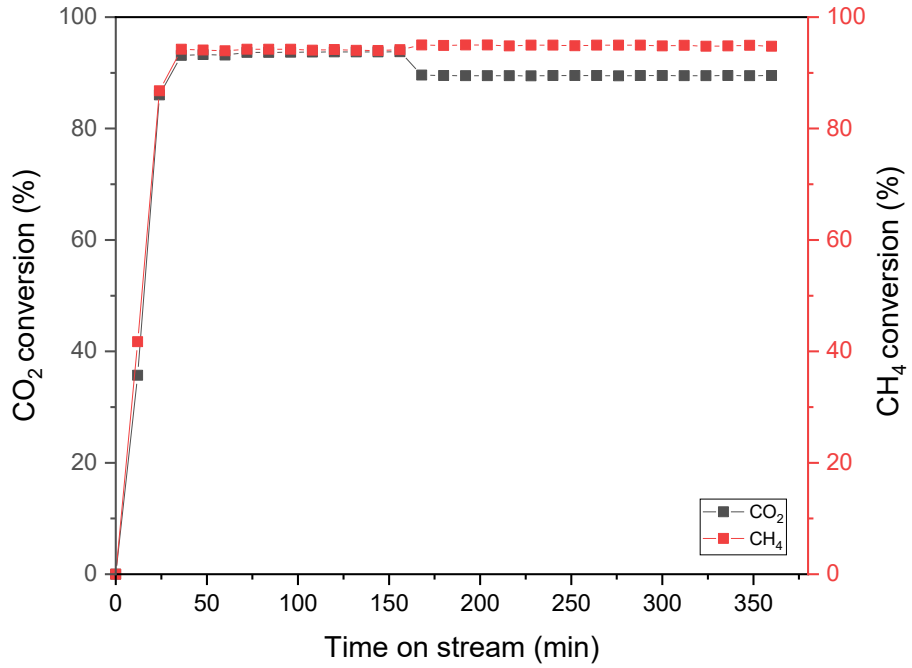

Figure 64- CH_4 and CO_2 conversions vs time measured for NiO/Al_2O_3 at 750°C under gas stream of 5% CH_4, 5% CO_2, 1% NO for 360 minutes

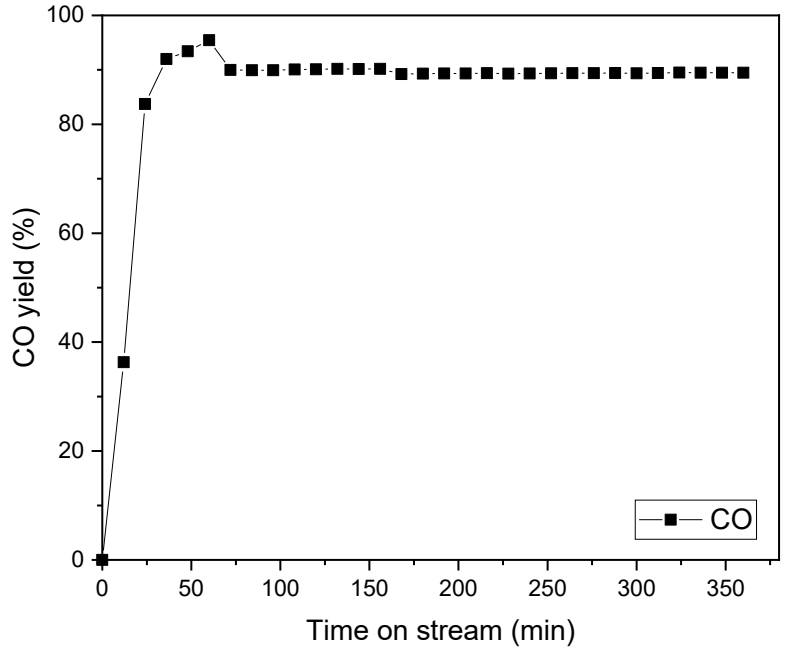

Figure 65- CO yield vs time measured for NiO/Al_2O_3 at 750°C under gas stream of 5% CH_4, 5% CO_2, 1% NO for 360 minutes

The catalyst shows high conversion rates for both CO_2 and CH_4. CH_4 shows comparable conversion to CO_2 in the first 160 minutes, with CH_4 conversion slightly higher than CO_2 one. This might be due also to NO that can react with CH_4 of the reaction mixture. As a matter of fact, NO was not detected by TCD detector, therefore suggesting total NO conversion due to reaction with the gas mixture, prior to coking formation. To verify this hypothesis, NO concentration in the gas mixture was changed from 1% to 1.5% after 160 minutes; subsequently CH_4 conversion increased of around 1% and CO_2 conversion diminished of around 4,5%. NO takes part in reactions (12) and (13) below:

$$2\,NO + 2\,CO \longrightarrow 2\,N_2 + 2\,CO_2 \qquad (12)$$

$$2\,NO + 2\,Ni \longrightarrow N_2 + 2\,NiO \qquad (13)$$

NO reduction with CO can be confirmed by CO's yield that decreases when NO concentration is increased, as shown in figure 65. The change in CO concentration has an impact on DRM reaction (1) and reverse water-gas shift reaction (2), resulting in a change in methane and carbon dioxide conversions.

XRD pattern of the spent catalyst was acquired and is shown in the pattern below (figure 66), together with the post-impregnation and post-reaction catalyst for comparison (figure 67):

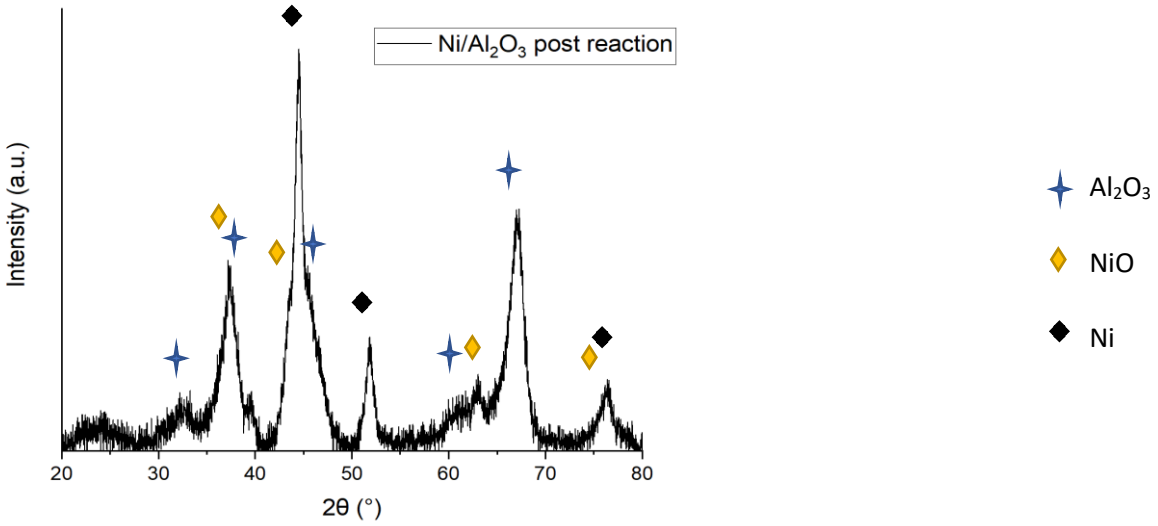

Figure 66 - XRD pattern of post-reaction NiO/Al_2O_3 catalyst

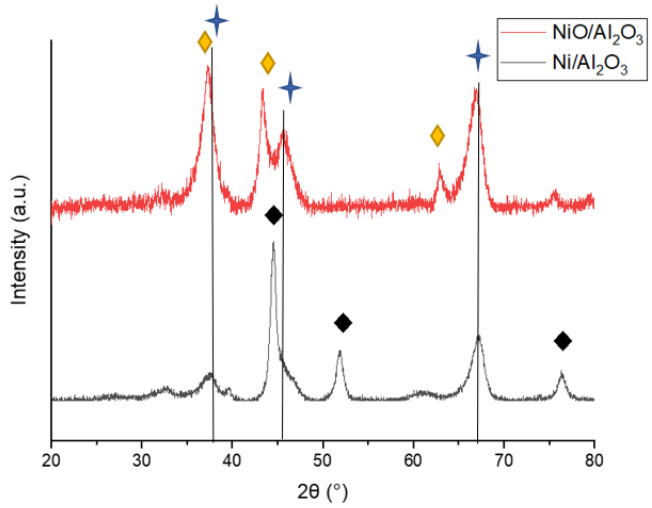

Figure 67 - XRD pattern of NiO/Al_2O_3 catalyst post-calcination (red) and post-reduction (black)

From the XRD patterns it is possible to see that the catalyst during the reaction is partially oxidized. By comparing the post-reaction XRD pattern in figure 66 and the post-reduction catalyst Ni/Al_2O_3 in figure 67, it is evident that a part of Ni is oxidized back to its oxide form NiO after the reaction. The oxidation of Ni can be explained by NO's oxidative power, as seen in chapter 1.2.. No crystalline coke was detected after the process, so dry reforming of methane reaction was tested for the same time on the same catalyst to understand if coke was formed and removed by NO or if the conditions of the process didn't allow coke deposition.

Conversions and yield are reported in the graphs below (figures 68 and 69, respectively):

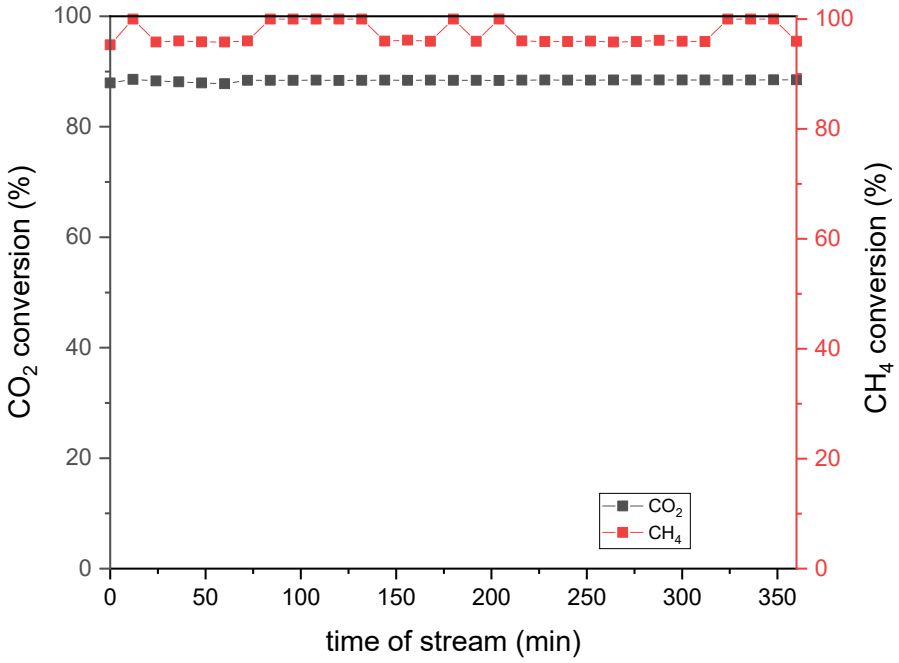

Figure 68- CH_4 and CO_2 conversions vs time measured for NiO/Al_2O_3 at 750°C under gas stream of 5% CH_4, 5% CO_2 for 360 minutes

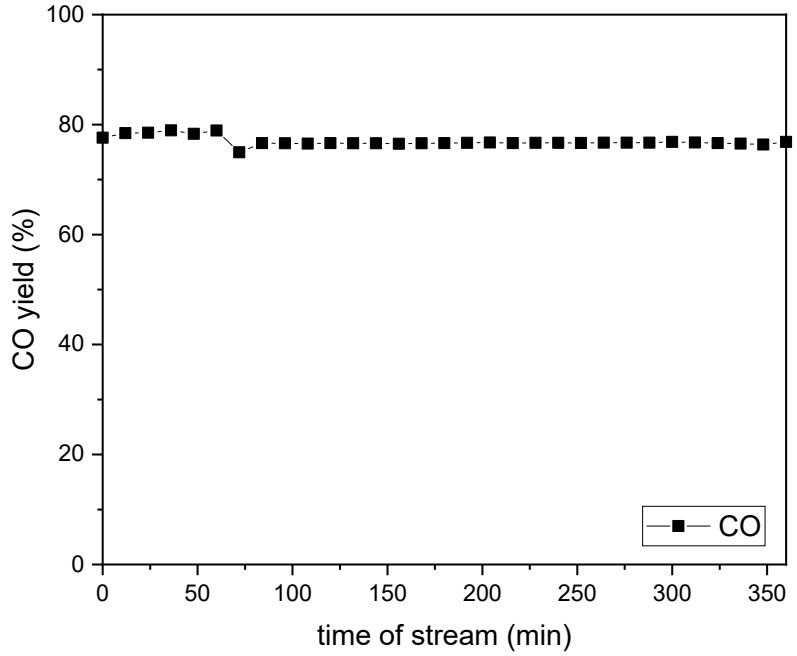

Figure 69- CO yield vs time measured for NiO/Al_2O_3 at 750°C under gas stream of 5% CH_4, 5% CO_2 for 360 minutes

DRM showed comparable activity to DRM and nitric oxide reduction process. CH_4 conversion was slightly higher; this might be due to more metallic Ni that avoids oxidation due to NO presence, so Ni is more present in its active form, which is key for CH_4 conversion. CO_2 conversion values are equivalent in the two processes,

while DRM has a slightly lower CO yield, that can be influenced by the reverse gas-shift reaction and will have an impact on the total H_2/CO ratio.

The spent catalyst was analyzed via XRD pattern to investigate the presence of deposited carbon. XRD pattern of the spent post dry reforming reaction NiO/Al_2O_3 is shown below:

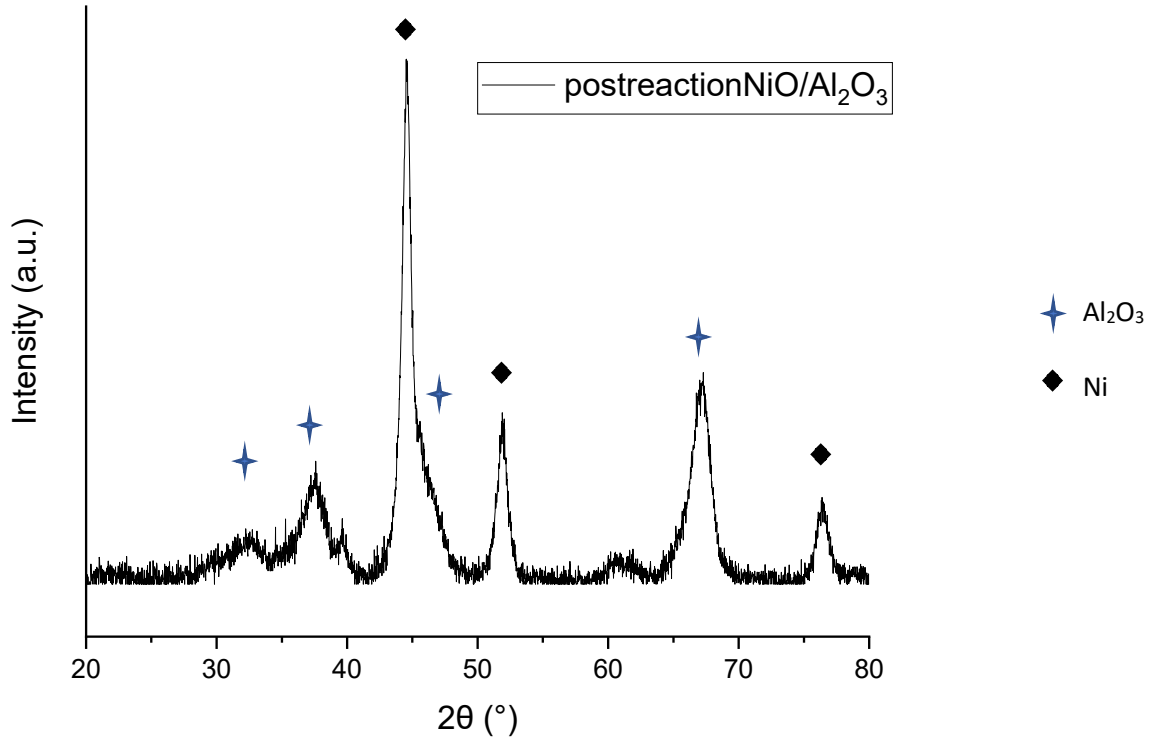

Figure 70 - XRD pattern of post-reaction NiO/Al_2O_3 catalyst

After DRM, the catalyst showed Al_2O_3 and Ni typical peaks, as shown in the figure above. NiO was not detected after the process, therefore confirming that nickel oxidation occurred in the previous test due to NO oxidizing ability (see figures 66-67). In order to understand if NO oxidation of the catalyst can be influenced by the temperature at which the reaction mixture is injected, further experiments will be carried out to understand how to preserve the catalyst in its active phase. No carbon was detected as well by XRD pattern, so in conclusion the conditions (time, temperature, and reactant concentrations) were not enough for coking. Consequently, the next experiments will be conducted for a larger period of time (15h), keeping temperature and the reactant gasses the same as before. Moreover, the temperature of injection of the reaction mixture was changed as well, being lowered from 250° C to 100° C.

NiO/Al_2O_3 tested for 15 hours for dry reforming of methane coupling with nitric oxide reduction gave the conversions and yield data reported in the graphs below (figures 71 and 72, respectively):

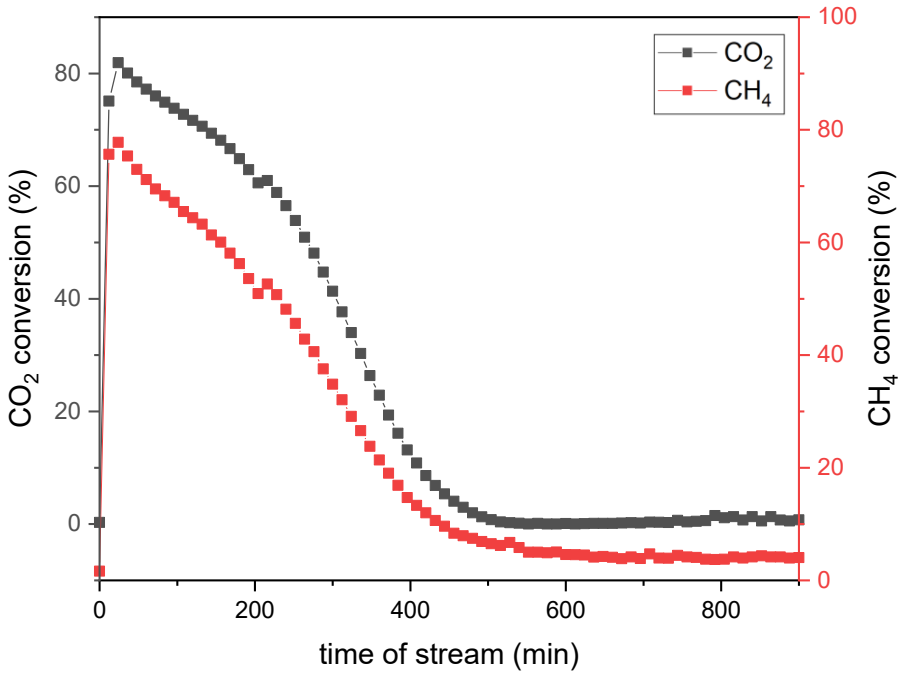

Figure 71- CH_4 and CO_2 conversions vs time measured for NiO/Al_2O_3 at 750°C under gas stream of 5% CH_4, 5% CO_2, 1% NO for 900 minutes

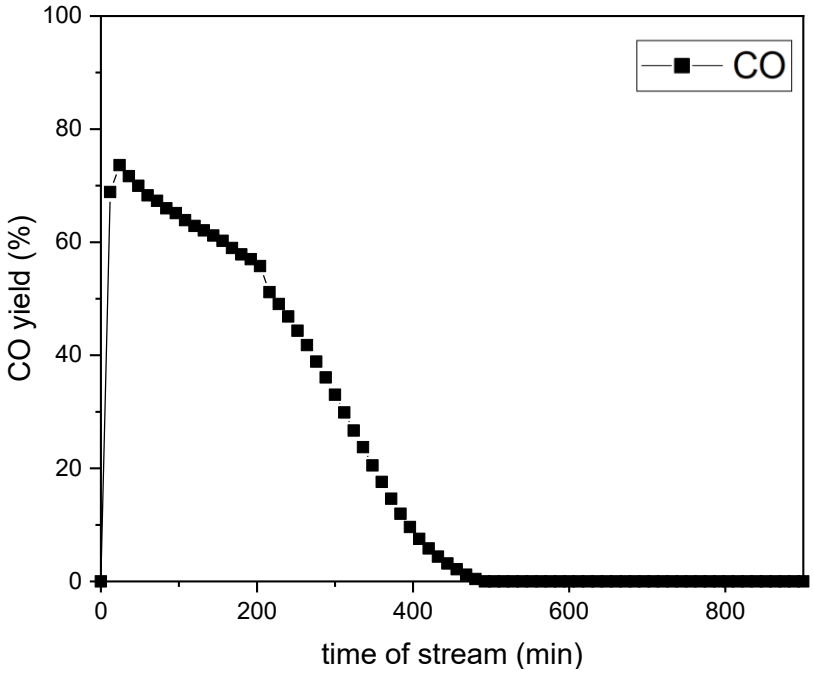

Figure 72- CO yield vs time measured for NiO/Al_2O_3 at 750°C under gas stream of 5% CH_4, 5% CO_2, 1% NO for 900 minutes

The graphs above show high catalytic activity in the first 400 minutes of reaction, time in which CO_2 and CH_4 conversions of CO_2 and CH_4 go to approximately 0%, as CO yield. The rapid decrease of their value is in this amount of time is in strong discordance with what obtained in the first experiment tested, that had the same conditions but for the time of stream (360 minutes). A scan be seen, in the first 6 hours of reaction the behavior of Ni/Al_2O_3 is very different in graphs 71-72 and graphs 64-65. The difference among the two processes was the temperature at which the gas stream was injected into the reactor. While in the first

experiments the gas mixture was injected at 250°C (after the pre-reduction treatment), in this experiment the mixture was injected at 100°C. As NO has a strong oxidative power that can oxidize nickel particles into their inactive form NiO, the difference of the graphs in the two experiments could be due to a deactivation of the catalyst due to nickel oxidation, that is most severe when NO is injected at lower temperatures (100°C). This can be confirmed by the XRD pattern of the spent catalyst, which is shown in figure 73. Having observed the relevance of the injection temperature on the results, further studies have been carried out to evaluate the more adequate conditions for catalytic activity investigation.

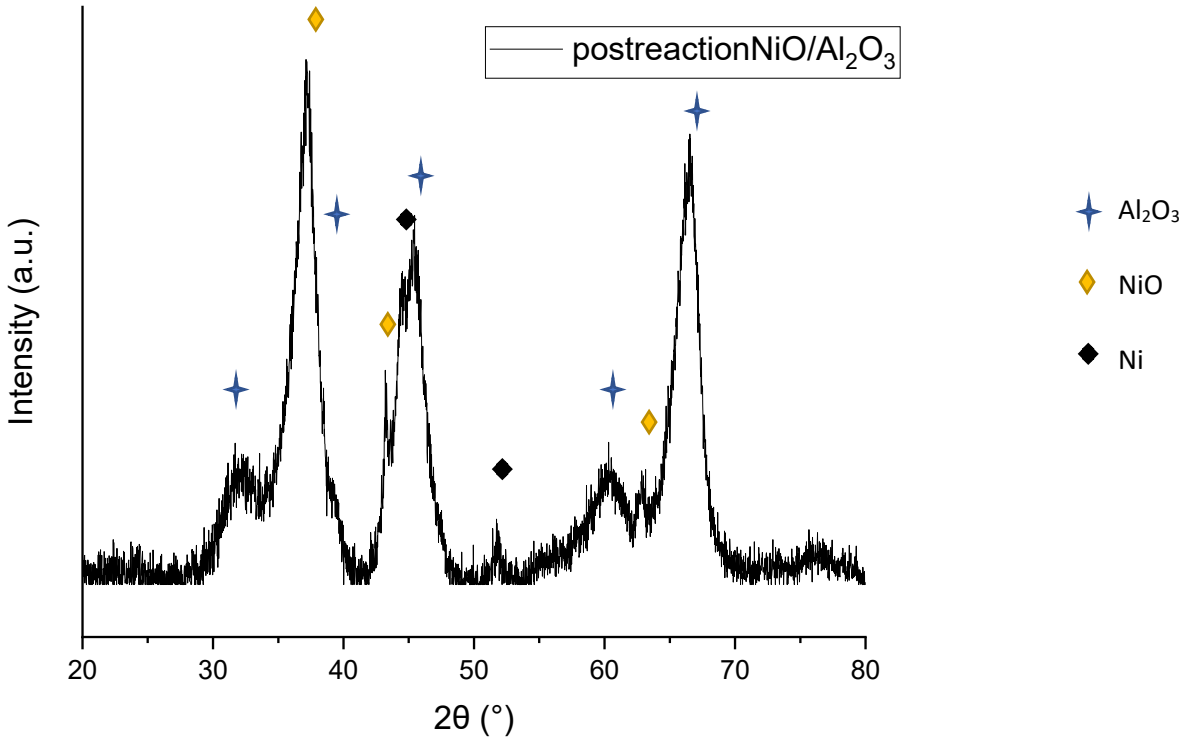

Figure 73 - XRD pattern of post-reaction NiO/Al_2O_3 catalyst

As expected, the XRD pattern shows almost no metallic nickel left, as it was converted to NiO. Al_2O_3 support wasn't modified, instead. In order to gain more information about the difference in the experiment, XRD pattern comparing Al_2O_3, the post-calcination catalyst NiO/Al_2O_3, the post-reduction catalyst Ni/Al_2O_3, DRM spent catalysts and the catalyst spent after DRM and NO reduction process for 15 hours were compared and plotted in the graph below (figure 74):

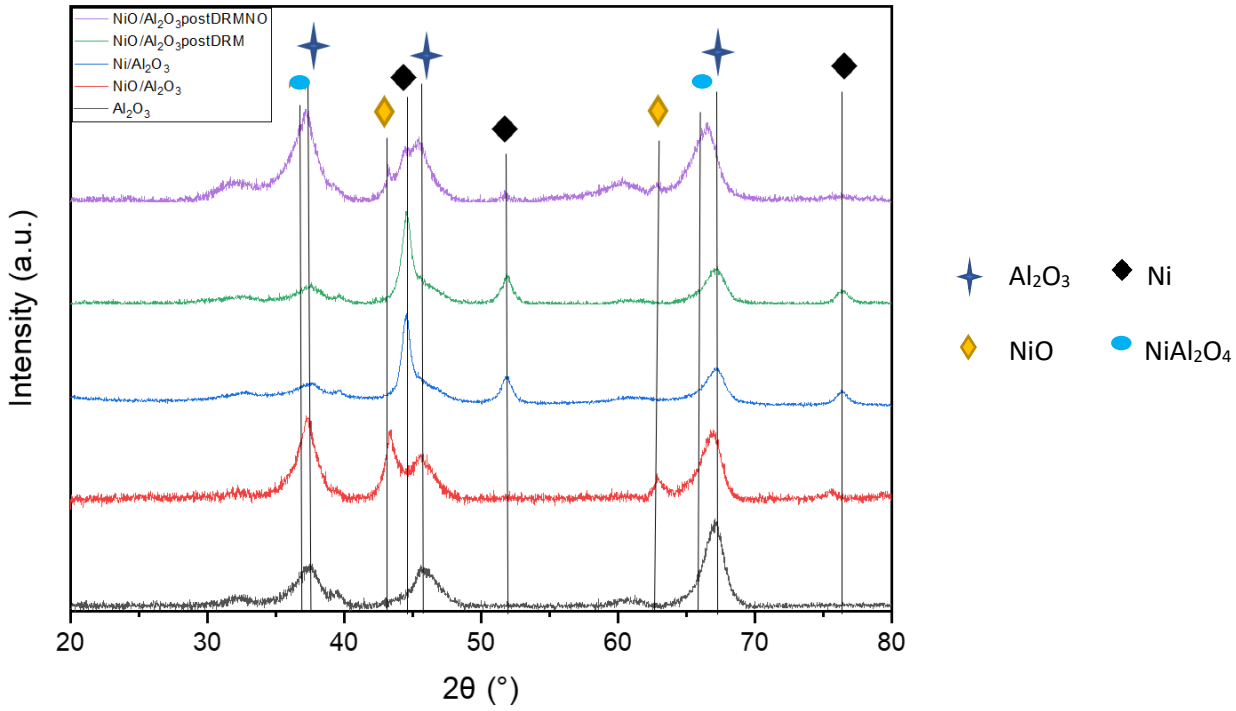

Figure 74 - XRD pattern of normalized post-reaction Al_2O_3, NiO/Al_2O_3, Ni/Al_2O_3, post-DRM reaction NiO/Al_2O_3 and post-DRM and NO reduction (DRMNO) reaction NiO/Al_2O_3 catalysts

In the graph above, nickel and nickel oxide presence in the post-reaction catalysts can be well visualized. DRM doesn't oxidize nickel particle in the studied process, while the presence of NO in the other catalytic tests lead to nickel oxidation to NiO. Moreover, $NiAl_2O_4$ can be seen thanks to the peak at around 2θ=67°. This peak has both Al_2O_3 and the spinel contribution, however, the form of the peak changes in the different samples, showing the spinel presence in certain cases. Al_2O_3 peak is asymmetric but quite sharp in alumina sample, and a contribution can be seen at the left of the peak center (2θ=67°) when nickel oxide is deposited, at around 2θ=66°. This contribution is the spinel that forms during the calcination of the sample, causing a moderate lift in the peak center position. Then, after reduction, the peak center is again at 2θ value of Al_2O_3, suggesting for a reduction on the spinel; however, the reduction of the spinel could be only partial as suggested by TPR results (see chapter 3.1.4.), so XPS experiments will be carried out to gain more information (see below). Finally, Al_2O_3 peak at 2θ=67.2° can be seen shifting again towards lower 2θ values (2θ=66.4°C) for the catalyst after DRM and nitric oxide reduction. The major shift could be attributed to the presence of a new specie, that forms during the process. This could be due to transformation of γ- Al_2O_3 to δ-Al_2O_3, that is expected at 750°C as reported in literature. [72]

Finally, XPS experiments were carried out to study surface of the post-reaction samples. Ni 2p detailed spectra were acquired to investigate the evolution of the nickel species present in the alumina samples, while C 1s detailed spectra were acquired to verify the absence of deposited carbon- as suggested by XRD results.

Ni 2p detailed scan were acquired for post-calcination catalyst NiO/Al_2O_3, post-reduction catalyst Ni/Al_2O_3, DRM spent catalysts and the catalysts after DRM and NO reduction process for 6 and 15 hours, as shown below (figure 75):

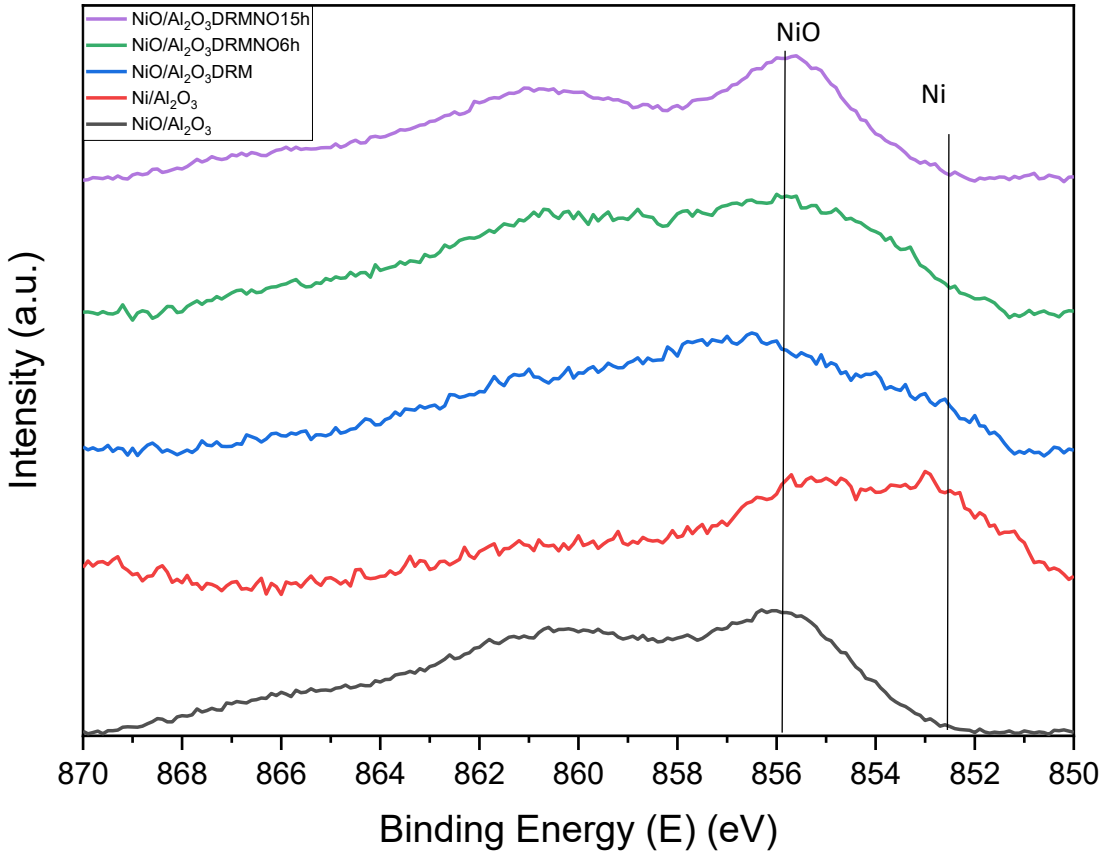

Figure 75 - Detailed XPS spectra of normalized Ni 2p photopeak for Ni/ Al_2O_3, NiO/ Al_2O_3, spent NiO/ Al_2O_3 after DRM, spent NiO/ Al_2O_3 after DRM and nitric oxide reduction process for 6 and 15 hours samples

Comparison among the different catalysts allowed to see the increase in NiO contribution with the hours of exposure to nitric oxide gas. The post-reaction catalyst NiO/Al_2O_3 after DRM and nitric oxide reduction process for 15 hours showed complete oxidation of nickel to nickel oxide, confirming the results obtained with XRD analysis above.

At last, C1s detailed scan were acquired for post-calcination catalyst NiO/Al_2O_3, post-reduction catalyst Ni/Al_2O_3, DRM spent catalysts and the catalysts after DRM and NO reduction process for 6 and 15 hours, as shown below (figure 76):

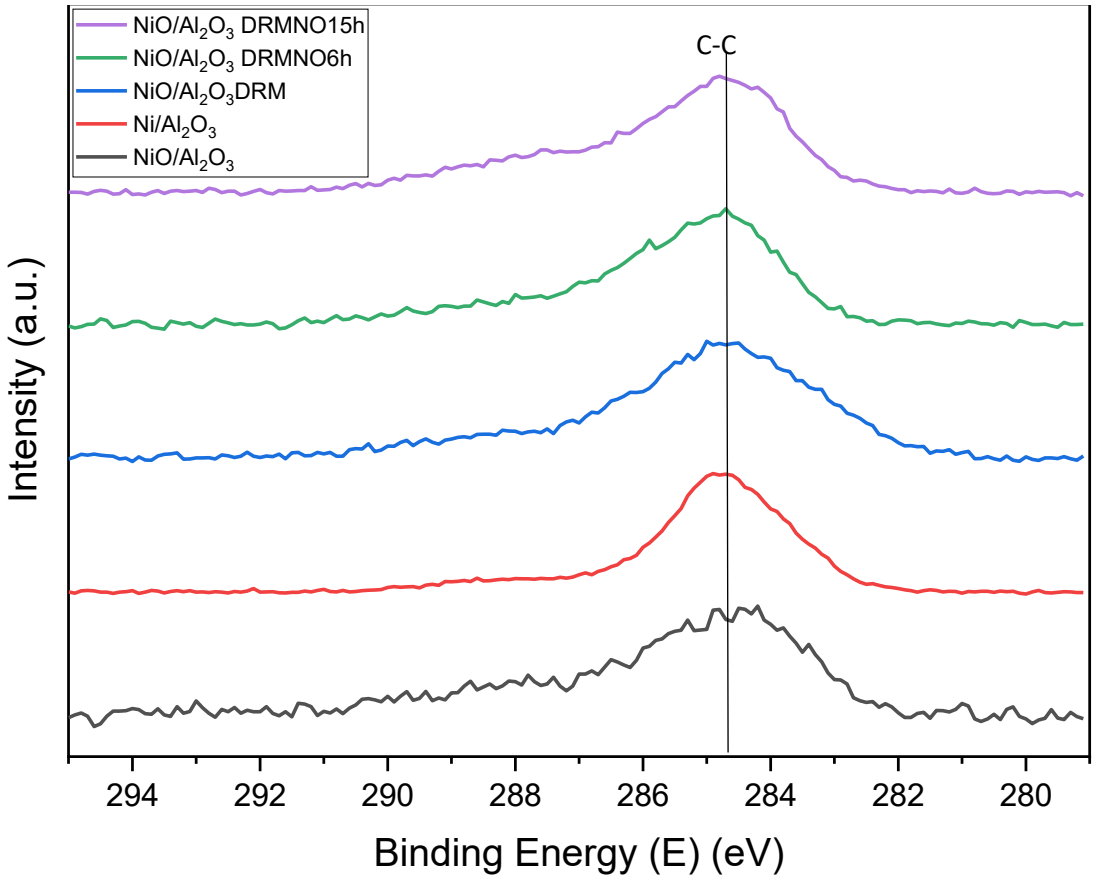

Figure 76 - Detailed XPS spectra of normalized C 1s photopeak for Ni/ Al_2O_3, NiO/ Al_2O_3, spent NiO/ Al_2O_3 after DRM, spent NiO/ Al_2O_3 after DRM and nitric oxide reduction process for 6 and 15 hours samples

The graph shows the presence of adventitious carbon at 284.8 eV for all samples, therefore confirming the presence of adventitious carbon as main surface carbon specie for all samples. Only sample NiO/Al_2O_3 after DRM reaction showed an additional contribution, visible in the shoulder at the right of the peak. To better investigate this contribution, NiO/Al_2O_3 after DRM was plotted with NiO/Al_2O_3 peak in figure 77 below:

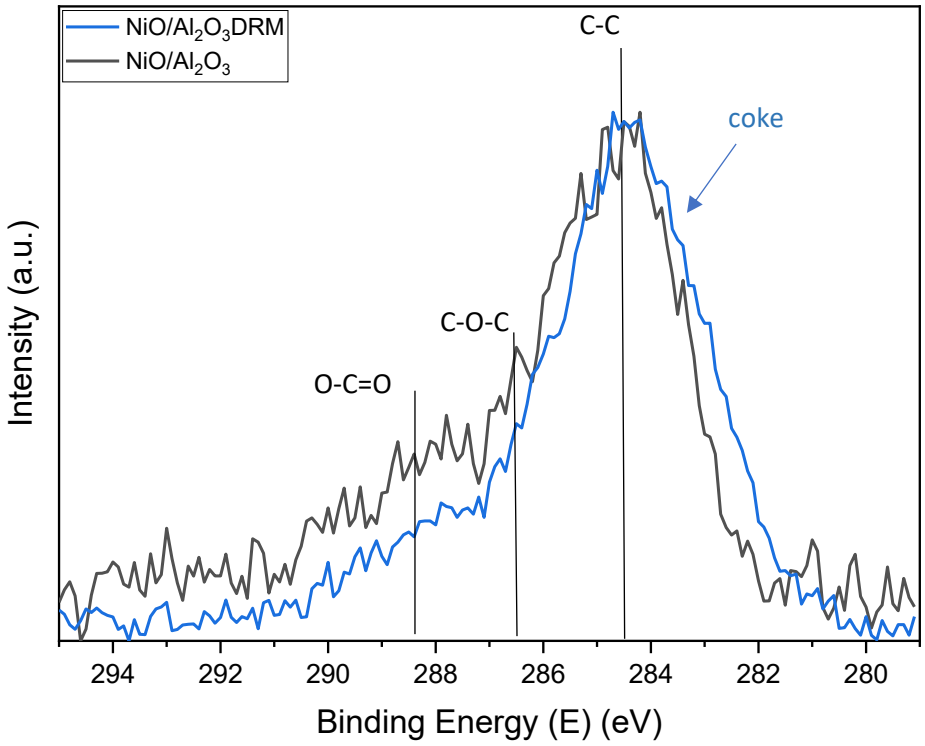

Figure 77 - Detailed XPS spectra of normalized C 1s photopeak for NiO/ Al_2O_3(black) spent NiO/ Al_2O_3 after DRM (blue) samples

From figure 77 it is possible to see a difference in the peak shape in the two samples: while NiO/Al_2O_3 shows the typical asymmetric shape of adventitious carbon, NiO/Al_2O_3 after DRM shows a symmetrical peak with a contribution around 284 eV that could be due to a small quantity of carbon that deposits on the catalyst during DRM. However, due to the little contribution of the deposited carbon to the adventitious carbon peak, the precise peak position could not be determined, and consequently no additional information was gained about the specie of carbon deposited. Therefore, catalytic tests with different reaction conditions will be needed to allow proper carbon deposition and determine its nature by XPS and XRD measurements (see after).

2 - NiO/$MgAl_2O_4$- Al_2O_3

NiO/$MgAl_2O_4$- Al_2O_3 catalyst was then analyzed, keeping the reaction conditions specified above (15 hours tests) in order to compare the catalytic activity among the different samples. Obtained conversions and yields are plotted against time in the graphs below (figures 78 and 79):

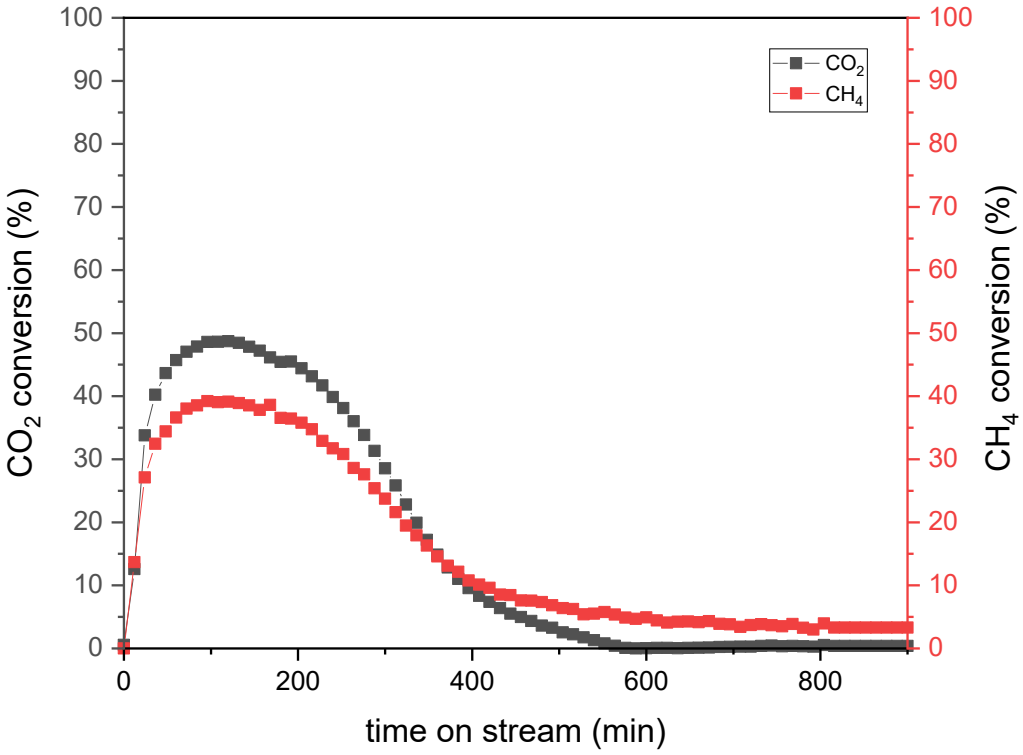

Figure 78- CH_4 and CO_2 conversions vs time measured for NiO/ $MgAl_2O_4$-Al_2O_3 at 750°C under gas stream of 5% CH_4, 5% CO_2, 1% NO for 900 minutes

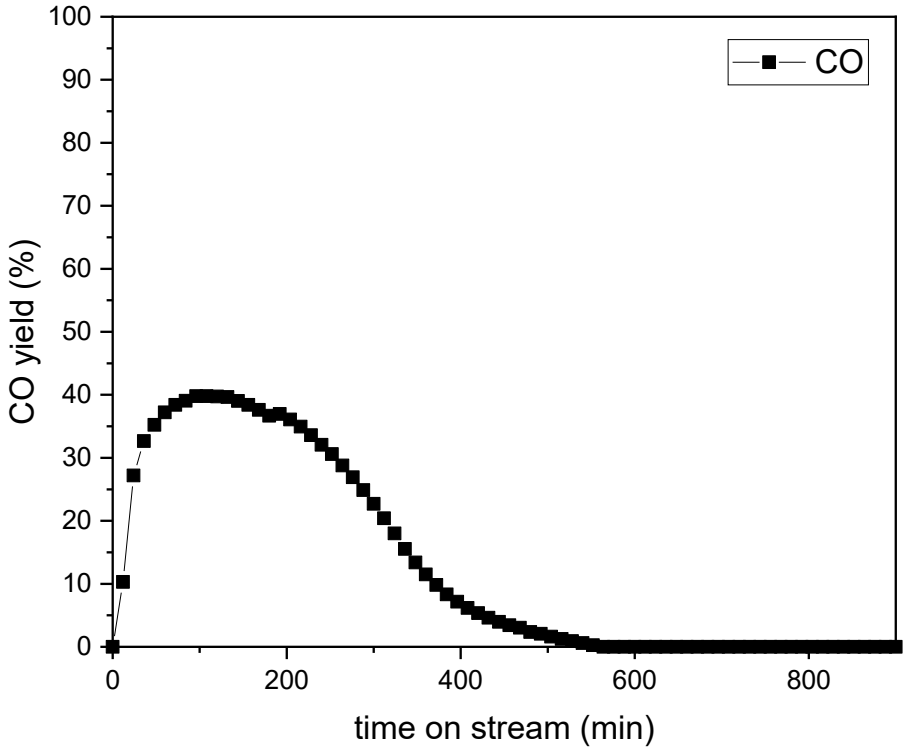

Figure 79- CO yield vs time measured for NiO/$MgAl_2O_4$-Al_2O_3 at 750°C under gas stream of 5% CH_4, 5% CO_2, 1% NO for 900 minutes

The graph showed higher CO_2 conversion compared to CH_4 conversion, as expected for a catalyst with a support characterized by basic properties (see chapter 1.3.1.). Catalytic activity showed a broader range of stability then NiO/Al_2O_3 catalyst, with CO_2 and CH_4 conversions and CO yield being stable between 100 and 200 minutes. Finally, while CO_2 conversion trend is coherent with CO yield, methane keeps being converted even when no CO is anymore produces. This could be due to NO reaction with CH_4, as reported in literature and seen above. [18]

Finally, spent catalyst was analyzed via XRD technique, and compared to the support peaks as well as the peaks of the post-calcination and post-reduction catalyst for a better attribution of crystalline phases.

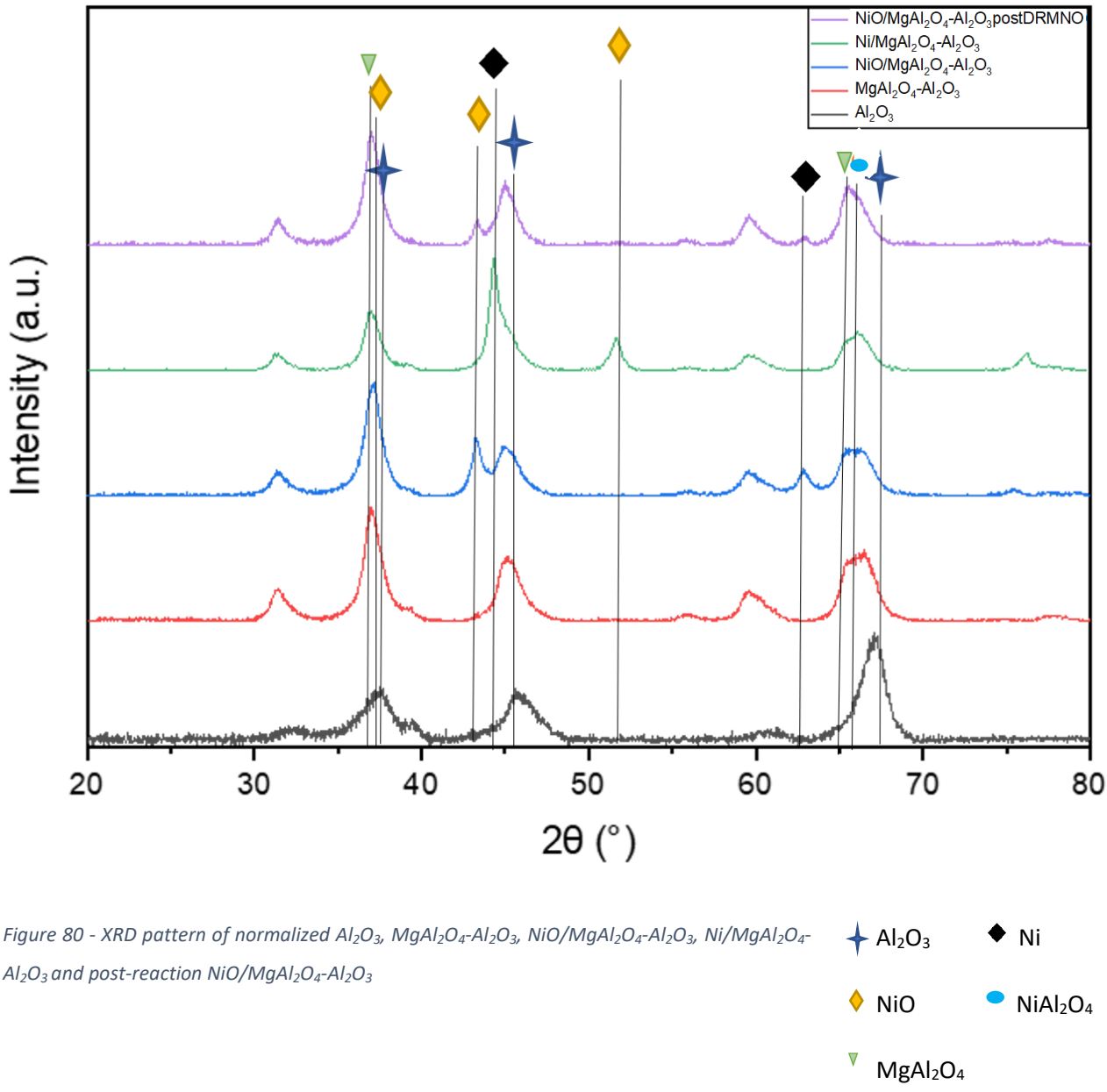

Figure 80 - XRD pattern of normalized Al_2O_3, $MgAl_2O_4$-Al_2O_3, $NiO/MgAl_2O_4$-Al_2O_3, $Ni/MgAl_2O_4$-Al_2O_3 and post-reaction $NiO/MgAl_2O_4$-Al_2O_3

XRD analysis (figure 80) allowed to see the presence of nickel oxide after the reaction, with only a small peak present for the remained nickel at around 63°. The support showed a change in the form of the peak centered at around 2θ=66°. This peak has a visible contribution of $MgAl_2O_4$ spinel on the left, and Al_2O_3 on the right, as for the other samples $NiO/MgAl_2O_4$-Al_2O_3 and $Ni/MgAl_2O_4$-Al_2O_3. However, the peak drastically changed among the samples. While $MgAl_2O_4$-Al_2O_3 shown an asymmetric peak with a smaller contribution of the $MgAl_2O_4$ spinel respect to Al_2O_3 contribution, visible in the difference of height between the left and right part of the peak, this changed after NiO calcination. An added contribution to the left of the peak makes the peak symmetric; this contribution is due to the nickel spinel that forms during calcination as for the NiO/Al_2O_3 catalyst. After reduction, the peak shape changes again, losing its nickel-spinel contribution (due to nickel reduction to its metallic form) and re-gaining its asymmetric shape. Finally, the post-reaction catalyst shows a different peak form, that has a contribution of a specie at lower 2θ values. This can be attribute to the partial transformation of γ-Al_2O_3 into δ-Al_2O_3, as for the previous catalyst.

3- $NiO/CaZrO_3$

$NiO/CaZrO_3$ was tested for dry reforming of methane coupled with nitric oxide reduction with using the same conditions of the previous catalysts. CO_2 and CH_4 conversions are plotted below against time, as well as CO yield (figures 81 and 82, respectively).

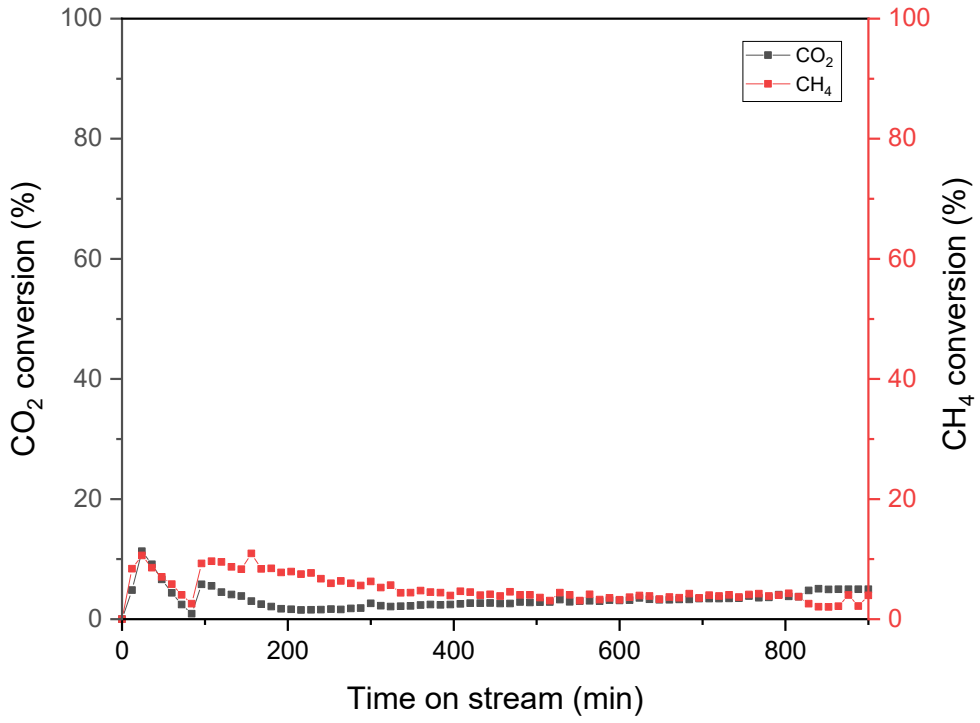

Figure 81- CH_4 and CO_2 conversions vs time measured for $NiO/CaZrO_3$ at 750°C under gas stream of 5% CH_4, 5% CO_2, 1% NO for 900 minutes

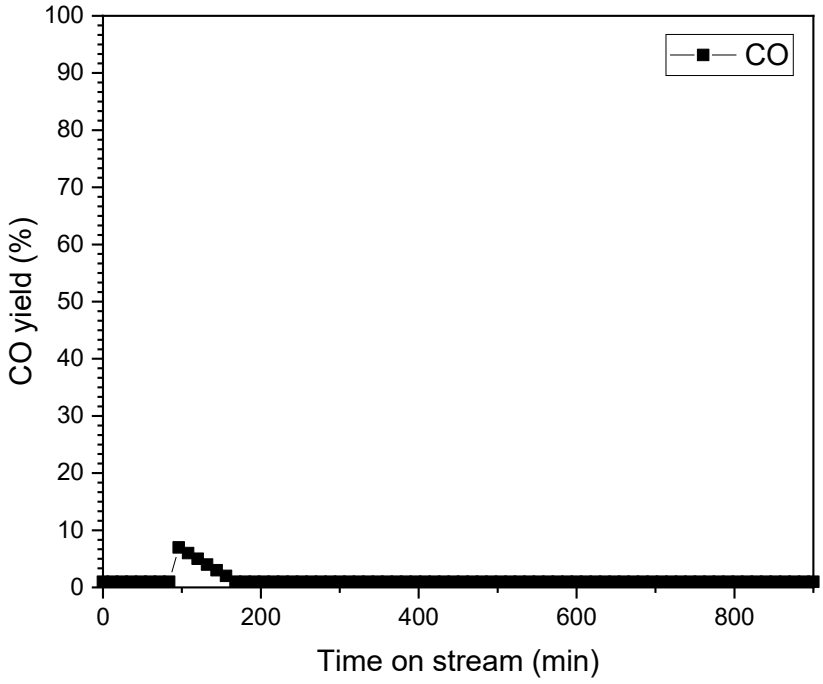

Figure 82- CO yield vs time measured for NiO/Al_2O_3 at 750°C under gas stream of 5% CH_4, 5% CO_2, 1% NO for 900 minutes

$NiO/CaZrO_3$ is characterized by low and unstable activity. Initially there was an increase in CO_2 and CH_4 conversions, but no CO was detected. This might be due to the production of very little CO quantity, that reacts with NO to re-obtain CO_2 gas. Then, between 100 and 160 minutes, CO_2 and CH_4 conversions are respectively around 5% and 10%, leading to CO's yield in a range of 2.46-0.57%. Part of CO can react with NO, therefore causing lower CO concentrations than expected. After this period of time, CO_2 and CH_4 conversions are steady and respectively around 2% and 5% value, but no CO was detected in the remaining time on stream. This could be explained as a reaction between methane and NO to give CO_2, so that no CO would be produced, but CH_4 could react with NO explaining its conversion values, giving CO_2 as product. This would explain as well CO_2 lower conversions compared to methane.

XRD pattern of the spent catalyst was then obtained and shown in figure 83, together with the post-calcination and post-reduction XRD patterns of the catalyst (figure 84):

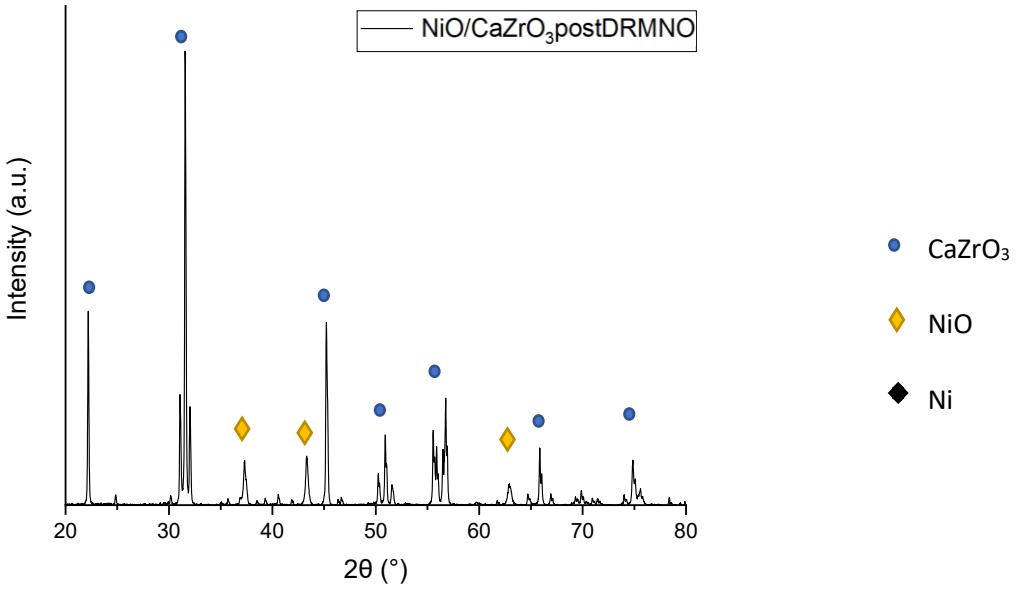

Figure 83 - XRD pattern of post-reaction NiO/$CaZrO_3$ catalyst

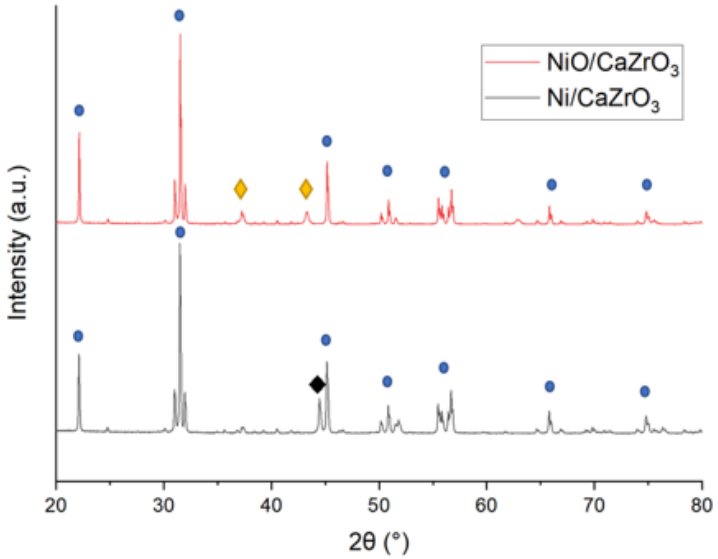

Figure 84- XRD pattern of NiO/ $CaZrO_3$ catalyst post-calcination (red) and post-reduction treatment (black) (until 900°C)

$Ni/CaZrO_3$ shows, after reaction, complete oxidation of nickel from its metallic active form after the reduction treatment ($Ni/CaZrO_3$ in figure 84) to its oxide form post-reaction (figure 83). Therefore, after the reaction the catalyst goes back in its oxidized form, as it is before the reduction treatments ($NiO/CaZrO_3$ in figure 84). This might be due to both the low metal support interaction of nickel particles with the perovskite support (see chapter 3.1.4.) and to the inability of the support to protect nickel particles from nitric oxide oxidizing power.

4- $NiO/LaFeO_3$

$NiO/LaFeO_3$ was finally tested for DRM process coupled with nitric oxide reduction. Graphs of CH_4 and CO_2 conversions and CO yield are shown below (figure 85 and 86):

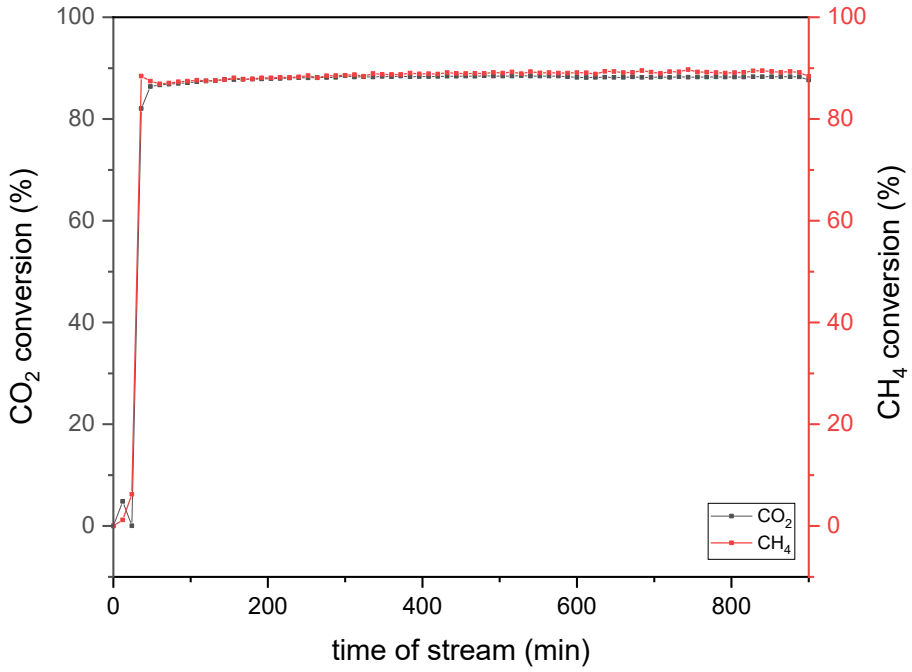

Figure 85- CH_4 and CO_2 conversions vs time measured for $NiO/LaFeO_3$ at 750°C under gas stream of 5% CH_4, 5% CO_2, 1% NO for 900 minutes

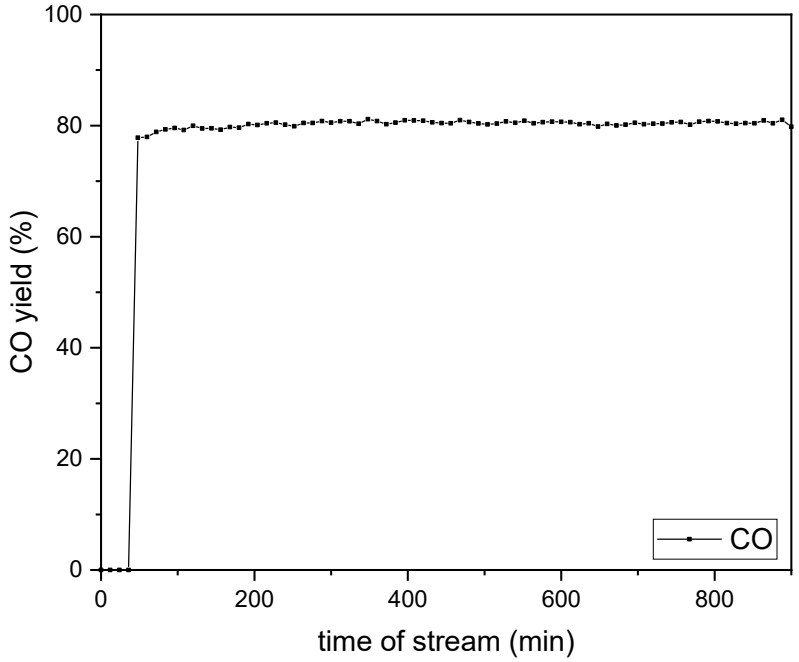

Figure 86- CO yield vs time measured for $NiO/LaFeO_3$ at 750°C under gas stream of 5% CH_4, 5% CO_2, 1% NO for 900 minutes

Tests revealed the best catalytic activity for this catalyst compared to the other samples. High and stable conversions around 90% were achieved during the 15 hours of tests. The stability of $NiO/LaFeO_3$ is guaranteed by $LaFeO_3$ support, which protects nickel particles from NO oxidation by making two NO molecules react to form N_2, as explained in chapter 1.3.2..

XRD pattern of the spent catalyst was then obtained to verify the catalyst stability (figure 86), and compared with the post-calcination and post-reduction pattern (figure 87):

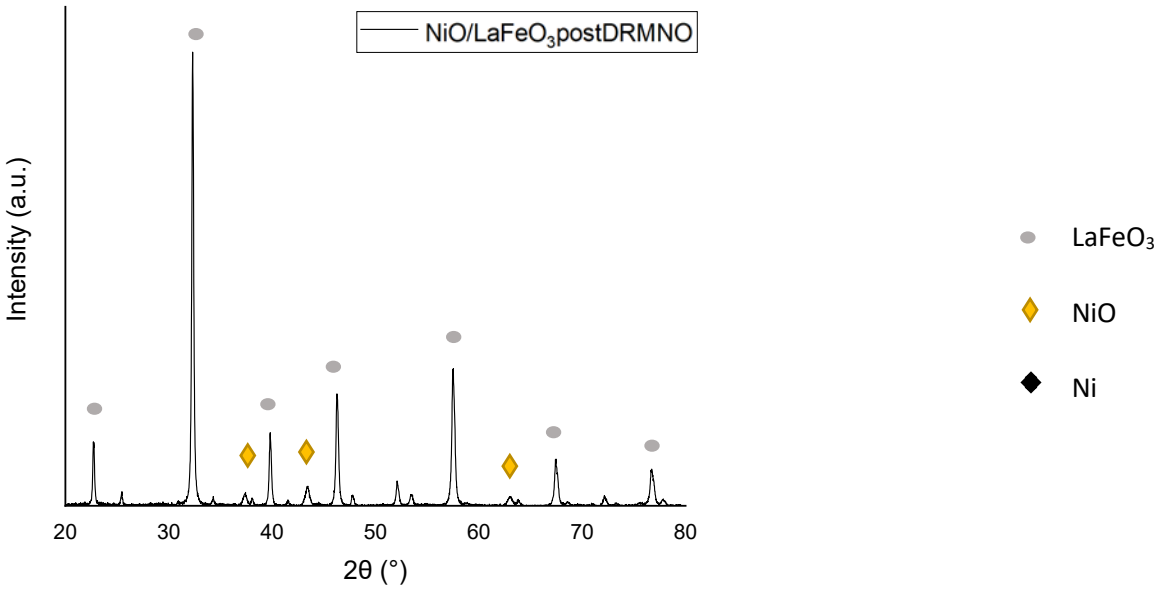

Figure 87- XRD pattern of post-reaction $NiO/LaFeO_3$ catalyst

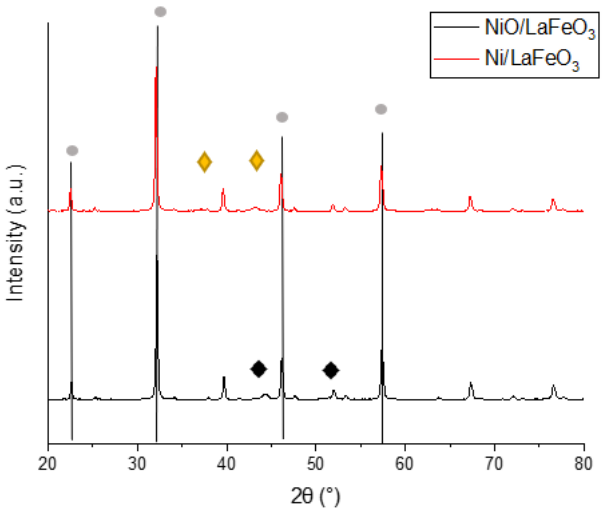

Figure 88- XRD pattern of $NiO/LaFeO_3$ catalyst post-calcination (black) and post-reduction treatment (red) (until 600°C)

XRD pattern of the spent catalyst (figure 87) showed nickel oxide presence, contrary on the predictions on finding nickel in its active metal form, as suggested by its catalytic activity (figures 85-86). However, considering the high and stable activity showed by the process, nickel must be present in its metallic form in the sample; nickel could be present in amorphous or highly distributed form, therefore not detectable by XRD technique. No coke was identified in the pattern of the spent catalyst, therefore suggesting- as for the other samples- the need of higher gas reactant concentrations to study coking phenomena.

4.2. Dry Reforming of Methane and Nitric Oxide Reduction: Second tests (25% CH_4, 25% CO_2, 1% NO)

Catalytic activity was finally measured for all samples using a gas mixture with higher methane and carbon dioxide concentrations in order to promote carbon deposition onto the catalysts. A gas mixture made of 25% CH_4, 25% CO_2, 1% NO and 49% Ar was chosen for the tests.

CO_2 and CH_4 conversions are reported below in graphs conversion versus time as for the first catalytic tests, while CO was not possible to be quantified due to lack of high concentration gas cylinder of CO for instrument calibration. Moreover, XRD patterns of the spent catalysts were acquired together with XPS data to evaluate catalysts' deactivation during the process.

4.2.1. Catalytic activity: Conversions and XRD analysis of the spent catalyst

1 - NiO/Al_2O_3

The first catalyst was tested for DRM coupled with NO reduction process; CO_2 and CH_4 conversions are plotted against time in graph 89 below:

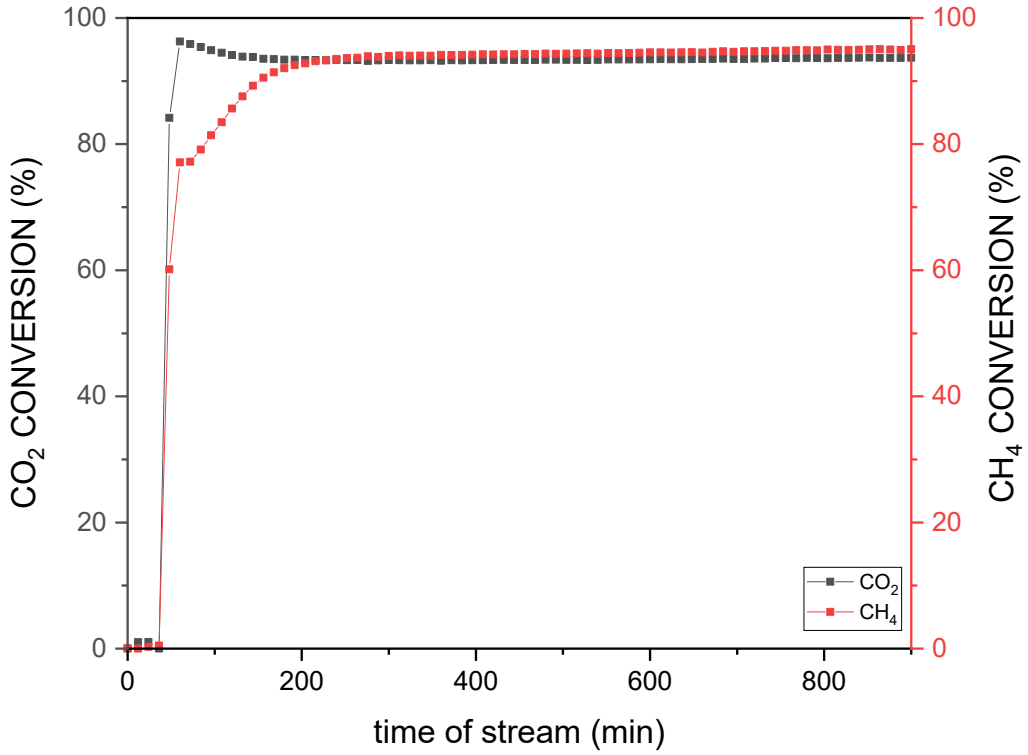

Figure 89- CH_4 and CO_2 conversions vs time measured for NiO/Al_2O_3 at 750°C under gas stream of 25% CH_4, 25% CO_2, 1% NO for 900 minutes

High and stable conversions were obtained by this catalyst, that were around 93% for CO_2 and 94% for CH_4. At the beginning of the experiment, high CO_2 conversions were achieved, while CH_4 arrived at his maximum activity after 200 minutes of reaction, probably due to the presence of nickel in a non-active form, like $NiAl_2O_4$ or Ni strongly interacting with the support. In the course of reaction, as H_2 develops during the process, nickel can be reduced in its active metal form. CO_2 conversions, on the other hand, slightly diminished until 200 minutes of reaction, passing from around 96% to 93%; this might me explained with a contribution to CO_2 concentrations due to both CO disproportionation reaction (4) and nitric oxide reaction with coke (5) that give CO_2 as product, therefore causing higher CO_2 concentrations in the reaction mixture.

XRD pattern of the spent catalyst is shown below in figure 90, together with the post-calcination and post-reduction XRD patterns of the catalyst (figure 91):

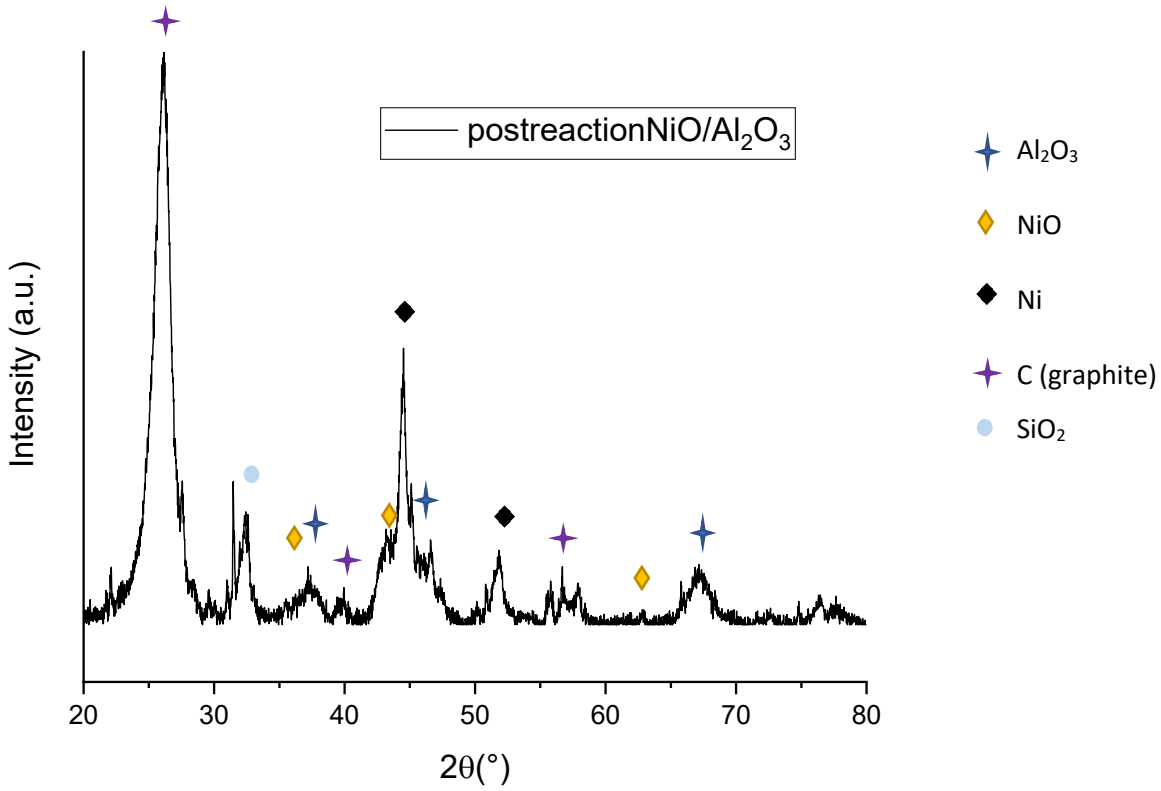

Figure 90 - XRD pattern of post-reaction NiO/Al_2O_3 catalyst

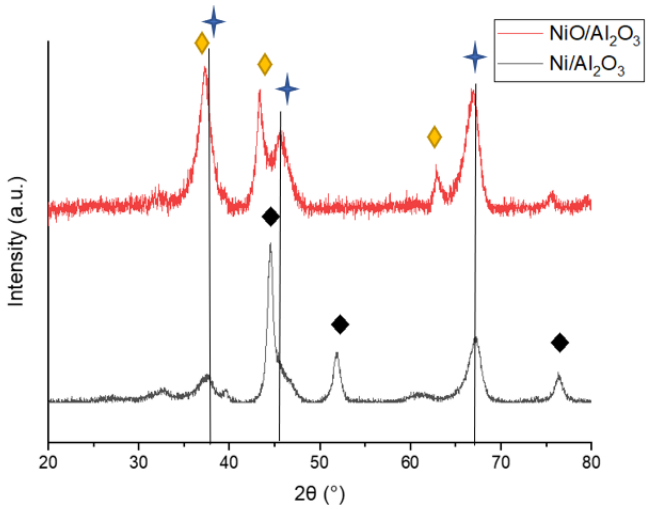

Figure 91 - XRD pattern of NiO/Al_2O_3 catalyst post-calcination (red) and post-reduction (black)

XRD pattern of the spent catalyst showed a relevant carbon deposition in form of graphite. Ni is present in its active metallic form, however little NiO is present in the pattern, though it doesn't cause activity problems, as can be deduced from the stability of the conversions. γ-Al_2O_3 support was not modified during the reaction. $NiAl_2O_4$ spinel was not detected by XRD analysis, probably because in the course of the reaction part of H_2 can reduce Ni^{II} of $NiAl_2O_4$ to its metallic form. Finally, SiO_2 impurities were found due the contamination of the sample with the quartz wool used in the experiment (see chapter 2.4.2.)

2 - $NiO/MgAl_2O_4$- Al_2O_3

$NiO/MgAl_2O_4$- Al_2O_3 was then tested for the process. CO_2 and CH_4 conversions are shown in the graph below (figure 92):

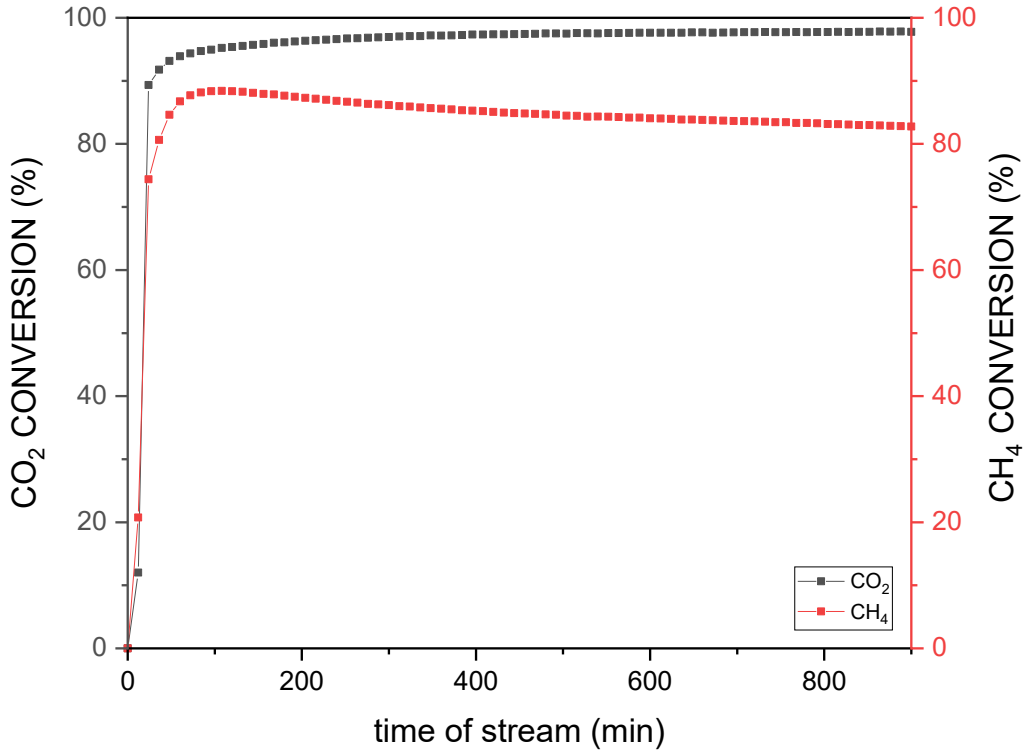

Figure 92- CH_4 and CO_2 conversions vs time measured for $NiO/CaZrO_3$ at 750°C under gas stream of 25% CH_4, 25% CO_2, 1% NO for 900 minutes

Conversion graph showed high CO_2 and CH_4 conversions. CO_2 conversion was higher than CH_4 thanks to the basicity of the support, as for the first catalytic test (see chapter 4.1.). This was the best catalyst for CO_2 conversion, with its 97% of constant conversion. CH_4 conversion, on the other hand, slightly diminished in the course of 15 hours, passing from around 88% to 82%. This might be due to nickel deactivation during the course of reaction due to sintering and coking.

The spent catalyst was studied via XRD measurements, as shown below (figure 93), together with the post-calcination and post-reduction XRD patterns of the catalyst (figure 94):

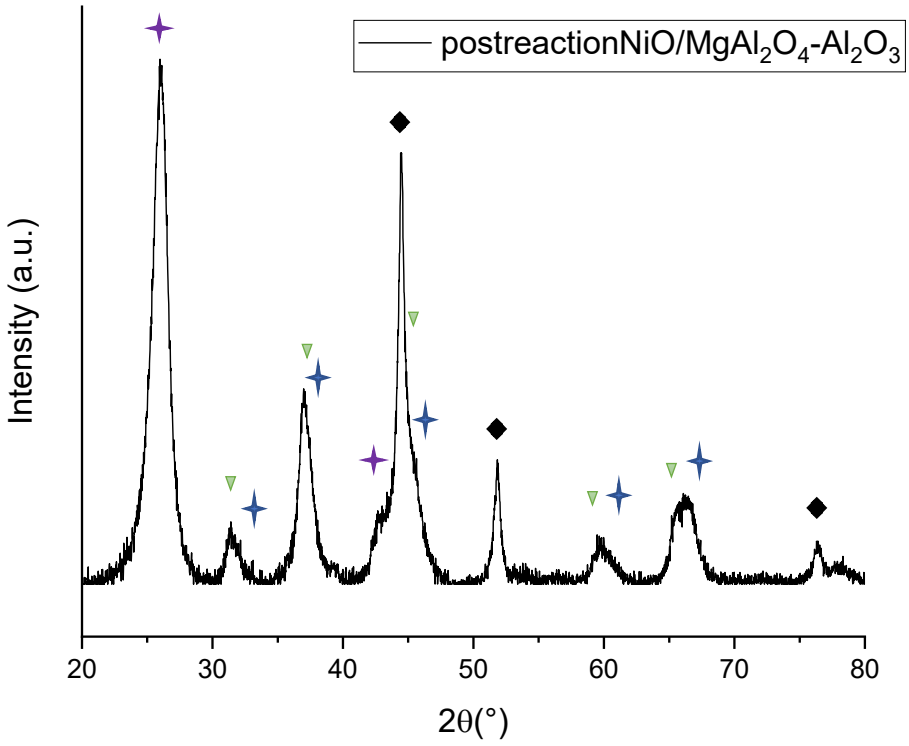

Figure 93 - XRD pattern of post-reaction NiO/$MgAl_2O_4$-Al_2O_3 catalyst

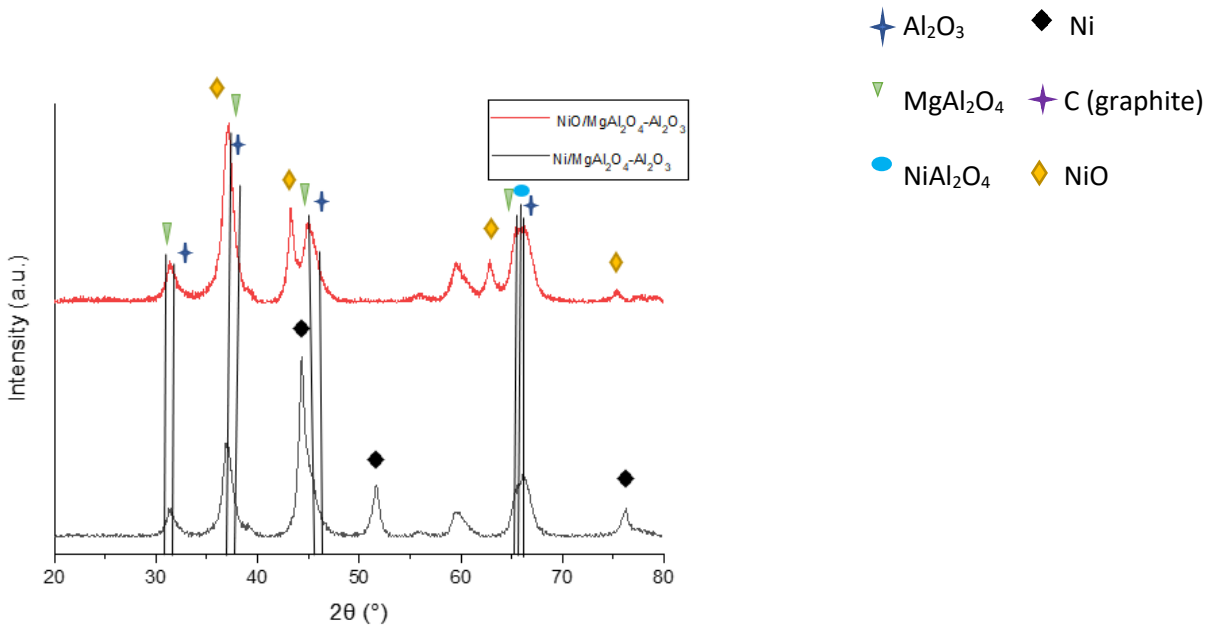

Figure 94 - XRD pattern of NiO/$MgAl_2O_4$-Al_2O_3 catalyst post-calcination (red) and post-reduction (black)

XRD pattern revealed the presence of graphitic carbon as for the previous sample; nickel was present in its metallic form and no nickel oxide was detected. No nickel spinel was detected, being probably reduced by H_2 produced in the process, while the support stayed for the rest unaltered.

3- $NiO/CaZrO_3$

$NiO/CaZrO_3$ catalyst was tested for the catalytic process, but no CO was detected during the process. Being catalytically inactive, $NiO/CaZrO_3$ conversion graphs won't be reported.

XRD pattern of the spent catalyst was acquired below, shown in figure 95 together with the post-calcination and post-reduction XRD patterns of the catalyst of figure 96:

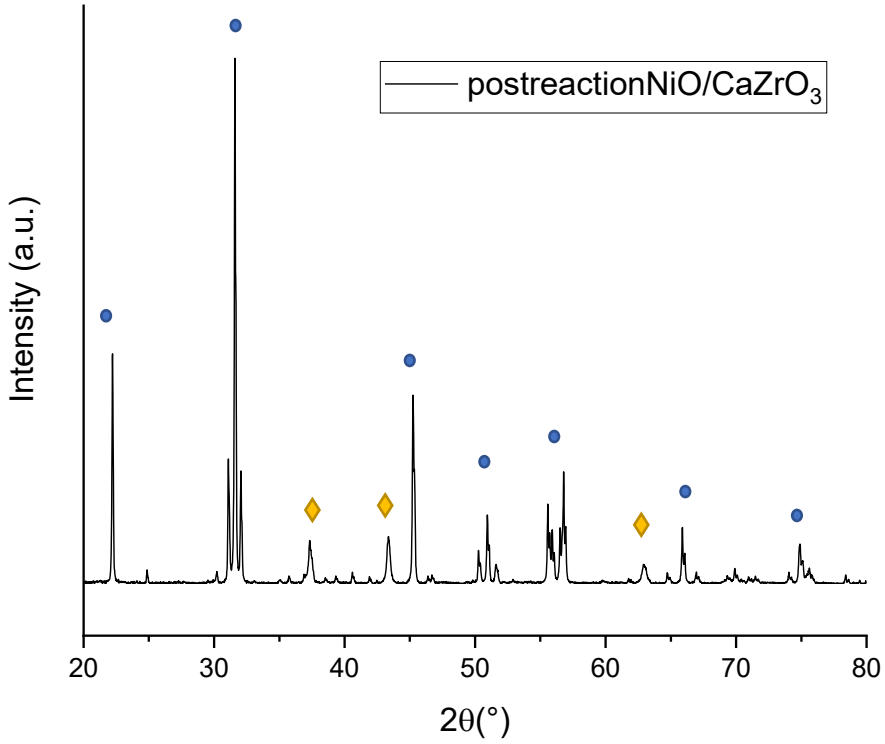

Figure 95 - XRD pattern of post-reaction $NiO/CaZrO_3$ catalyst

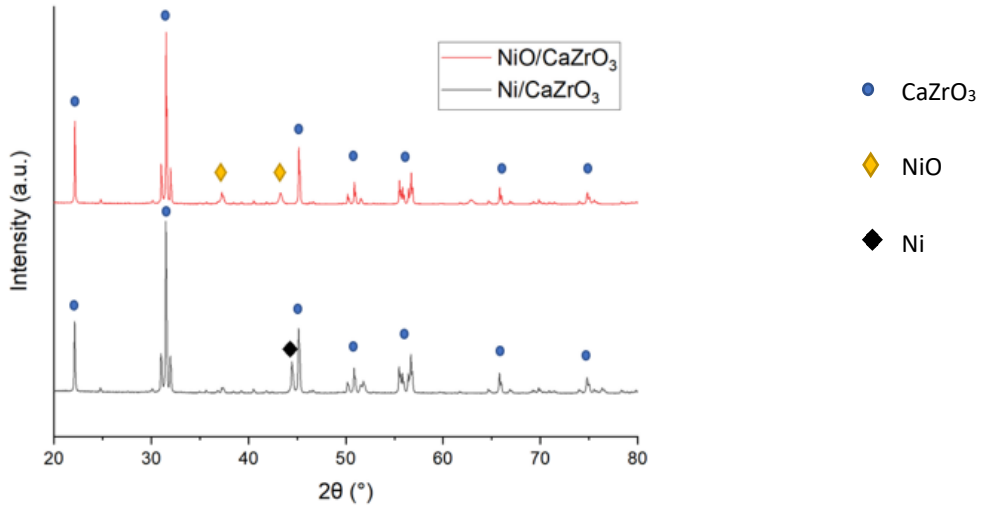

Figure 96- XRD pattern of $NiO/CaZrO_3$ catalyst post-calcination (black) and post-reduction treatment (red) (until 600°C)

Sample showed complete nickel oxidation after the process; this is in accordance with $NiO/CaZrO_3$ very low catalytic activity. Even if conditions were less oxidizing than in the first catalytic tests (chapter 4.1.), this perovskite was not a good support for nickel particles in this process, probably due to both the low metal-support interaction and the lack of protection of the particles from NO. Therefore, no carbon was deposited during the process as nickel was deactivated by oxidation before carbon deposition could happen.

4- $NiO/LaFeO_3$

At last, $NiO/LaFeO_3$ catalyst was tested. Its conversion percentages are shown in the graph below (figure 97):

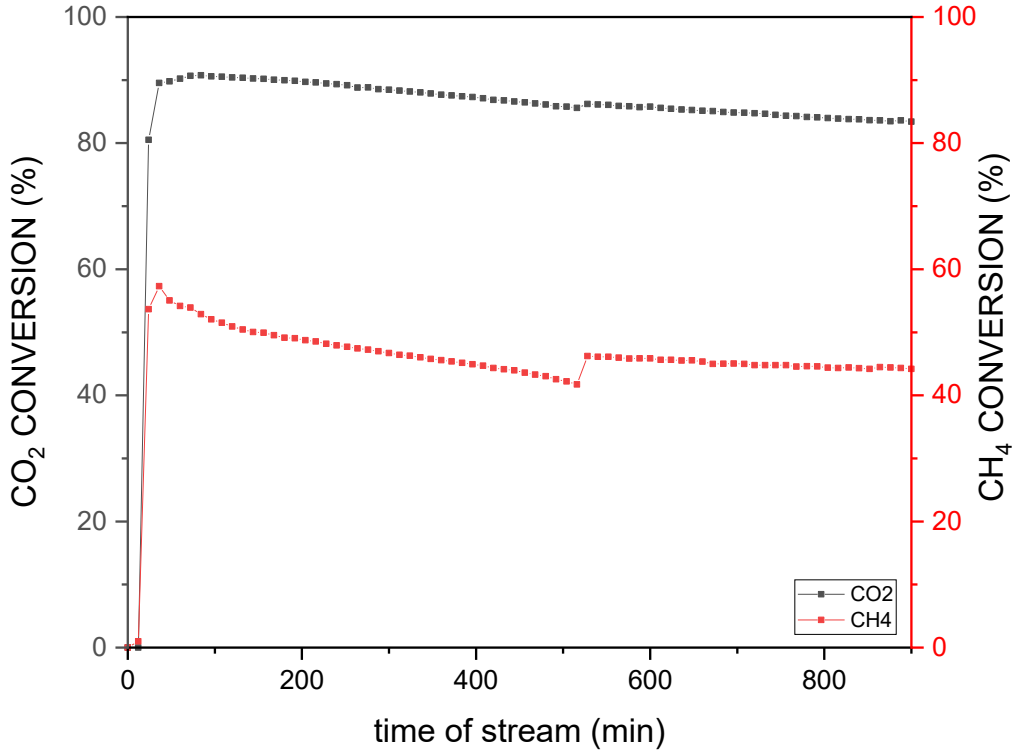

Figure 97- CH_4 and CO_2 conversions vs time measured for $NiO/LaFeO_3$ at 750°C under gas stream of 25% CH_4, 25% CO_2, 1% NO for 900 minutes

$NiO/LaFeO_3$ sample showed high CO_2 conversion around 91% at the beginning of the reaction, that then diminishes until 83% at the end of the process. CH_4 conversions started from 55% and then decreased until 44%, with a sudden increase at around 516 minutes. This sudden increase might be due to an instrumental error related to the gas concentrations streamed into the reactor. Comparing the activity recorded in this test and the one with 1/5 of reactant percentage (chapter 4.1.), it appears that the catalyst doesn't have the same stability of conversions in the studied range of time as in the test before. Conversions slowly decrease as time passes for this support, different from alumina-based catalysts' behavior. This might be due to the

weaker metal support interaction of nickel particles in the perovskite catalyst, which will be more sensitive to sintering and coking during the reaction, leading to a slow decrease in catalytic activity. It is important also to remember that perovskite-based catalysts are characterized by low surface area values (1 order of magnitude difference with alumina-based samples), that can have an impact on the catalytic behavior of the sample.

XRD pattern of the post-reaction catalyst was finally obtained (figure 98), together with the post-calcination and post-reduction XRD patterns of the catalyst of figure 99:

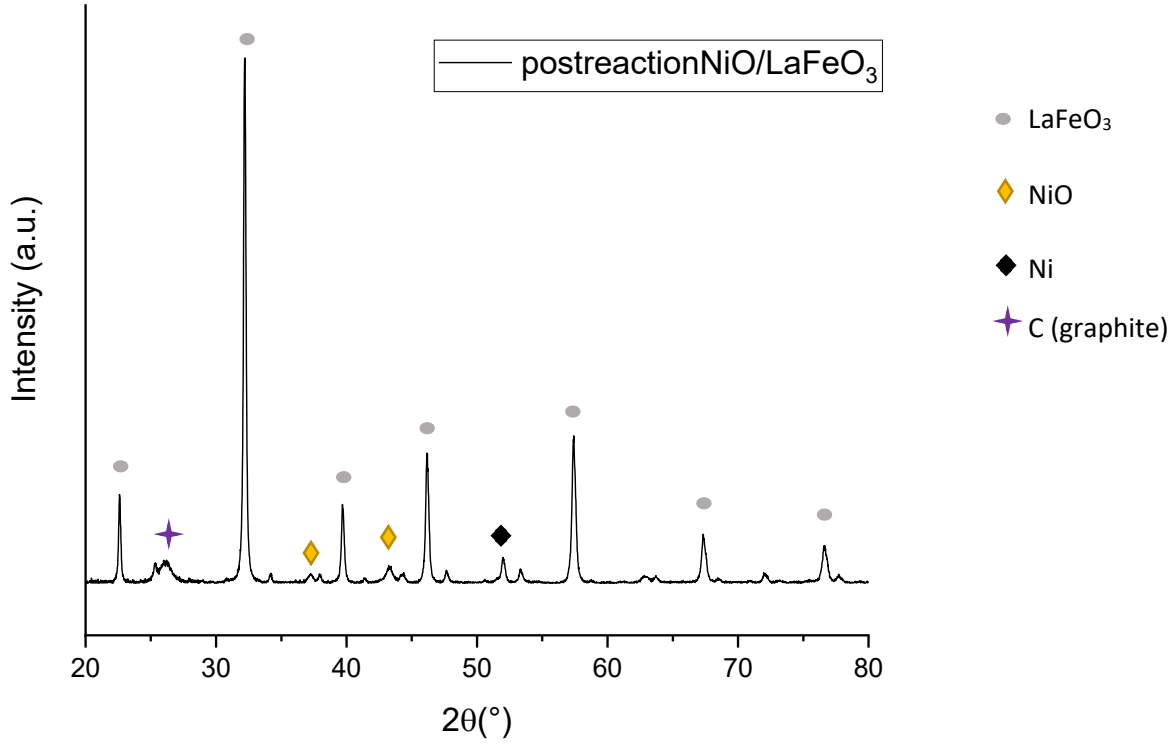

Figure 98 - XRD pattern of post-reaction $NiO/LaFeO_3$ catalyst (catalytic activity measured after reductive treatment in 5% H_2 in Ar, with 25% CO_2 25% CH_4 and 1% NO gas flow)

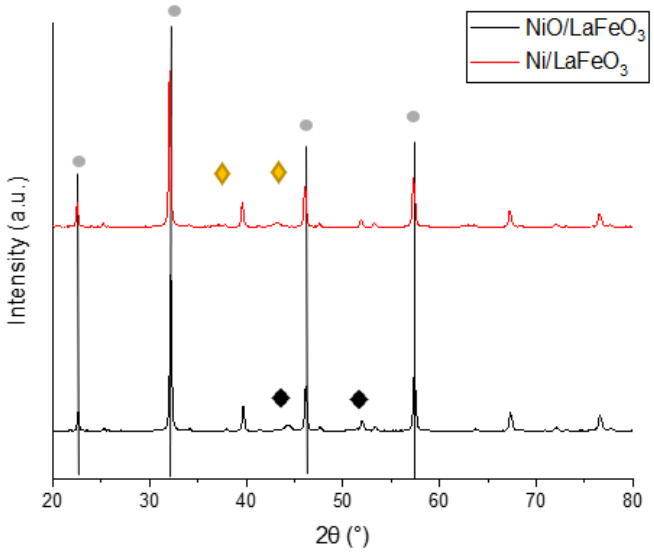

Figure 99 - XRD pattern of $NiO/LaFeO_3$ catalyst post-calcination (black) and post-reduction treatment (red) (until 600°C)

The catalyst showed the presence of graphitic carbon and partial nickel oxidation to NiO as in the other samples; the support remained unaltered during the 15 hours process.

We can conclude that the chosen conditions allowed coke development on all catalysts, except for $NiO/CaZrO_3$ who showed no relevant catalytic activity. With the aim to better characterize the deposited carbon and to understand the differences among the samples, XPS studies will be conducted in the next chapter.

4.2.2. Coke: type and reactivity of the deposited carbon

Carbon that deposits onto the catalysts was analyzed at first via XRD experiments (see chapter 4.2.1.), then XPS analysis was conducted in order to do investigate the first nanometers of carbon that deposits onto the catalyst during 15 hours of reaction. XPS analysis allows to study, via C 1s photopeaks, the different types of carbon that deposits onto the surface of the catalysts. Moreover, XPS allows to evaluate the amount of carbon (in terms of atomic percentage). Therefore, by comparing post-reduction samples and post-reaction samples, it is possible to appreciate the type and relative quantity of carbon deposited during the reaction.

Finally, it is interesting to understand the reactivity of the deposited carbon, that gives information about the easiness with which carbon can be removed in order to avoid catalysts deactivation (see chapter 1.1.2.).

4.2.2.1. XPS study on the deposited carbon

In order to have an idea about the quantity of carbon deposited during the process, semi-quantitative analysis of surface compositions was made on the samples, by integrating C1s photopeak in the extended spectra and using the instrumental sensitivity factors and a Shirley-type background as explained in chapter 3.1.6..

XPS extended spectra were recorded for all samples, as shown in the figure 100 below:

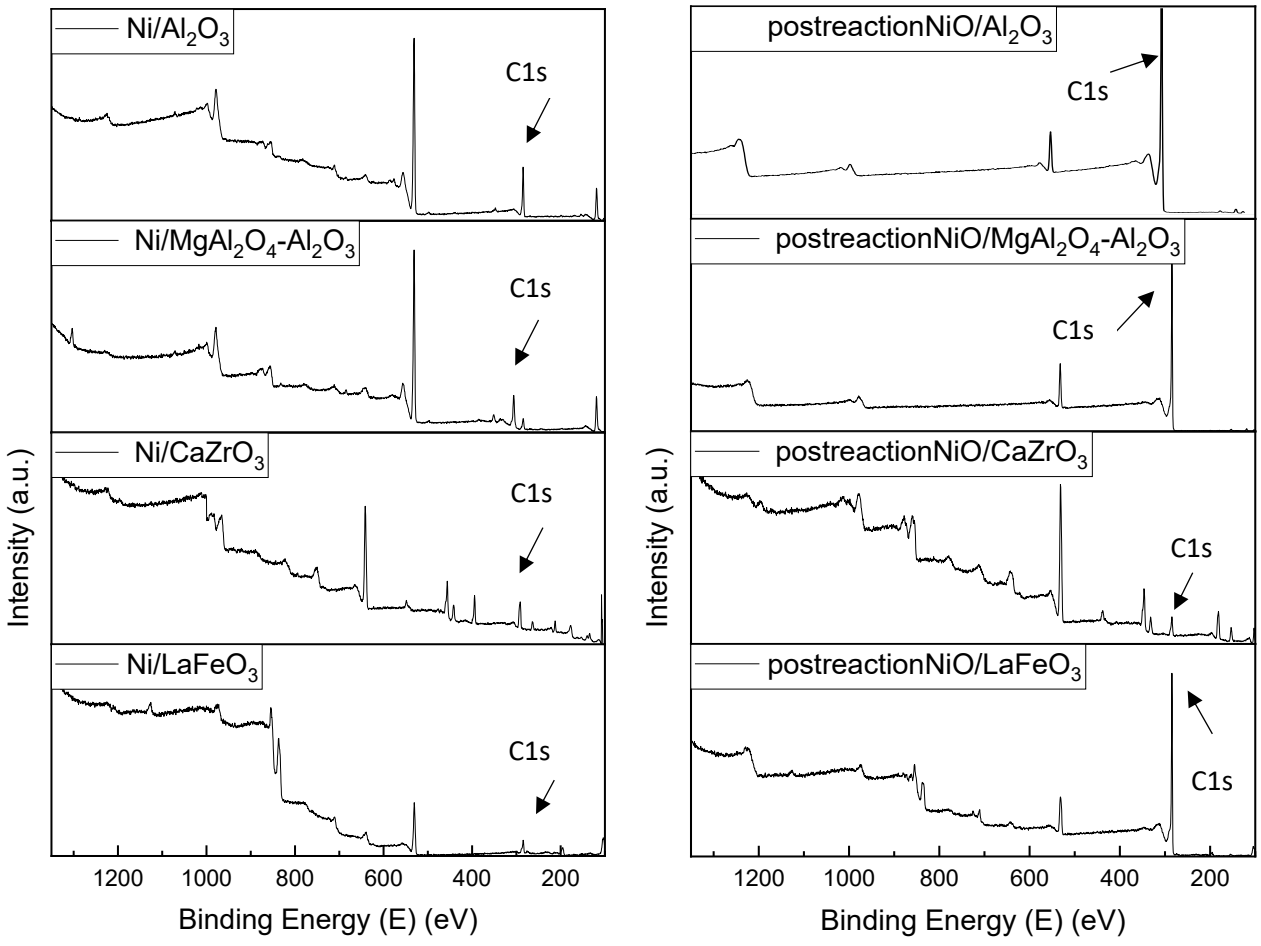

Figure 100- Extended XPS spectra for all post-reduction (on the left) and post-reaction (on the right) catalysts

From the graphs above, it is possible to appreciate a drastic change in the relative intensity of carbon before and after catalytic activity for all catalysts except for the $CaZrO_3$ supported. This confirms the depositions of carbon on the surface of the samples, therefore indicating the coking of the samples. In order to have an estimation of the quantity of carbon deposited, in XPS spectra were identified the elements characteristics

of the catalysts thanks to their binding energy positions, and the integration of each element main photopeak was performed as described in chapter 3.1.6..

Below in table 8, the calculated values of carbon surface compositions are reported and compared for post-reduction catalysts and post-reaction catalysts:

Table 8- XPS (5-10 nm depth) elemental quantifications for C, calculated for post-reduction and post-reaction samples.

Support	Post-reduction C atomic surface composition (at. %)	Post-reaction C atomic surface composition (at. %)
Al_2O_3	26.0	89.3
$MgAl_2O_4$-Al_2O_3	8.6	85.9
$CaZrO_3$	28.9	15.1
$LaFeO_3$	31.4	82.9

As expected, carbon atomic percentage drastically increases after catalysis for all samples except $NiO/CaZrO_3$. Considering the low activity of the latter, as seen in chapter 4.1., the lack of carbon might be due to the immediate deactivation of the catalyst, which is not able to sustain enough hours of the process to let the coking process happen. However, this will be more discussed with the aid of the detailed XPS C1s spectra showed below. Regarding the rest of the catalysts, post-reaction catalysts have higher carbon surface composition for acidic catalysts, such as post-reaction NiO/Al_2O_3, than the basic catalysts post-reaction $NiO/MgAl_2O_4$-Al_2O_3 or $NiO/LaFeO_3$. Moreover, post-reaction $NiO/LaFeO_3$ shows the lowest concentration of carbon on its surface, better than $NiO/MgAl_2O_4$-Al_2O_3; this could be related either to its basicity and chemisorption capacity or to its capacity to interact with NO molecules and therefore facilitating NO gasification of coke.

To better understand the coking phenomena, detailed C1s XPS spectra of all catalysts were acquired, as shown below.

1- NiO/Al_2O_3

The first catalyst was investigated by XPS, obtaining C1s photopeaks of Ni/Al_2O_3 and postreaction NiO/Al_2O_3. The photopeaks are shown in the figures below (figures 101 and 102, respectively):

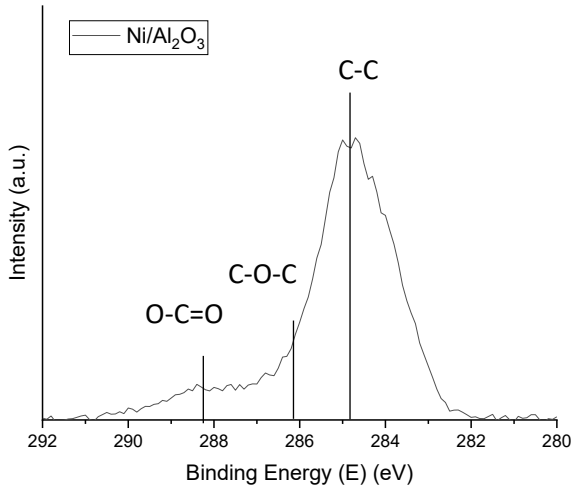

Figure 101- Detailed XPS spectra of C 1s photopeak for Ni/Al_2O_3

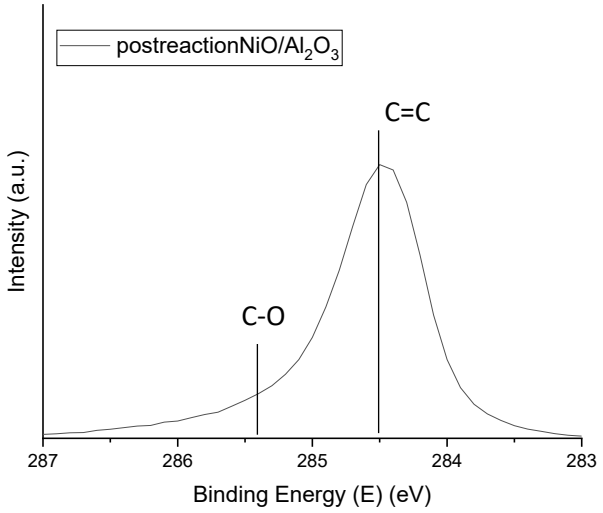

Figure 102- Detailed XPS spectra of C 1s photopeak for post-reaction NiO/Al_2O_3

Ni/Al_2O_3 sample showed C1s photopeak typical of adventitious carbon, with the reference peak C-C at 284.8 eV, and at higher Binding Energy typical contributions C-O-C and O-C=O are observed. After reaction, the catalyst showed a change in the peak position (that shifts at 284.5 eV) and shape, typical value for C-C of the graphitic carbon. A tail can be seen around 285-286 eV, which accounts for satellites of C1s. Therefore, XPS results confirm the presence of graphitic carbon obtained by XRD experiments (see chapter 4.1.).

2- $NiO/MgAl_2O_4$-Al_2O_3

The same analysis was made for $NiO/ MgAl_2O_4$-Al_2O_3 catalysts, as shown in figures 103 and 104:

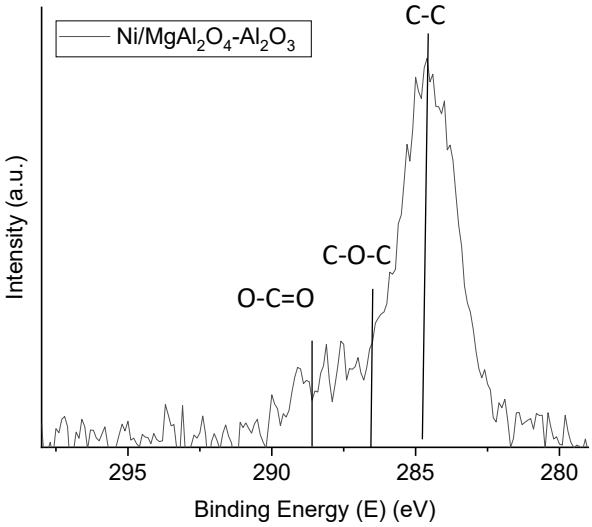

Figure 103- Detailed XPS spectra of C 1s photopeak for $Ni/MgAl_2O_4$ -Al_2O_3

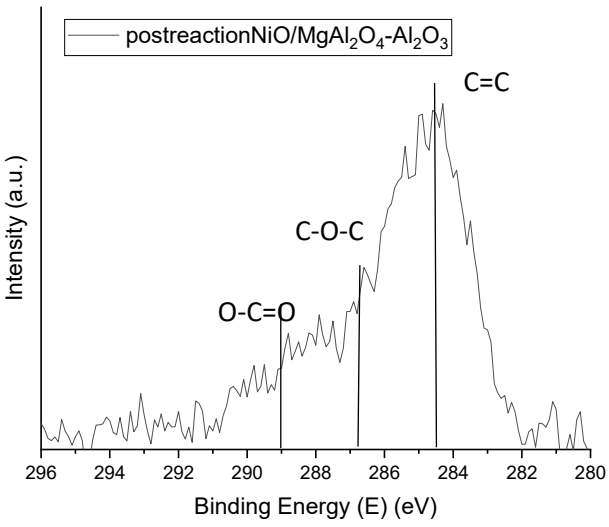

Figure 104- Detailed XPS spectra of C 1s photopeak for post-reaction $NiO/MgAl_2O_4$ -Al_2O_3

In this sample post-reduction catalyst showed C1s photopeak typical of adventitious carbon, while post-reaction catalyst had C1s photopeak in which the contribution of graphite is the main one. C-O-C and O-C=O components can be seen in both graphs. C=O might be due to carbonates species forming on the surface of the basic support, thanks to CO_2 interaction with the spinel. [73] In conclusion, a part from the predisposition of the supports in forming carbonates, XPS results of the samples confirm the presence of adventitious carbon in the post-reduction sample and the deposition of graphitic carbon after the catalytic process, in accordance with XRD results obtained in chapter 4.1..

3- $NiO/CaZrO_3$

C1s photopeaks for $Ni/CaZrO_3$ and postreaction $NiO/CaZrO_3$ were obtained, and shown in the graphs below (figures 105 and 106):

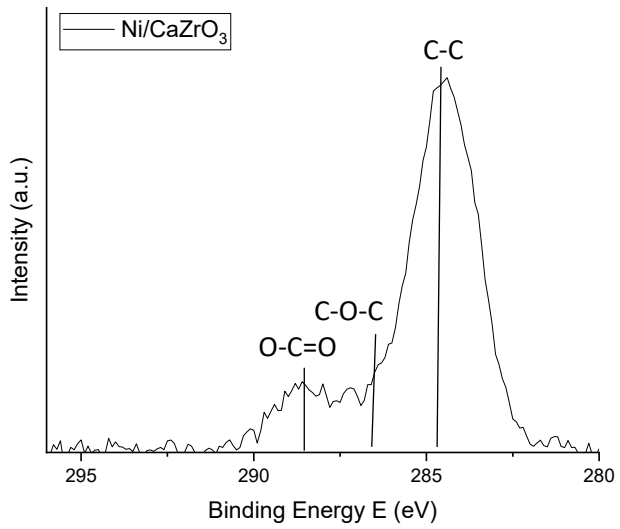

Figure 105- Detailed XPS spectra of C 1s photopeak for post-reaction $NiO/CaZrO_3$

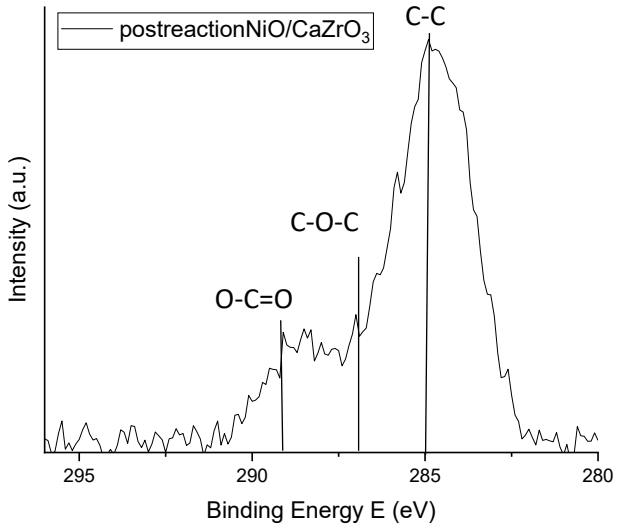

Figure 106- Detailed XPS spectra of C 1s photopeak for post-reaction $NiO/CaZrO_3$

$CaZrO_3$ supported catalysts showed C1s photopeak typical of adventitious carbon, both for its post-reduction catalyst and post-reaction catalyst. XPS results of the samples confirm the absence of deposited carbon in the catalyst after the catalytic activity, as was suggested by XRD results in chapter 4.2.1..

4- $NiO/LaFeO_3$

Finally, C1s photopeaks of $Ni/LaFeO_3$ and postreaction $NiO/LaFeO_3$ were obtained for the last catalyst. C1s photopeaks are shown in the graphs below (figures 107 and 108):

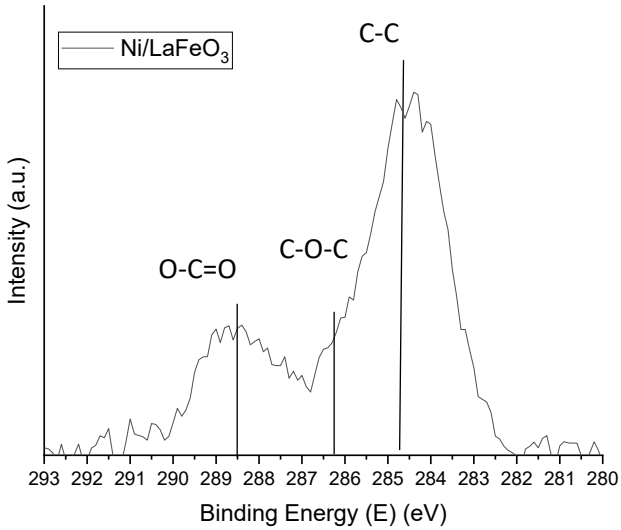

Figure 107- Detailed XPS spectra of C 1s photopeak for post-reaction $NiO/LaFeO_3$

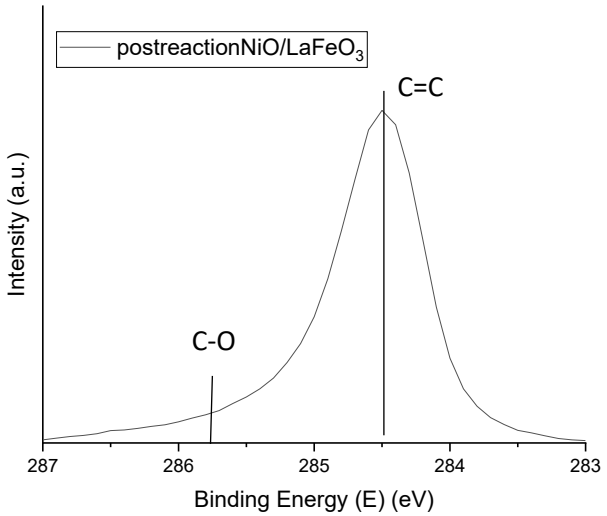

Figure 108- Detailed XPS spectra of C 1s photopeak for post-reaction $NiO/LaFeO_3$

This catalyst shows a similar behavior as the previous samples, with adventitious carbon characterizing $Ni/LaFeO_3$ sample, and graphitic carbon in the post-reaction sample. While O-C=O contribution is well visible in post-reduction catalyst, after the catalytic process this contribution is no longer visible, probably due to the high quantity of graphitic carbon deposited onto the catalyst.

We can conclude that graphitic carbon was the type of carbon that deposited on all samples subjected at coking phenomena, confirming XRD results. However, in order to investigate possible differences in the reactivity of the carbon, its gasification abilities will be tested via TPO experiments in the chapter below.

4.2.2.2. Gasification ability of the deposited carbon

In order to study the reactivity of the deposited carbon, O_2-TPO experiments were carried out, to exploit the oxidizing power of O_2 or NO gasses to remove the carbon from the catalysts surface. O_2-TPO experiments are a conventional method for studying and characterizing the deposited coke; experiments were carried out with 5% O_2 in Ar, in temperature ramp at 10°C/min, from less than 100°C to 900°C, and then in descending

temperature ramp. Depending on the temperature at which the coke gasifies and based on the quantity of CO_2 produced, information about carbon reactivity can be gained.

The graphs obtained by O_2-TPO experiments are shown below, with CO_2 concentration on Y axis and time/temperature on X axis (figures 109-111).

1- NiO/ Al_2O_3

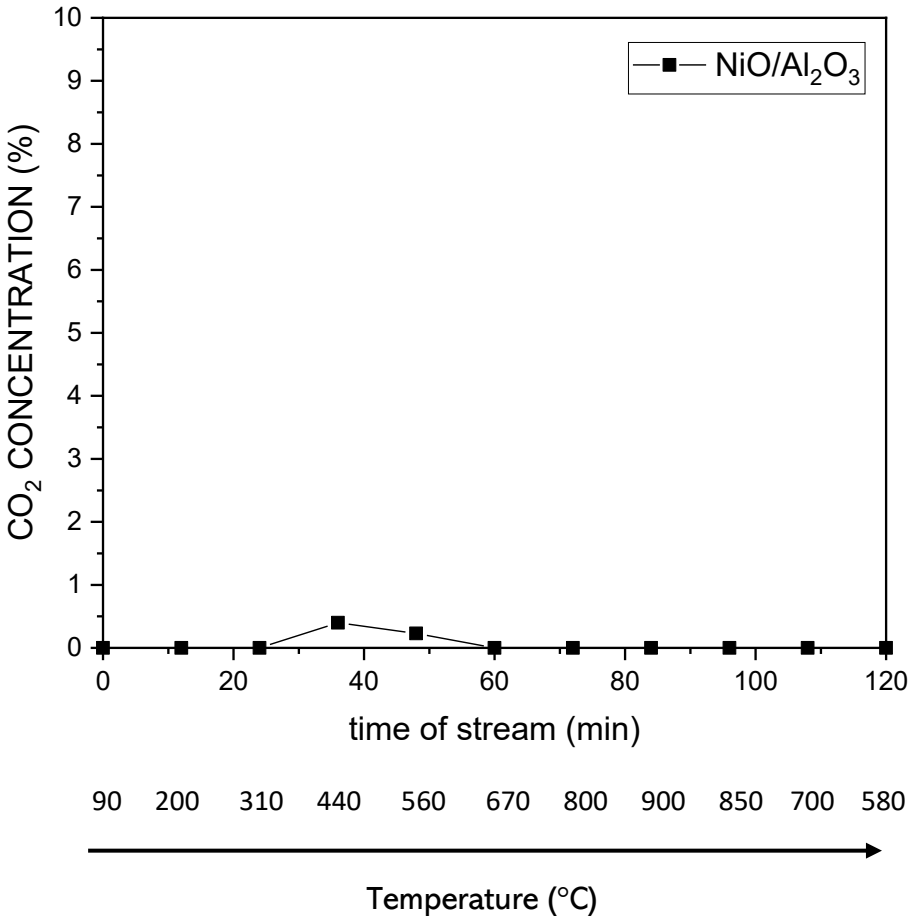

Figure 109- CO_2 concentration vs time measured for post-reaction NiO/Al_2O_3 (25% CH_4, 25% CO_2, 1% NO) obtained by using a 5% O_2 gas flow and a temperature ramp (room temperature-900°C)

The graph shows CO_2 development between 300 and 600°C. This temperature range is indicative of the gasification of amorphous carbon, as can be found in literature. [74] However, NiO/ Al_2O_3 catalyst was characterized by a significant quantity of graphitic carbon, detected both by XRD and XPS experiments (see chapter 4.2.1. and 4.2.2.1.). This, together with the low concentration of CO_2 obtained respect to the other

catalysts, suggests that the majority of the carbon deposited onto the sample is in graphitic form and has not been gasified by the oxidative treatment. This is an expected result as the acidic properties of the alumina support do not help with coke gasification and the needed CO_2 chemisorption (see chapter 1.3.1.).

2- $NiO/MgAl_2O_4$-Al_2O_3

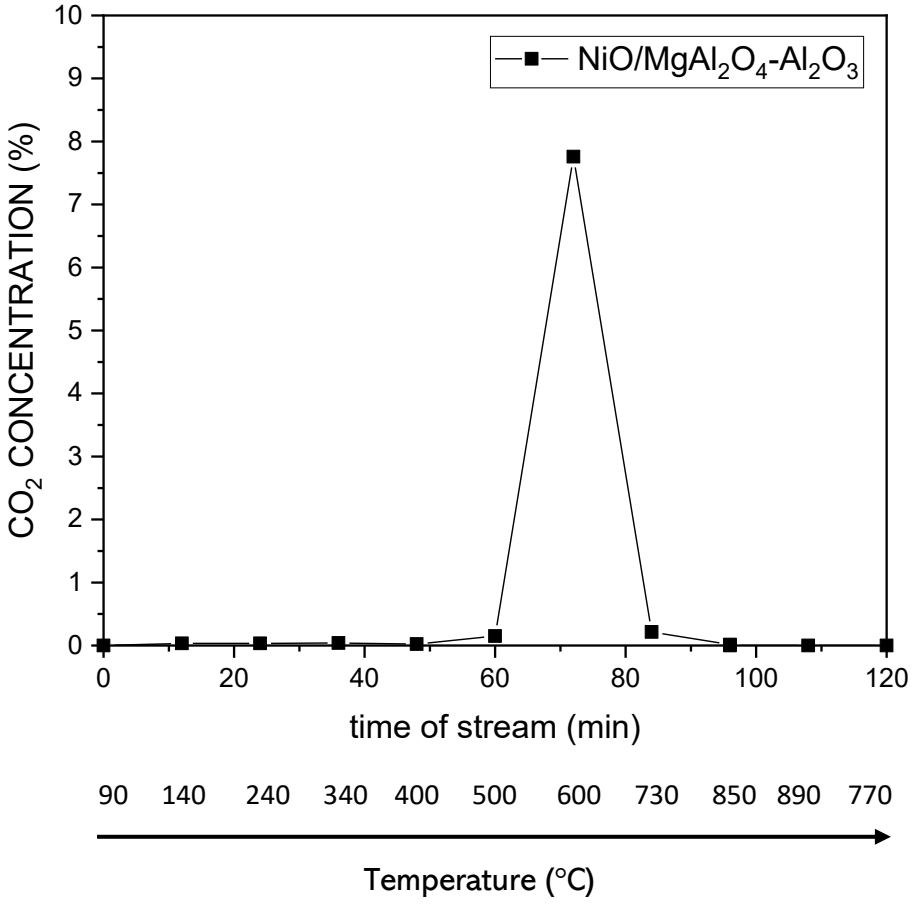

Figure 110- CO_2 concentration vs time measured for post-reaction $NiO/MgAl_2O_4$-Al_2O_3 (25% CH_4, 25% CO_2, 1% NO) obtained by using a 5% O_2 gas flow and a temperature ramp (room temperature-900°C)

$NiO/MgAl_2O_4$-Al_2O_3 showed high CO_2 development around 600°C, therefore suggesting graphitic carbon gasification. [74] High CO_2 levels obtained could be due to the support basicity, that help to attract CO_2 molecules near the sample in order to allow the reaction with the deposited carbon. However, being the ramp temperature quite fast (10°C/min), only a few points have been recorded; so, in order to gain more information about the temperature of gasification of the coke of the samples, it would be interesting to detect the concentration of CO_2 produced in smaller range of temperatures, by performing TPO experiments with milder temperature ramps.

3- $NiO/LaFeO_3$

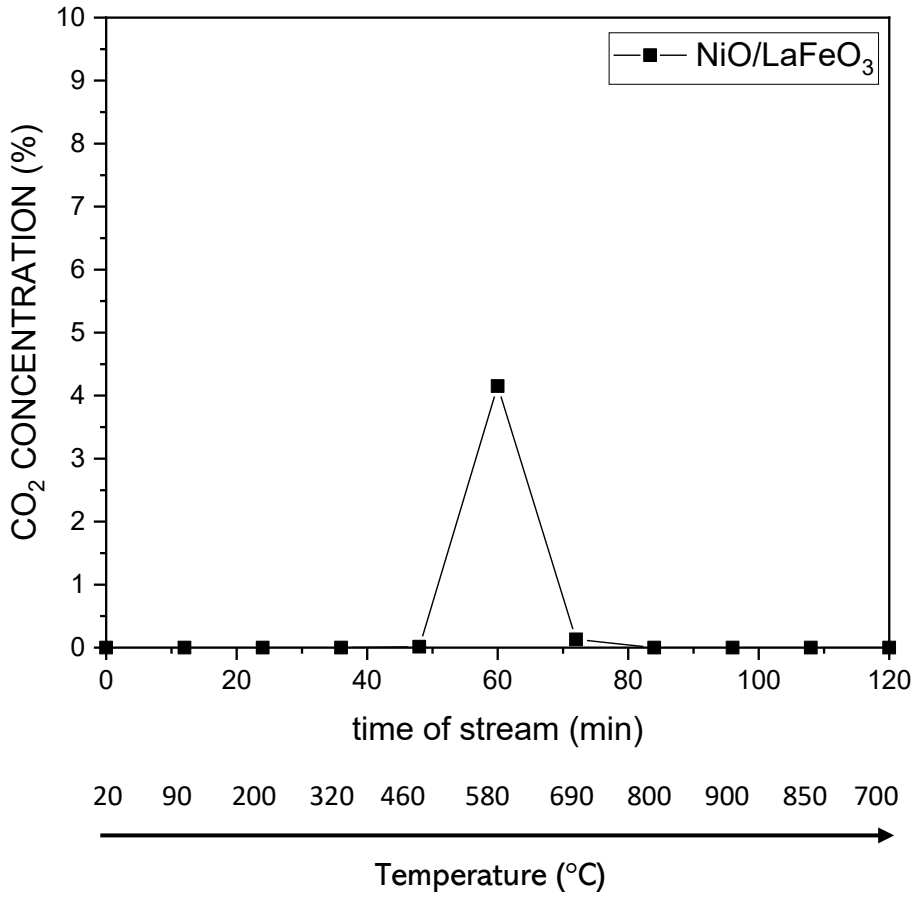

Figure 111- CO_2 concentration vs time measured for post-reaction $NiO/LaFeO_3$ (25% CH_4, 25% CO_2, 1% NO) obtained by using a 5% O_2 gas flow and a temperature ramp (room temperature-900°C)

$NiO/LaFeO_3$ catalyst has also been tested. This catalyst shows a wider range of gasification temperatures than the other catalysts, that centers around 600°C. Both amorphous or graphitic carbon could be reduced in this interval, and other TPO experiments would be interesting to be performed to understand if in this range of temperature different forms of carbon are gasified. As for the previous catalyst, $LaFeO_3$ basic properties help with CO_2 gasification, reaching a CO_2 concentration level of around 5%. This concentration level is less than for the previous catalyst; this could be due to a difference in the ability of gasifying coke, such as different sites for CO_2 chemisorption, or a different type of deposited coke. However, no clear conclusions can be obtained, also considering that only a few points have been taken into account in this graph, and that a more accurate description of CO_2 evolution during temperature increase is needed for a better understanding.

Finally, after testing with O_2-TPO experiments, another oxidizing treatment was conducted: NO-TPO; the results are reported in figure 112. Temperature was increased until reaching the temperature of the catalytic process (750°C), so that NO gasification properties could be verified for the studied process. 5% NO in Ar was chosen as concentration of gas flow, and the obtained graphs is shown below:

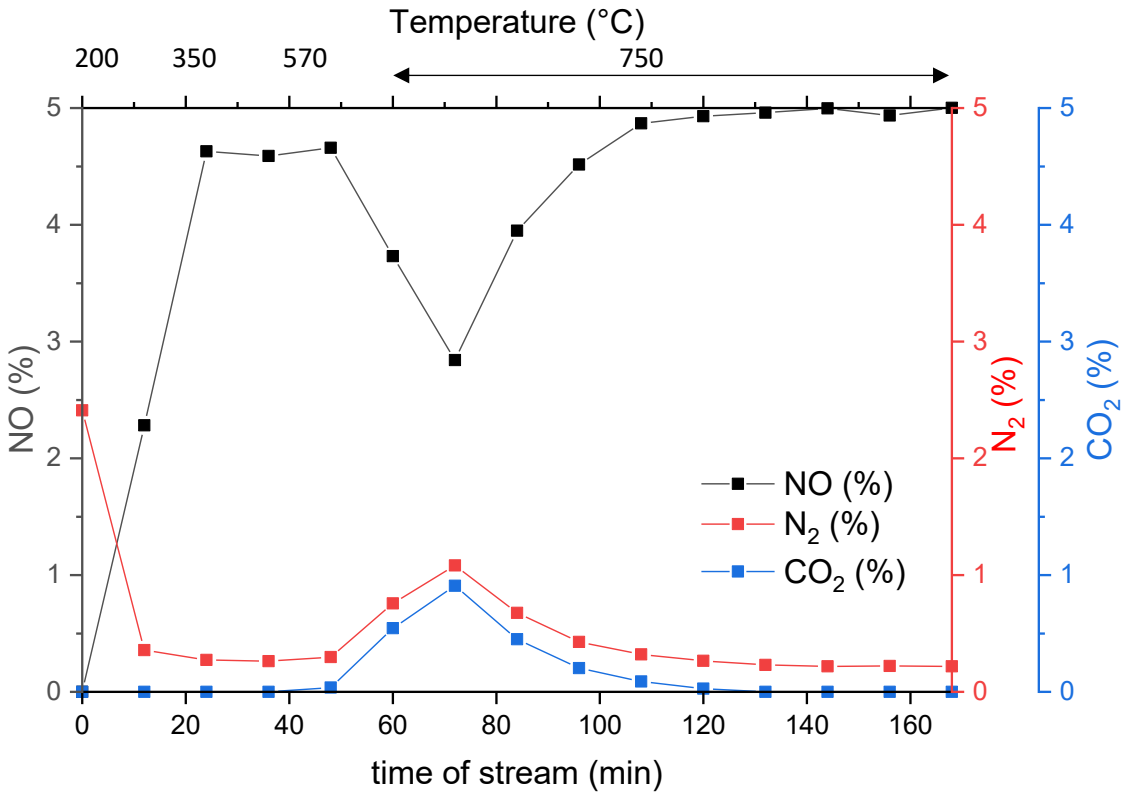

Figure 112- CO_2 concentration vs time measured for post-reaction NiO/Al_2O_3 (5% NO in Ar) obtained by heating the sample from room temperature to 750°C in temperature ramp (10°C/min)

NO, N_2 and CO_2 have been obtained in the process, as expected by the reactions described in chapter 1.2.. No CO was detected during the experiment. NO flow clearly reacts from 200°C, being completely converted in N_2 (2.5%). No CO_2 is produced in this first moment of reaction, indicating that NO must react with something different than coke. In this range of temperature, NO can react with nickel particles, oxidizing them to NiO, as suggested both by prior experiments (see the oxidation of catalysts in the experiments in chapter 1.4.1.) and by literature, as reported in chapter 1.2.. At around 400°C, NO concentration reaches around 5%, therefore the majority of NO doesn't react with the sample. Finally, after 600°C NO is consumed again, with production of N_2 and CO_2 associated to his consumption. This is clearly the temperature in which the carbon deposited onto the catalyst starts to be removed and gasified in form of CO_2. Up to 1% of NO reacts with coke, giving 1% N_2 and 1% CO_2 as suggested by the stoichiometry of the reaction. [18] Carbon

continues to be gasified from 750°C for around 1 hour under gas stream, therefore confirming the validity of this method for coke gasification and NO conversion.

CONCLUSIONS

This project was focused on developing a solution for coking problem that affects commercial nickel-based catalysts for dry reforming of methane. The solution studied was to couple dry reforming of methane with nitric oxide reduction, in order to reduce nitric oxide- one the major pollutants in the atmosphere- with the coke that was deposited onto the catalysts during the process, therefore gasifying it.

Four different catalysts were developed for the process: 4 supports were chosen with different properties, then nickel was impregnated onto the support via a wet-impregnation synthesis, keeping the same conditions for all impregnations. The studied supports were 4 oxides, all synthesizable with simple and economic synthesis in order to be industrially applicable. The main properties taken into consideration for the choice of the supports were high metal-support interaction, which helps to obtain smaller and more stable nickel particles, and the basicity of the support, which helps to coordinate CO_2 acidic molecules to the surface and so to increase its conversion. The supports chosen were γ-Al_2O_3, which is a standard for dry reforming of methane process and has a high metal-support interaction with nickel particles, $MgAl_2O_4$-Al_2O_3, which has not only a high metal support interaction but also a Mg ion with Lewis basicity properties that helps with CO_2 conversion, and two basic perovskite catalysts with properties that can be tuned by the choice of the cations: $CaZrO_3$, which has good thermal stability, and $LaFeO_3$, which is able to convert NO molecules in N_2, therefore participating in nitric oxide reduction reaction.

Commercial γ-Al_2O_3 was employed, while for the $MgAl_2O_4$ spinel coated sample a co-precipitation technique was used, using $Mg(OH)_2$ and γ-Al_2O_3 precursors in stoichiometric amounts. The perovskites supports have been synthetized via a citrate self-combustion route: stoichiometric quantities of precursors of the metal cations were dissolved in water and HNO_3 if needed, then citric acid was dissolved in water and added to the solution of the cations in order to coordinate the cations as a complexing agent. Citric acid was used in stoichiometric amount of 1.1 and 1.9 moles for mole of total cations for respectively $LaFeO_3$ and $CaZrO_3$ perovskite, the amount of citric acid being optimized for the two perovskites. Calcination was then carried out to obtain the supports and, after confirming via XRD analysis the presence of the desired phase, nickel was impregnated on the sample, starting from its nitrate precursor.

Catalysts were studied by means of different techniques to obtain information such as their dispersion (pulsed H_2 chemisorption experiments), surface area and porosity (N_2 physisorption), reducibility (H_2-TPR), composition (XRD, XPS, EDX) and morphology (SEM).

H_2-TPR studies allowed to understand the reducibility of the samples; alumina-based catalysts showed high temperature of reduction, around 700-800°C, which indicate highly interacting nickel particles and, as later

verified by XPS and XRD experiments, the presence of $NiAl_2O_4$ spinel-formed during calcination. The formation of the spinel is due to nickel ions that entered into the alumina structure. Perovskite supports were characterized by low interaction with nickel particles, with reduction temperatures centered around 400-500°C.

Catalysts showed very different values of specific surface area, measured via BET analysis: alumina presented the highest surface area (more than 100 m^2/g), while after spinel coating its surface area was half then before. Perovskites catalysts had instead low surface area under 10 m^2/g, as expected for those supports.

Catalytic activity was then measured for all catalysts. Tests were made of a pre-reductive treatment in 5% H_2, heating the sample until 900°C for alumina-based catalysts or 600°C for perovskite catalysts (as suggested by H_2-TPR experiments), then temperature was decreased until 100-300°C, and the gas consequently changed to the reaction mixture injected in the reactor; catalytic activity was measured keeping the temperature constant at 750°C.

First tests were conducted with a 5% CH_4, 5% CO_2, 1% NO gas mixture. NiO/Al_2O_3 was tested for 6 hours and showed high and sable catalytic activity, but no carbon was formed as shown by XRD pattern of the spent catalyst. In order to understand if the coke was formed and completely removed by NO or if the conditions of the reaction didn't allow carbon deposition, the catalyst was tested for dry reforming of methane reaction for the same amount of time. No coke was detected via XRD analysis. So, the following tests were conducted considering a longer time of reaction of 15 hours. Moreover, NO oxidation properties were investigated by carrying out experiment with different temperatures at which, after the reductive treatment, the reactant gas mixture was injected, as explained later.

Tests were conducted for all catalysts, starting with NiO/Al_2O_3, that showed high initial conversions but was soon deactivated after around 400 minutes of reaction; this fast deactivation, in contrast with the stable catalytic activity obtained for the same catalyst in the same temperature and gas concentration conditions for 360 minutes test (6 h), was ascribed to the different temperature at which NO was injected (in the 6 hours experiment the reactant mixture was injected when the temperature was around 250°C, in the 15 hours the reactor was cooled until 100°C), indicating that NO can react with nickel particles to give N_2 and NiO; it is the conversion of nickel in its non-active oxide form NiO that caused the fast catalyst deactivation. $NiO/MgAl_2O_4$-Al_2O_3 catalyst, studied for the 15 hours process, showed better CO_2 conversions, as expected for its basicity, and a higher stability in catalytic activity, probably due to its higher metal-support interaction- as suggested by H_2-TPR studies. Finally, the perovskite catalysts were tested; while $NiO/CaZrO_3$ had almost no catalytic activity, $NiO/LaFeO_3$ showed the highest and most stable activity, with CO_2 and CH_4 conversions around 90% and CO yield around 80%, with constant values during all the tested reaction time. While $NiO/CaZrO_3$'s poor

interaction with nickel particles determines its fast deactivation due to NO oxidation, $NiO/LaFeO_3$ was able to protect the particles from NO oxidation, being the perovskite able to reduce NO and therefore preserving nickel particles in their metal form.

Spent catalysts showed nickel oxidation to its oxide form, and no carbon was detected on any catalyst. So, reaction conditions were changed again, using a 25% CH_4, 25% CO_2, 1% NO gas mixture. This time, the reaction mixture was injected when the reactor was at 300°C, in order to avoid catalyst deactivation. This experiments finally allowed to obtain high and stable conversions for all catalysts except $NiO/CaZrO_3$, who showed no significant activity. Alumina-based catalysts had the best performance, with NiO/Al_2O_3 conversions around 93%, while $NiO/MgAl_2O_4$-Al_2O_3 had higher CO_2 conversions (97%) but lower CH_4 conversions (88-82%). $NiO/LaFeO_3$ catalysts, on the other hand, had smaller values of conversion than in the 6 hours tests, with CO_2 conversion being around 91-83% and CH_4 conversions around 55-44%. $LaFeO_3$ activity was less stable in the 15 hours process, probably due to its little metal support-interaction that exacerbated the deactivation of the nickel particles, leading to their sintering and oxidation.

All catalyst except for $NiO/CaZrO_3$ - that had basically no catalytic activity - showed the presence of coke in form of graphitic carbon, both at XRD and XPS measurements. Spent catalysts were all characterized by the presence of metallic nickel; nickel oxide was found in NiO/Al_2O_3 and $NiO/LaFeO_3$ post-reaction samples, due to NO oxidation. However, NiO will be most-probably present in $NiO/MgAl_2O_4$-Al_2O_3 catalyst as well, maybe in amorphous form, as this support offers less protection from nickel oxidation than $LaFeO_3$ (as the first catalytic tests had shown), in which nickel oxide was found.

Carbon amount in the spent catalysts was compared via a semi-quantitative XPS elemental quantification, showing higher carbon atomic concentration for Al_2O_3 acidic support, followed by magnesium-aluminum spinel support and finally $LaFeO_3$ perovskite, that was the support that had the best anti-coking properties, both thanks to its basicity and to the possibility of attracting NO towards its surface.

Finally, carbon reactivity was studied via TPO experiments, in order to understand how easily it can be gasified, and to gain information about its morphology. O_2-TPO experiments were conducted in temperature ramp, heating samples until 900°C. All coked catalysts showed gasification abilities, with alumina support being the worst support for carbon gasification (both in quantity of CO_2 produced and in type of carbon gasifiable). While alumina allowed amorphous carbon gasification, other catalysts had CO_2 production at temperatures corresponding to graphitic carbon gasification.
NO-TPO experiment was then conducted to verify NO oxidizing power toward carbon. Post-15 hours of reaction NiO/Al_2O_3 was studied under a 5% NO gas stream, at 750°C. NO allowed to gasify carbon at the temperature of the catalytic processes, giving N_2 and CO_2 as products.

In conclusion, NO reduction can be an interesting reaction to couple with dry reforming of methane in order to reduce coking of the catalysts and to obtain the conversion of three major pollutants/greenhouse gasses that affect our world today: NO, CH_4 and CO_2. Among the tested catalysts, depending on the concentrations of the gas reactants used, $NiO/LaFeO_3$ or NiO/Al_2O_3 were the best catalysts respectively for 5% CH_4, 5% CO_2, 1% NO gas mixture and 25% CH_4, 25% CO_2, 1% NO gas mixture. However, $NiO/MgAl_2O_4$-Al_2O_3 had the best performance in CO_2 conversion, thanks to its basicity. The good catalytic performance of alumina-based catalysts was obtained thanks to the high metal-support interaction and high superficial area. $NiO/LaFeO_3$ gave, instead, high protection against nickel oxidation, thanks to the support's ability to promote NO reduction to N_2. However, its low metal-support interaction and low surface area, typical of perovskites, didn't allow high stable conversions for 25% CH_4, 25% CO_2, 1% NO tests.

Nickel oxidation caused by NO was the main deactivation cause for the catalysts. Therefore, in order to have high and constant conversions, NO concentration in the gas mixture must be well calibrated in order not to have a too oxidative atmosphere. High metal support interaction catalysts and supports with the ability of protecting nickel from oxidation are fundamental to have long catalysts lifetime- that is a necessary condition for the industrial application of the processes. Deeper investigations are therefore necessary to assess the real possibility of employing this process, regarding for example supports and synthesis that allow a better protection from NO oxidation and the choice of the reactant gas concentrations, to allow a better calibration of oxidative and reductive properties of the gas mixture.

REFERENCES

[1] N. Hadian and M. Rezaei, 'Combination of dry reforming and partial oxidation of methane over Ni catalysts supported on nanocrystalline MgAl2O4', *Fuel*, vol. 113, pp. 571–579, Nov. 2013

[2] S. Bhattar, Md. A. Abedin, S. Kanitkar, and J. J. Spivey, 'A review on dry reforming of methane over perovskite derived catalysts', *Catal. Today*, vol. 365, pp. 2–23, Apr. 2021

[3] K. Selvarajah, N. H. H. Phuc, B. Abdullah, F. Alenazey, and D.-V. N. Vo, 'Syngas production from methane dry reforming over Ni/Al2O3 catalyst', *Res. Chem. Intermed.*, vol. 42, no. 1, pp. 269–288, Jan. 2016

[4] J. Deng, B. Yang, Y. Liu, X. Zhang, J. Zheng and D. Zhang, 'Sintering- and coking-resistant nickel catalysts embedded in boron nitride supported nickel aluminate spinels for dry reforming of methane, *Appl. Cat. A: Gen.,* vol. 642, Jul. 2022

[5] M. Tao, X. Meng, Y. Lv, Z. Bian, Z. Xhin,'Effect of impregnation solvent on Ni dispersion and catalytic properties of Ni/SBA-15 for CO methanation reaction', *Fuel*, vol. 165, pp. 289-297, Feb. 2016

[6] T. Juzsakova, N. Al-Jammal, I. Cretescu, V. Sebestyén, C. Le Phuoc, E. Domokos, A. Rédey, and C.D. Stan, 'Case Studies for Clean Technology Development in the Chemical Industry Using Zeolite Based Catalysts', *Minerals*, 2018

[7] US Dep. of Energy, '8.7. Nitrogen Oxides (NOx) Emissions', *netl.doe.gov,* 2014, https://www.netl.doe.gov/research/Coal/energy-systems/gasification/gasifipedia/nitrogen-oxides

[8] C. Wang *et al.*, 'Coking and deactivation of a mesoporous Ni–CaO–ZrO2 catalyst in dry reforming of methane: A study under different feeding compositions', *Fuel*, vol. 143, pp. 527–535, Mar. 2015

[9] E. Ruckenstein and H. Y. Wang, 'Carbon Deposition and Catalytic Deactivation during CO2 Reforming of CH4 over Co/γ-Al2O3 Catalysts', *J. Catal.*, vol. 205, no. 2, pp. 289–293, Jan. 2002

[10] S. Wang, 'A Comprehensive Study on Carbon Dioxide Reforming of Methane over Ni/γ-Al2O3 Catalysts', *Ind. Eng. Chem. Res.*, vol. 38, no. 7, pp. 2615–2625, Jul. 1999

[11] D. Wang, P. Littlewood, T. J. Marks, P. C. Stair, and E. Weitz, 'Coking Can Enhance Product Yields in the Dry Reforming of Methane', *ACS Catal.*, vol. 12, no. 14, pp. 8352–8362, Jul. 2022

[12] C. H. Bartholomew, 'Carbon Deposition in Steam Reforming and Methanation', *Catal. Rev.*, vol. 24, no. 1, pp. 67–112, Jan. 1982

[13] O. Muraza and A. Galadima, 'A review on coke management during dry reforming of methane', *Int. J. Energy Res.*, vol. 39, no. 9, pp. 1196–1216, 2015

[14] L. Baharudin, N. Rahmat, N. H. Othman, N. Shah, and S. S. A. Syed-Hassan, 'Formation, control, and elimination of carbon on Ni-based catalyst during CO2 and CH4 conversion via dry reforming process: A review', *J. CO2 Util.*, vol. 61, p. 102050, Jul. 2022

[15] J. Guo, H. Lou, H. Zhao, D. Chai, and X. Zheng, 'Dry reforming of methane over nickel catalysts supported on magnesium aluminate spinels', *Appl. Catal. Gen.*, vol. 273, no. 1, pp. 75–82, Oct. 2004

[16] Y. Kathiraser, U. Oemar, E. T. Saw, Z. Li, and S. Kawi, 'Kinetic and mechanistic aspects for CO2 reforming of methane over Ni based catalysts', *Chem. Eng. J.*, vol. 278, pp. 62–78, Oct. 2015

[17] K. Wittich, M. Krämer, N. Bottke, and S. A. Schunk, 'Catalytic Dry Reforming of Methane: Insights from Model Systems', *ChemCatChem*, vol. 12, no. 8, pp. 2130–2147, 2020

[18] J. Hu, V. V. Galvita, H. Poelman, Z. Wang, G. B. Marin, and S. Kawi, 'Coupling CO2 utilization and NO reduction in chemical looping manner by surface carbon', *Appl. Catal. B Environ.*, vol. 297, p. 120472, Nov. 2021

[19] J. Song, Z. Wang, X. Cheng, and X. Wang, 'State-of-Art Review of NO Reduction Technologies by CO, CH4 and H2', *Processes*, vol. 9, no. 3, Art. no. 3, Mar. 2021

[20] J. N. Armor, 'Catalytic reduction of nitrogen oxides with methane in the presence of excess oxygen: A review', *Catal. Today*, vol. 26, no. 2, pp. 147–158, Nov. 1995

[21] N. A. K. Aramouni, J. G. Touma, B. A. Tarboush, J. Zeaiter, and M. N. Ahmad, 'Catalyst design for dry reforming of methane: Analysis review', *Renew. Sustain. Energy Rev.*, vol. 82, pp. 2570–2585, Feb. 2018

[22] A. H. K. Owgi *et al.*, 'The preferable Ni quantity to boost the performance of FSA for dry reforming of methane', *Fuel*, vol. 332, p. 126124, Jan. 2023
[23] Z. Alipour, M. Rezaei, and F. Meshkani, 'Effect of Ni loadings on the activity and coke formation of MgO-modified Ni/Al2O3 nanocatalyst in dry reforming of methane', *J. Energy Chem.*, vol. 23, no. 5, pp. 633–638, Sep. 2014
[24] F. Meshkani, M. Rezaei, and M. Andache, 'Investigation of the catalytic performance of Ni/MgO catalysts in partial oxidation, dry reforming and combined reforming of methane', *J. Ind. Eng. Chem.*, vol. 20, no. 4, pp. 1251–1260, Jul. 2014
[25] T. Wei, L. Jia, J.-L. Luo, B. Chi, J. Pu, and J. Li, 'CO2 dry reforming of CH4 with Sr and Ni co-doped LaCrO3 perovskite catalysts', *Appl. Surf. Sci.*, vol. 506, p. 144699, Mar. 2020
[26] A. Abdulrasheed, A. A. Jalil, Y. Gambo, M. Ibrahim, H. U. Hambali, and M. Y. Shahul Hamid, 'A review on catalyst development for dry reforming of methane to syngas: Recent advances', *Renew. Sustain. Energy Rev.*, vol. 108, pp. 175–193, Jul. 2019
[27] M. C. J. Bradford and M. A. Vannice, 'Catalytic reforming of methane with carbon dioxide over nickel catalysts I. Catalyst characterization and activity', *Appl. Catal. Gen.*, vol. 142, no. 1, pp. 73–96, Aug. 1996
[28] Q. Sun, Z. Whang, D. Wang, Z. Hong, M. Zhou and X. Li, 'A review on the catalytic decomposition of NO to N2 and O2: catalysts and processes',*Catal. Sci. Technol.*, vol. 8, pp. 4563-4575, 2018
[29] S. Wang and G. Q. M. Lu, 'CO2 reforming of methane on Ni catalysts: Effects of the support phase and preparation technique', *Appl. Catal. B Environ.*, vol. 16, no. 3, pp. 269–277, May 1998
[30] L. Zhou, L. Li, N. Wei, J. Li, and J.-M. Basset, 'Effect of NiAl2O4 Formation on Ni/Al2O3 Stability during Dry Reforming of Methane', *ChemCatChem*, vol. 7, no. 16, pp. 2508–2516, 2015
[31] P. Chupas, K. Chapman, and G. J. Halder, 'Elucidating the Structure of Surface Acid Sites on γ-Al2O3', *J. Am. Chem. Soc.*, vol. 133, no. 22, pp. 8522–8524, Jun. 2011
[32] Y. Chen, M. Li, Z. Li, F. Liu, G. Song, and S. Kawi, 'Efficient syngas production via CO2 reforming and electroreduction reactions through catalyst design', *Energy Convers. Manag.*, vol. 265, p. 115744, Aug. 2022
[33] M. G. Brik, A. Suchocki, and A. Kamińska, 'Lattice Parameters and Stability of the Spinel Compounds in Relation to the Ionic Radii and Electronegativities of Constituting Chemical Elements', *Inorg. Chem.*, vol. 53, no. 10, pp. 5088–5099, May 2014
[34] M. Abbas, U. Sikander, M. T. Mehran, and S. H. Kim, 'Exceptional stability of hydrotalcite derived spinel Mg(Ni)Al2O4 catalyst for dry reforming of methane', *Catal. Today*, vol. 403, pp. 74–85, Nov. 2022
[35] C. Biagioni and M. Pasero, 'The systematics of the spinel-type minerals: An overview', *Am. Mineral.*, vol. 99, no. 7, pp. 1254–1264, Jul. 2014
[36] M. A. P. and and J. L. G. Fierro, 'Chemical Structures and Performance of Perovskite Oxides', *ACS Publications*, *Chem. Rev.*, vol. 101, no. 7, 1981–2018, May 2001
[37] A. Manikandan, S. Yassine, A. Dinesh, I. Khan, A. Khan, M. M. A. Khan, S. Khan, F. Verpoort, and A. Umar, '8 - Perovskite's potential functionality in a composite structure', *Hybrid Perovskite Composite Materials*, pp. 181–202, 2021
[38] Z. Bian, Z. Wang, B. Jiang, P. Hongmanorom, W. Zhong, and S. Kawi, 'A review on perovskite catalysts for reforming of methane to hydrogen production', *Renew. Sustain. Energy Rev.*, vol. 134, p. 110291, Dec. 2020
[39] A.V. Nikonov, K.A. Kuterbekov, K.Z. Bekmyrza and N.B. Pavzderin, 'A brief review of conductivity and thermal expansion of perovskite-related oxides for SOFC cathode', *Eurasian Journal of Physics and Functional Materials*, vol. 2, no. 3, pp. 274-292, 2018
[40] F. Polo-Garzon and Z. Wu, 'Acid–base catalysis over perovskites: a review', *J. Mater. Chem. A*, vol. 6, no. 7, pp. 2877–2894, 2018
[41] A. Hossain, S. Roy, and K. Sakthipandi, 'The external and internal influences on the tuning of the properties of perovskites: An overview', *Ceram. Int.*, vol. 45, no. 4, pp. 4152–4166, Mar. 2019

[42] K. Lertwittayanon, W. Youravong, and W. J. Lau, 'Enhanced catalytic performance of Ni/α-Al2O3 catalyst modified with CaZrO3 nanoparticles in steam-methane reforming', *Int. J. Hydrog. Energy*, vol. 42, no. 47, pp. 28254–28265, Nov. 2017
[43] H. R. Radfarnia and M. C. Iliuta, 'Hydrogen production by sorption-enhanced steam methane reforming process using CaO-Zr/Ni bifunctional sorbent–catalyst', *Chem. Eng. Process. Process Intensif.*, vol. 86, pp. 96–103, Dec. 2014
[44] J. Chen, M. Shen, X. Wang, J. Wang, Y. Su, and Z. Zhao, 'Catalytic performance of NO oxidation over LaMeO3 (Me=Mn, Fe, Co) perovskite prepared by the sol–gel method', *Catal. Commun.*, vol. 37, pp. 105–108, Jul. 2013
[45] G. E. Andrews, 'Ultra-low nitrogen oxides (NOx) emissions combustion in gas turbine systems', in *Modern Gas Turbine Systems*, 16, pp. 715–790, 2013
[46] Siemens Energy, 'Gas turbines or gas engines?', www.siemens-energy.com, 2021
[47] A. Bedon, M. M. Natile, and A. Glisenti, 'On the synthesis and stability of La0.6Sr0.4Ga0.3Fe0.7O3', *J. Eur. Ceram. Soc.*, vol. 37, no. 3, pp. 1049–1058, Mar. 2017
[48] P. Stoch, J. Szczerba, J. Lis, D. Madej, and Z. Pędzich, 'Crystal structure and ab initio calculations of CaZrO3', *J. Eur. Ceram. Soc.*, vol. 32, no. 3, pp. 665–670, Mar. 2012
[49] C. A.L. Dixon, C. M. Kavanagh, K. S. Knight, W. Kockelmann, F. D. Morrison and P. Lightfoot, 'Thermal evolution of the crystal structure of the orthorhombic perovskite LaFeO3', *J. Solid State Chem.*, vol. 230, pp. 337–342, Oct. 2015
[50] M. Thommes, K. Kaneko, A. V. Neimark, J. P. Olivier, F. Rodriguez-Reinoso, J. Rouquerol and K. S. W. Sing,' Physisorption of gases, with special reference to the evaluation of surface area and pore size distribution (IUPAC Technical Report), *Pure Appl. Chem*., vol. 87, no.9-10, pp. 1051–1069, 2015
[51] S. Storck, H. Bretinger, and W. F. Maier, 'Characterization of micro- and mesoporous solids by physisorption methods and pore-size analysis', *Appl. Catal. Gen.*, vol. 174, no. 1, pp. 137–146, Nov. 1998
[52] E. P. Barrett, L. G. Joyner, and P. P. Halenda, 'The Determination of Pore Volume and Area Distributions in Porous Substances. I. Computations from Nitrogen Isotherms', *J. Am. Chem. Soc.*, vol. 73, no. 1, pp. 373–380, Jan. 1951
[53] A. M. Holban, A. M. Grumezescu, and E. Andronescu, 'Inorganic nanoarchitectonics designed for drug delivery and anti-infective surfaces', *Surf. Chem. of Nanobiomaterials*, 10, pp. 301–327, 2016
[54] M. Tavanarad, F. Meshkani, and M. Rezaei, 'Production of syngas via glycerol dry reforming on Ni catalysts supported on mesoporous nanocrystalline Al2O3', *J. CO2 Util.*, vol. 24, pp. 298–305, Mar. 2018
[55] G. Li, L. Hu, and J. M. Hill, 'Comparison of reducibility and stability of alumina-supported Ni catalysts prepared by impregnation and co-precipitation', *Appl. Catal. Gen.*, vol. 301, no. 1, pp. 16–24, Feb. 2006
[56] G. Wang *et al.*, 'Effect of Ni Content of Ni/γ-Al2O3 Catalysts Prepared by the Atomic Layer Deposition Method on CO2 Reforming of Methane', *Energy Technol.*, vol. 7, no. 5, p. 1800359, 2019
[57] C. Zhao, Z. Zhou, Z. Cheng, and X. Fang, 'Sol-gel-derived, CaZrO3-stabilized Ni/CaO-CaZrO3 bifunctional catalyst for sorption-enhanced steam methane reforming', *Appl. Catal. B Environ.*, vol. 196, pp. 16–26, Nov. 2016
[58] M. Mokhtar, A. Medkhali, K. Narasimharao, and S. Basahel, 'Divalent Transition Metals Substituted LaFeO3 Perovskite Catalyst for Nitrous Oxide Decomposition', *J. Membr. Sep. Technol.*, vol. 3, no. 4, pp. 206–212, Dec. 2014
[59] X. Li *et al.*, 'In Situ Hydrogen Temperature-Programmed Reduction Technology Based on the Integrated Microcantilever for Metal Oxide Catalyst Analysis', *Anal. Chem.*, vol. 94, no. 47, pp. 16502–16509, Nov. 2022
[60] A. Schön, C. Dujardin, J.-P. Dacquin, and P. Granger, 'Enhancing catalytic activity of perovskite-based catalysts in three-way catalysis by surface composition optimisation', *Catal. Today*, vol. 258, pp. 543–548, Dec. 2015

[61] I. Sebai, A. Boulahaouache, M. Trari, and N. Salhi, ‘Preparation and characterization of 5%Ni/γ-Al2o3 catalysts by complexation with NH3 derivatives active in methane steam reforming’, *Int. J. Hydrog. Energy*, vol. 44, no. 20, pp. 9949–9958, Apr. 2019
[62] H. M. AbdelDayem, M. Faiz, H. S. Abdel-Samad, and S. A. Hassan, ‘Rare earth oxides doped NiO/γ-Al2O3 catalyst for oxidative dehydrogenation of cyclohexane’, *J. Rare Earths*, vol. 33, no. 6, pp. 611–618, Jun. 2015
[63] M. I. Haider, A. Fakharuddin, S. Ahmed, M. Sultan, and L. Schmidt-Mende, ‘Modulating defect density of NiO hole transport layer via tuning interfacial oxygen stoichiometry in perovskite solar cells’, *Sol. Energy*, vol. 233, pp. 326–336, Feb. 2022
[64] G. Bergeret and P. Gallezot, ‘Particle Size and Dispersion Measurements’, *Handbook of Heterogeneous Catalysis*, vol. 2, pp. 738-765, 2008
[65] C.H. Bartholomew, R.B. Pannell, 'The stoichiometry of hydrogen and carbon monoxide chemisorption on alumina- and silica-supported nickel’, *J. Catal.*, vol. 65, no. 2, pp. 390–401, Oct. 1980
[66] J. K. Kesavan *et al.*, ‘Nickel supported on YSZ: The effect of Ni particle size on the catalytic activity for CO2 methanation’, *J. CO2 Util.*, vol. 23, pp. 200–211, Jan. 2018
[67] A. P. Grosvenor, M. C. Biesinger, R. St. C. Smart, and N. S. McIntyre, ‘New interpretations of XPS spectra of nickel metal and oxides’, *Surf. Sci.*, vol. 600, no. 9, pp. 1771–1779, May 2006
[68] X. Zou, Z. Rui, S. Song, and H. Ji, ‘Enhanced methane combustion performance over NiAl2O4-interface-promoted Pd/γ-Al2O3’, *J. Catal.*, vol. 338, pp. 192–201, Jun. 2016
[69] M. Han *et al.*, ‘Physical properties of MgAl2O4, CoAl2O4, NiAl2O4, CuAl2O4, and ZnAl2O4 spinels synthesized by a solution combustion method’, *Mater. Chem. Phys.*, vol. 215, pp. 251–258, Aug. 2018
[70] N. Habibi, Y. Wang, H. Arandiyan, and M. Rezaei, ‘Biogas Reforming for Hydrogen Production: A New Path to High-Performance Nickel Catalysts Supported on Magnesium Aluminate Spinel’, *ChemCatChem*, vol. 8, no. 23, pp. 3600–3610, 2016
[71] A. A. Ansari *et al.*, ‘Optimization of Redox and Catalytic Performance of LaFeO3 Perovskites: Synthesis and Physicochemical Properties’, *J. Electron. Mater.*, vol. 48, no. 7, pp. 4351–4361, Jul. 2019
[72] S. Lamouri *et al.*, ‘Control of the γ-alumina to α-alumina phase transformation for an optimized alumina densification’, *Bol. Soc. Esp. Cerámica Vidr.*, vol. 56, no. 2, pp. 47–54, Mar. 2017
[73] L. Azancot, L. F. Bobadilla, M. A. Centeno, and J. A. Odriozola, ‘Effect of potassium loading on basic properties of Ni/MgAl2O4 catalyst for CO2 reforming of methane’, *J. CO2 Util.*, vol. 52, p. 101681, Oct. 2021
[74] B. Jin, S. Li, and X. Liang, ‘Enhanced activity and stability of MgO-promoted Ni/Al2O3 catalyst for dry reforming of methane: Role of MgO’, *Fuel*, vol. 284, p. 119082, Jan. 2021

6. APPENDIX

3.1.3. SEM

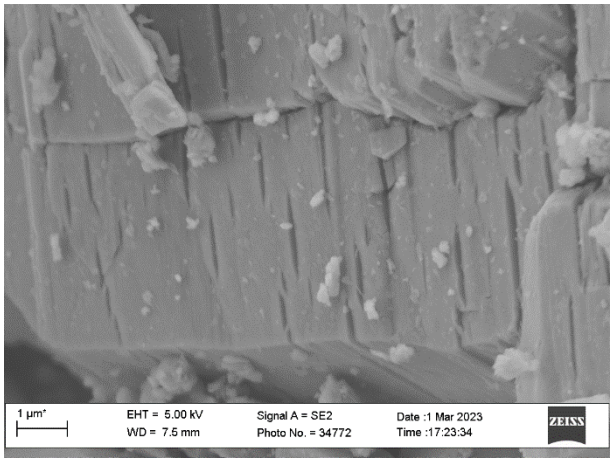

Figure 113- SEM image of Al_2O_3 at 25000x magnification

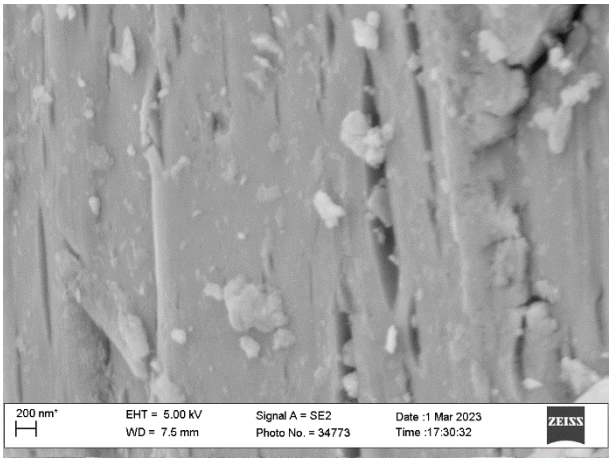

Figure 114- SEM image of Al_2O_3 at 50000x magnification

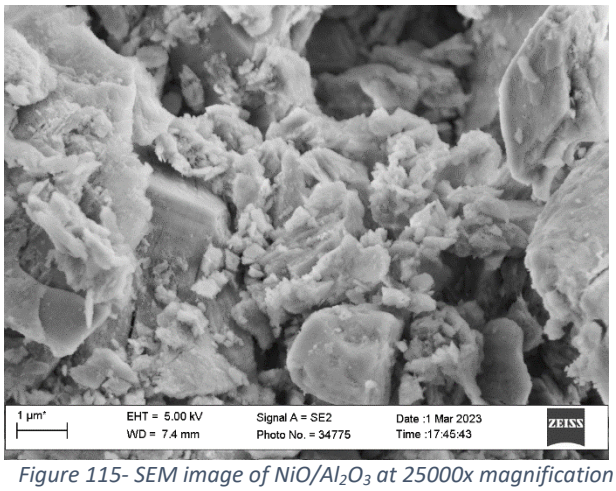

Figure 115- SEM image of NiO/Al_2O_3 at 25000x magnification

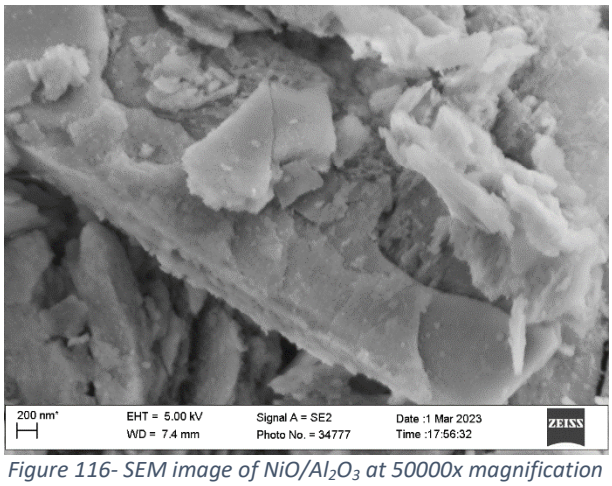

Figure 116- SEM image of NiO/Al_2O_3 at 50000x magnification

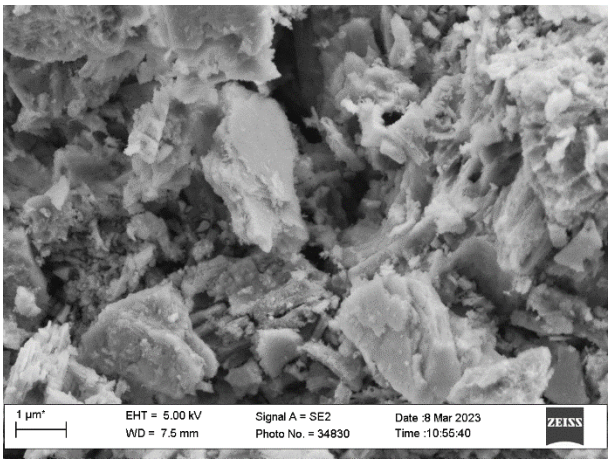

Figure 117- SEM image of $MgAl_2O_4$-Al_2O_3 at 25000x magnification

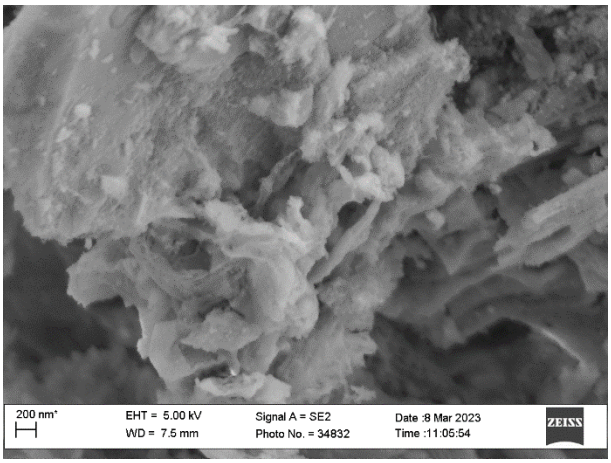

Figure 118- SEM image of $MgAl_2O_4$-Al_2O_3 at 50000x magnification

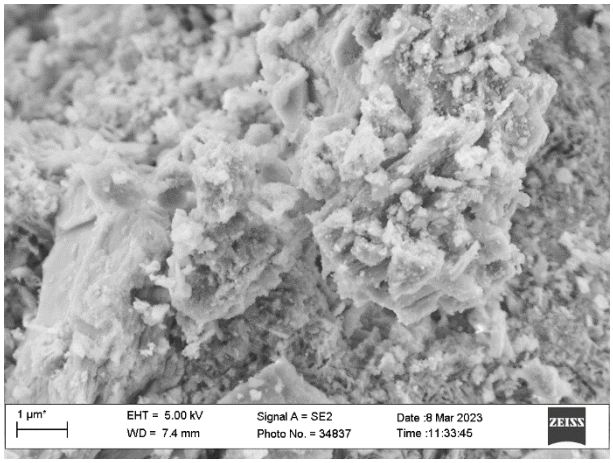

Figure 119- SEM image of NiO/$MgAl_2O_4$-Al_2O_3 at 5000x magnification

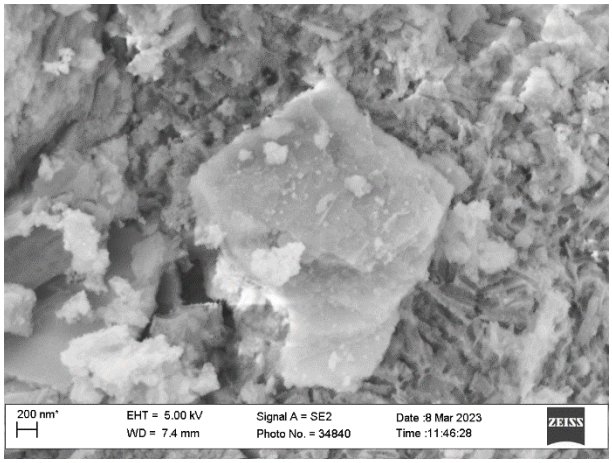

Figure 120- SEM image of NiO/$MgAl_2O_4$-Al_2O_3 at 25000x magnification

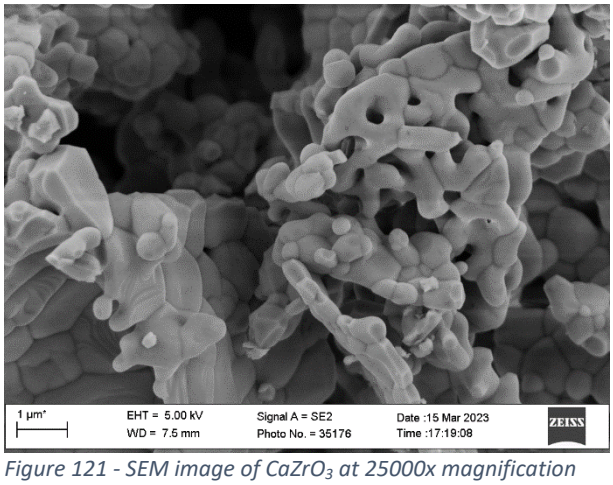

Figure 121 - SEM image of $CaZrO_3$ at 25000x magnification

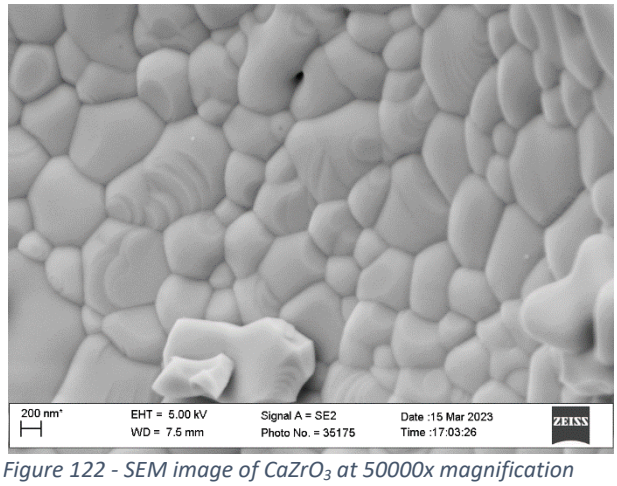

Figure 122 - SEM image of $CaZrO_3$ at 50000x magnification

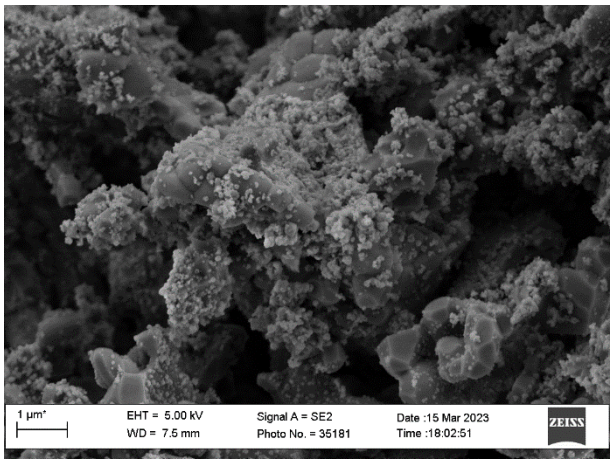

Figure 123 - SEM image of $NiO/CaZrO_3$ at 25000x magnification

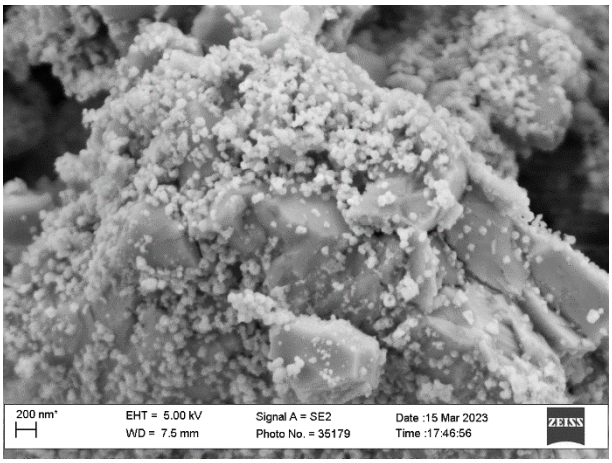

Figure 124 - SEM image of $NiO/CaZrO_3$ at 25000x magnification

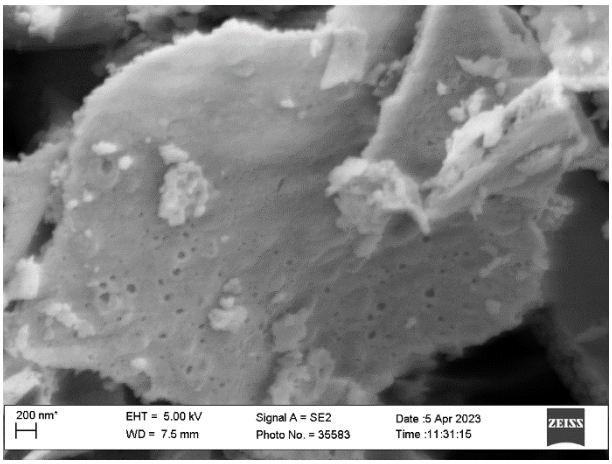

Figure 125 - SEM image of $LaFeO_3$ at 25000x magnification

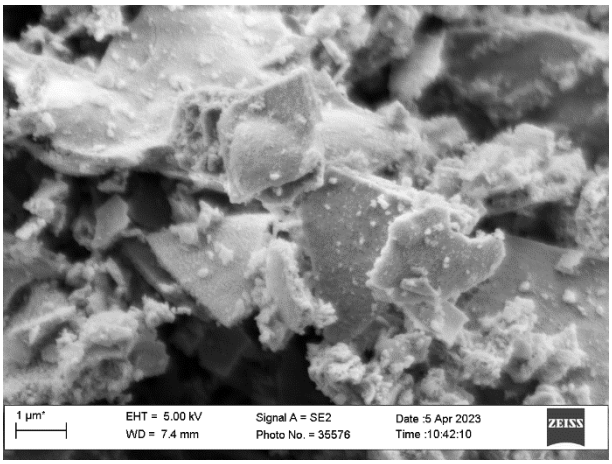

Figure 126 - SEM image of $NiO/LaFeO_3$ at 25000x magnification

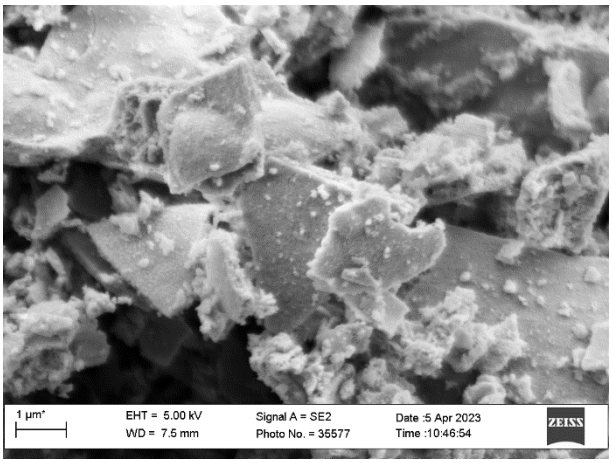

Figure 127 - SEM image of $NiO/LaFeO_3$ at 5000x magnification

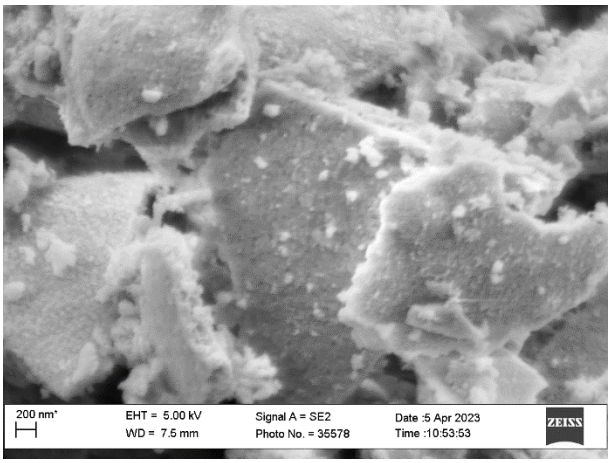

Figure 128 - SEM image of $NiO/LaFeO_3$ at 5000x magnification

6.1. XRD of $NiO/CaZrO_3$

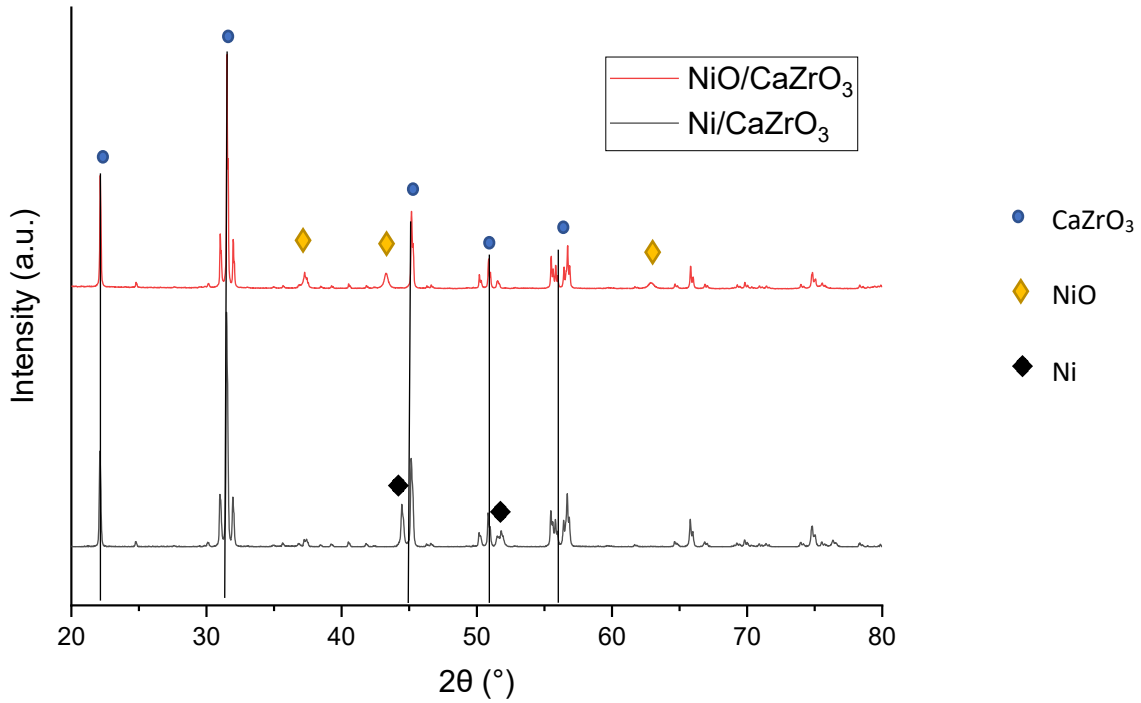

Figure 129 - XRD pattern of NiO/ $CaZrO_3$ catalyst post-calcination and post-reduction treatment (until 600°C)

ACKNOWLEDGMENTS

At first, I would like to express my sincere gratitude to my supervisor, prof. Antonella Glisenti, for her kind guidance and continuous support during my research project; her knowledge, availability and friendliness have been fundamental in my thesis development. Another great thanks is for all the Master students, PhD students and researchers members of Impact Group, for their invaluable help in preparing this thesis and for the constant support in this journey. I feel really lucky to have worked with you. I try to mention you all: Andrea, Giacomo, Simone T., Simone C., Chiara, Ambra, Gabriel, Jonathan, Lorenzo, Pietro, Matteo, Mattia, Davide and Michele. Finally, I would like to thank very much my family, my friends and my partner, who have supported and encouraged me throughout this thesis. This journey wouldn't have been the same without you.